TUNING METAL-ORGANIC FRAMEWORKS FOR FLUE GAS DESULFURIZATION

A Dissertation
Presented to
The Academic Faculty

by

Chengzhai Wang

In Partial Fulfillment
of the Requirements for the Degree
Doctor of Philosophy in the
School of Chemical and Biomolecular Engineering

Georgia Institute of Technology
August 2023

TUNING METAL-ORGANIC FRAMEWORKS FOR FLUE GAS DESULFURIZATION

Approved by:

Dr. Krista S. Walton, Advisor
School of Chemical and Biomolecular Engineering
Georgia Institute of Technology

Dr. Christopher W. Jones
School of Chemical and Biomolecular Engineering
Georgia Institute of Technology

Dr. David S. Sholl
School of Chemical and Biomolecular Engineering
Georgia Institute of Technology

Dr. Joseph P. Sadighi
School of Chemistry and Biochemistry
Georgia Institute of Technology

Dr. Ryan P. Lively
School of Chemical and Biomolecular Engineering
Georgia Institute of Technology

Date Approved: July 20th, 2023

To The People That Supported Me

ACKNOWLEDGEMENTS

I would like to begin by expressing my heartfelt gratitude to my advisor, Dr. Krista S. Walton, whose guidance, support, and expertise have been indispensable throughout the course of my research. Professor Walton's unwavering commitment to excellence and tireless dedication has inspired me to push myself beyond my limits and to produce work that I am truly proud of. I am deeply grateful for your mentorship, guidance, and friendship.

I would also like to extend my sincere thanks to my dissertation committee members, Dr. Christopher W. Jones, Dr. David S. Sholl, Dr. Joseph P. Sadighi, and Dr. Ryan P. Lively, whose thoughtful feedback and insights helped to shape my research in ways that I could not have foreseen. Your critical analyses, incisive comments, and constructive suggestions challenged me to think more deeply about my research questions and to refine my arguments in ways that I believe have strengthened the overall quality of this work.

I am also indebted to Walton group members, Dr. Ian Walton, Dr. Pasquale Fernando Fulvio, Dr. Yutao Gong, Dr. Carmen Chen, Dr. Danny Shade, Dr. Eli Carter, Lukas Willi Bingel, Jamie L Salinger, Mengjiao Wu, Brandon W Bout, Tania G Evans, Ojuolape O Oghenetega, whose kindness, friendship, support, and encouragement have been instrumental in my success. I am particularly grateful to Dr. Ian Walton, Dr. Yutao Gong, Dr. Carmen Chen, Lukas Willi Bingel, and Dr. Kai Cui, who provided invaluable assistance in locating and obtaining the many primary sources that I needed for my projects. Your tireless efforts, attention to detail, and deep knowledge of the collections were absolutely essential to the completion of this dissertation.

In addition, I would like to thank my friends, Qiang Fu, Zhenzi Yu, Xuqing Cai, Yuhan Yang, Chunyi Li, Yue Ji, and Yuge Hu for your unwavering support and encouragement throughout this journey. I am grateful to many individuals at Georgia Tech, including the faculty, staff, building manager, and librarians. Your help sustained me through the long hours of research, writing, and revision, and gave me the strength and courage to persevere even in the face of daunting obstacles. I am also grateful to the Center for Understanding and Control of Acid Gas-Induced Evolution of Materials for Energy (UNCAGE-ME), an Energy Frontier Research Center funded by the U.S. Department of Energy, which allowed me to conduct extensive archival research both domestically and abroad. Without your support, this project would not have been possible.

In closing, I would like to express my deepest gratitude to my father, Xingmiao Wang, my mother, Junzhi Wang, and my wife, Ting Wang for your love, support, encouragement, and trust over the years. I love you all!

TABLE OF CONTENTS

ACKNOWLEDGEMENTS **iv**

LIST OF TABLES **x**

LIST OF FIGURES **xi**

LIST OF SYMBOLS AND ABBREVIATIONS **xv**

SUMMARY **xix**

CHAPTER 1. Introduction **1**

1.1 Flue gas desulfurization **1**

1.1.1 Sulfur dioxide (SO_2) 1

1.1.2 Flue gas 2

1.1.3 Flue gas desulfurization 5

1.2 Adsorption **7**

1.2.1 Adsorption for flue gas desulfurization 7

1.3 Metal-organic frameworks **12**

1.3.1 MOFs for gas adsorption 14

1.3.2 MOFs for flue gas desulfurization and challenges 17

1.4 Dissertation overview **19**

1.5 References **22**

CHAPTER 2. Experimental Materials and Methods **30**

2.1 Materials **30**

2.1.1 Material sources 30

2.1.2 MOFs 30

2.2 Experimental methods **35**

2.2.1 Powder X-ray diffraction (PXRD) 35

2.2.2 N_2 adsorption measurement 36

2.2.3 Thermogravimetric analysis (TGA) 37

2.2.4 Volumetric adsorption system 38

2.2.5 Breakthrough system 39
2.2.6 Infrared spectroscopy (IR) 40
2.3 References 41

CHAPTER 3. Influence of Trivalent Open Metal Sites on SO_2 Adsorption in MOFs 43
3.1 Introduction 43
3.2 Experimental section 45
3.2.1 Materials 45
3.2.2 Characterization and measurements 48
3.3 Results and discussion 49
3.3.1 Crystallinity and porosity of materials 49
3.3.2 SO_2 adsorption of MIL-100-M and IAST selectivity 50
3.3.3 SO_2 stability (Dry and humid) 53
3.3.4 Post trivalent metal insertion for UiO-66-2COOM 56
3.3.5 Humid SO_2 stability 57
3.3.6 SO_2 adsorption of UiO-66-2COOM 59
3.4 Conclusions 62
3.5 References 63

CHAPTER 4. Enhancing SO_2 Capture: Unveiling the Potential of DETA-based ILs for MIL-101 Functionalization 66
4.1 Introduction 66
4.2 Experimental section 69
4.2.1 Materials 69
4.2.2 Characterization and measurements 70
4.3 Results and discussion 71
4.3.1 Crystallinity and porosity of materials 71
4.3.2 DETA and DETA-based ILs in MIL-101 72
4.3.3 SO_2 adsorption and IAST selectivity 76
4.3.4 DRIFTS experiments 82
4.3.5 Stability testing 83

4.4 Conclusions 85
4.5 References 86

CHAPTER 5. Nitrogen-Modified UiO-66 MOFs for Enhanced SO_2 Adsorption: Experimental and Computational Investigations 89
5.1 Introduction 89
5.2 Experimental section 91
5.2.1 Materials 91
5.2.2 Characterization and measurements 93
5.3 Results and discussion 96
5.3.1 Crystallinity and porosity of materials 96
5.3.2 SO_2 Breakthrough Performance 97
5.3.3 Stability toward SO_2 99
5.3.4 SO_2 adsorption and IAST selectivity 101
5.3.5 ATR-IR spectroscopic characterization 104
5.3.6 Pyridine-N vs. pyrazine-N 108
5.4 Conclusions 111
5.5 References 112

CHAPTER 6. Conclusions and Recommendations 116
6.1 Conclusions 116
6.1.1 Chapter 3 conclusions 117
6.1.2 Chapter 4 conclusions 118
6.1.3 Chapter 5 conclusions 119
6.2 Recommendations 120
6.3 References 123

Appendix A. Chpater 3 Supporting Information 125
A.1 Preliminary results of DFT simulations for MIL-101-M (Dr. Thyagarajan Raghuram) 126
A.2 References 132

Appendix B. Chpater 4 Supporting Information 133

B.1 MIL-101-TETA-ILs 138

Appendix C. Chpater 5 Supporting Information 141

C.1 Geometry of the ML3 cluster model 144

C.2 Extension 148

C.3 References 149

LIST OF TABLES

Table 1-1: A typical flue gas compositions 4
Table 1-2: List of MOFs for specific gas adsorption/separation 16
Table 3-1: IAST Selectivity of SO_2/CO_2 for MIL-100-M MOFs. 53
Table 3-2: Summary of BET surface areas of MIL-100-M with different treatments. 56
Table 3-3: BET surface areas of UiO-66-2COOM before and after humid SO_2 exposure 59
Table 4-1: Weight percentage of DETA or DETA-based ILs in MIL-101 composites. 74
Table 4-2: Atomic concentrations (at. %) of elements for the samples. 76
Table 4-3: The summarized calculated IAST selectivity. 81
Table 4-4: BET surface areas of samples after different treatments. 85
Table 5-1: Surface areas of UiO-66 MOFs under SO_2 exposure. 100
Table 5-2: Calculated IAST selectivity. 103
Table 5-3: Calculated adsorption free energy $\Delta G_{ad}^{\ominus}$ (in kcal/mol) via Langmuir model at PBE-D3 level for the parent and N-modified UiO-66 MOFs. 107
Table 5-4: Binding energies (in eV) of SO_2 on the N sites in UiO-66-2,5-PDC and UiO-66-2,5-PziDC recalculated using periodic and cluster models. Numbers in parentheses are calculated using the same setup but exclude the D3 dispersion correction. 109
Table 5-5: Stabilization energies $E^{(2)}$ between the lone pair electrons of the N atom (LP-N) in the linker to three Rydberg orbitals of the S (RY*-S) atom in the SO_2.. 110
Table A-1: Binding energies E (kJ/mol^{-1}) for three adsorbate molecules CO_2, SO_2, and H_2O with MIL-100 trimetallic cluster models with Al, Sc, V, Fe and In metal ions..... 128
Table B-1: Materials information..... 133
Table C-1: Calculated adsorption free energy $\Delta G_{ad}^{\ominus}$ (in kcal/mol) via Langmuir model at LMP2/PBE-D3 level for the parent and N-modified UiO-66 MOFs. 147

LIST OF FIGURES

Figure 1-1: Global contributions of major industry sectors and natural sources (volcanoes) to total SO_2 emissions in 2019. Image reproduced from Dahiya[6]..... 3

Figure 1-2: Schematic diagram of wet scrubbing process for FGD. Image reproduced from Duan and Anthony[16] 6

Figure 1-3: Schematic of different carbon-based adsorbents: a) activated carbon, b) graphene oxide, GO; c) carbon nano-horns, d) carbon nanotubes. Image reproduced from Babu and Schneider[24] 9

Figure 1-4: Structure diagram of zeolites. Image reproduced from Derbe and Bitew[37] 11

Figure 1-5: (a) Schematic of the metal-organic frameworks (MOFs) structure. (b) Structures of common MOFs. Image reproduced from Kampouraki and Deliyanni[48] 13

Figure 1-6: Number of publications of MOFs for gas adsorption (Data from Web of Science, until May 2022). 15

Figure 2-1: Structure of MIL-100. (a) The trimer of metal octahedra and the trimesic acid. (b) One unit cell of MIL-100. (c) The free apertures of the two types of cages. (d) Pentagonal and hexagonal windows of the mesoporous cages. Image reproduced from Zhong and Zhang[2] 31

Figure 2-2: Structure of MIL-101. (a) The small cage. (b) The large cage. (c) Pentagonal and hexagonal windows of the mesoporous cages. Image reproduced from Trung and Ferey[8] 33

Figure 2-3: Structural details of UiO-66. Image reproduced from Rui and Feng[15-16] 34

Figure 2-4: Illustration of the home-built volumetric adsorption system. 39

Figure 2-5: Illustration of the home-built breakthrough system..... 40

Figure 3-1: Schematic structure of UiO-66-2COOM. 45

Figure 3-2: (a), PXRD of MIL-100-M; (b), N_2 adsorption isotherms of MIL-100-M. 50

Figure 3-3: (a), SO_2 isotherms of MIL-100-M; (b), SO_2 isotherms of MIL-100-M at low partial pressures. 51
Figure 3-4: (a), CO_2 isotherms of MIL-100-M; (b), a comparison of SO_2 and CO_2 isotherms for MIL-100-Sc. 53
Figure 3-5: PXRD patterns of Sc-MIL-100 and In-MIL-100 with different treatments. 54
Figure 3-6: (a), PXRD of UiO-66-2COOM; (b), N_2 adsorption isotherms of UiO-66-2COOM. 57
Figure 3-7: PXRD patterns of UiO-66-2COOM before and after humid SO_2 exposure. 58
Figure 3-8: (a) SO_2 isotherms of UiO-66-2COOM, (b) Sc XPS spectra of MIL-100-Sc and UiO-66-2COOSc, and (c) In XPS spectra of MIL-100-In and UiO-66-2COOIn. 61
Figure 4-1: (a) Schematic structures of ILs, (b) DETA coordinated metal cluster of MIL-101. 68
Figure 4-2: (a) PXRD patterns and (b) BET surface areas for MIL-101 and MIL-101 composites. 72
Figure 4-3: TGA curves of (a) MIL-101 and MIL-101-DETA-Lac and (b) MIL-101 and MIL-101 composites. 73
Figure 4-4: (a) XPS survey spectra (b) Cr XPS spectra of MIL-101 and MIL-101 composites. 75
Figure 4-5: (a) SO_2 and (b) CO_2 isotherms for MIL-101 and MIL-101 composites. 77
Figure 4-6: Dual-site Langmuir fitting of the SO_2 and CO_2 isotherms of MIL-101 and MIL-101-DETA-Lac. 80
Figure 4-7: (a) Proposed interaction structure of MIL-101-DETA-Lac with CO_2 and SO_2, (b) Proposed interaction structure of MIL-101-TETA-Lac with CO_2, (c) CO_2 isotherms for MIL-101, MIL-101-DETA-Lac, and MIL-101-TETA-Lac, and (d) SO_2 isotherms for MIL-101, MIL-101-DETA-Lac, and MIL-101-TETA-Lac. 81
Figure 4-8: In-situ DRIFTS spectra for (a), (b) pristine MIL-101 and MIL-101 composites, (c) MIL-101 before, during SO_2 sorption, and after reactivation and (d) MIL-101-DETA-Lac before, during SO_2 sorption, and after reactivation. 83

Figure 4-9: PXRD patterns of all samples (a) after SO_2 isotherm experiments, and (b) after H_2O isotherm experiments. 84
Figure 5-1: (a) Metal cluster and ligand of UiO-66, (b) Selected Ligands used in UiO-66 synthesis. 91
Figure 5-2: (a) PXRD patterns and (b) BET surface areas for UiO-66 type MOFs. 97
Figure 5-3: (a) SO_2 breakthrough curves and (b) Comparison of breakthrough capacity with BET surface areas for UiO-66 type MOFs. 98
Figure 5-4: PXRD patterns of UiO-66 MOFs before and after SO_2 exposure. 100
Figure 5-5: SO_2 isotherms for four "SO_2 stable" samples..... 102
Figure 5-6: SO_2 and CO_2 isotherms for four "SO_2 stable" samples. 103
Figure 5-7: ATR-IR spectra of SO_2 adsorption into four "SO_2 stable" samples. ... 105
Figure 5-8: (a) Four possible binding sites: μ_3-OH site, μ_3-O site, benzene and N sites. Colors: oxygen (red), carbon (brown), nitrogen (grey), sulfur (yellow), zirconium (green), and hydrogen (light pink). (b) Binding energy of SO_2 on the four binding sites on the parent and N-modified UiO-66 MOFs. 106
Figure 5-9: Illustration of the NBOs in in 2,5-PDC-SO_2 complex. (a) the lone pair orbital of N atom (LP-N) and (b) one of the unoccupied Rydberg orbitals of S atom (RY*-S), which corresponds to the first column in Table 5-5..... 110
Figure A-1: Diagram of humid SO_2 exposure device. 125
Figure A-2: Comparisons of SO_2 and CO_2 isotherms for MIL-100-M MOFs. 126
Figure A-3: PXRD of MIL-100-M after different treatments: (a), post dry SO_2, (b), post H_2O, and (c), post humid SO_2. 129
Figure A-4: N_2 adsorption isotherms of MIL-100-M after different treatments: (a), post dry SO_2, (b), post H_2O, and (c), post humid SO_2. 131
Figure A-5: Water vapor isotherms: (a), MIL-100-M; (b), UiO-66-2COOM. 131
Figure A-6: CH_4 isotherms: (a), MIL-100-M; (b), UiO-66-2COOM. 132
Figure B-1: CO_2 isotherms for MIL-101 and MIL-101 composites. 134
Figure B-2: In-situ DRIFTS spectra for (a) MIL-101-DETA, (b) MIL-101-DETA-Cl, and (c) MIL-101-DETA-Ace. 135
Figure B-3: BET surface areas for all samples (a) after SO_2 isotherm experiments and (b) after H_2O isotherm experiments. 136

Figure B-4: N1s XPS spectra of MIL-101 and MIL-101 composites. 138
Figure B-5: (a) PXRD patterns and (b) BET surface areas of MIL-101-TETA-ILs. 139
Figure B-6: CO_2 isotherms of MIL-101-TETA-ILs. 139
Figure B-7: Cr2p XPS spectra of MIL-101-TETA-ILs. 140
Figure C-1: PXRD patterns of (a) UiO-66-NH_2 and (b) UiO-66-2,5-PziDC MOFs before and after SO_2 exposure 141
Figure C-2: BET surface areas of N-modified UiO-66 MOFs. 141
Figure C-3: Water vapor isotherms of N-modified UiO-66 MOFs. 142
Figure C-4: ATR-IR spectra of N-modified UiO-66 MOFs before and after SO_2 exposure. 144
Figure C-5: Structure of the ML_3 cluster model. 144
Figure C-6: Linear relationship between $T\Delta S_{bind}$ (T=298K) and ΔE_{bind} for SO_2 adsorption in UiO-66 type MOFs. 147

LIST OF SYMBOLS AND ABBREVIATIONS

SO_2	Sulfur dioxide
EPA	Environmental Protection Agency
WHO	World Health Organization
g/m^3	gram per cubic metre
ppb	parts of per billion
CO_2	Carbon dioxide
H_2SO_4	Sulfuric acid
ppm	parts per million
FGD	Flue gas desulfurization
AC	Activated carbon
CNTs	Carbon nanotubes
BET	Brunauer–Emmett–Teller
MIL	Material Institute Lavoisier
MFM	Manchester Framework Material
UiO	University of Oslo
BTC	1,3,5-benzene tricarboxylic acid

BDC	Terephthalic acid
ED	Ethylenediamine
PMIDA	N-(phosphonomethyl)iminodiacetic acid
CH_4	Methane
PXRD	Powder X-ray diffraction
N_{av}	Avogadro number
TGA	Thermogravimetric analysis
BDC-$(COOH)_2$	1,2,4,5-Benzenetetracarboxylic Acid
OMSs	Open metal sites
Me-BTC	Trimethyl 1,3,5-benzenetricarboxylate
DMF	Dimethylformamide
Al	Aluminum
Sc	Scandium
V	Vanadium
Fe	Iron
In	Indium
Ga	Gallium
DMA	N-N dimethylacetamide

IAST	Ideal Adsorbed Solution Theory
DFT	Density functional theory
ILs	Ionic liquids
DETA	Diethylenetriamine
TETA	Tris(2-aminoethyl)amine
Ace	Acetate
Lac	Lactate
XPS	X-ray photoelectron spectroscopy
DRIFTS	Diffuse reflectance infrared Fourier transform spectroscopy
BDC-NH_2	2-Aminoterephthalic Acid
BDC-NO_2	2-Nitroterephthalic acid
$ZrCl_4$	Zirconium chloride
2,5-PDC	2,5-Pyridinedicarboxylic acid
2,5-PziDC	2,5-Pyrazinedicarboxylic acid
3,5-PzoDC	3,5-Pyrazoledicarboxylic acid
1,3-BDC	Isophthalic acid
1,3-BDC-NH_2	5-Aminoisophthalic acid

3,5-PDC	3,5-Pyridinedicarboxylic acid
CAU	Christian-Albrechts-University

SUMMARY

Continued intensive combustion of fossil fuels has caused the increase of sulfur dioxide (SO_2) concentration in the air, which has been considered one of the primary pollutants responsible for human health problems like respiratory disease and environmental issues. Unfortunately, the burning of fossil fuels or the production of flue gas containing SO_2 is unavoidable considering that currently more than 80% of global energy is supplied by fossil fuels and the transition to renewable energy is progressing slowly. Therefore, it is essential to conduct flue gas desulfurization before its emission. Conventional techniques deployed for flue gas desulfurization are ammonia or limestone scrubbing of the exhaust gas. However, these SO_2 scrubbing processes suffer from several drawbacks such as intensive energy, corrosion of pipelines, and production of tons of low-grade byproducts.

Metal organic frameworks (MOFs) have attracted considerable interest in the scientific community for gas separations. Briefly, MOFs are a class of highly crystalline and porous materials comprised of metal or oxometallate nodes and organic ligands forming a periodic porous structure. Due to features such as high surface area, high porosity, and designable chemistries, MOFs show intriguing potential for being used as selective SO_2 sorbents. In this dissertation, we focus on three types of MOF modifications: metal substitution in OMS MOFs, ionic liquid coordination to OMS, and ligand functionalization. This objective is to understand the ability of these modifications to tune and enhance adsorption properties of MOFs for SO_2 capture.

MOFs possessing coordinatively unsaturated metal sites (referred to as open metal sites, OMSs) have been observed to exhibit high affinity to specific gas molecules. The presence of unsaturated metal sites with accessible coordination vacancies allows for strong interactions, such as coordination bonds, electrostatic interactions, or dipole-dipole interactions, between the gas molecules and the OMSs. This results in enhanced adsorption of gases within the MOF framework. Furthermore, the unique properties of OMSs can facilitate selective gas adsorption. The presence of OMSs with tailored properties enables preferential adsorption of specific gases over others. This selectivity arises from the specific interactions between the gas molecules and the OMSs, such as size, shape, or electronic matching. In Chapter 3, we focus on the open trivalent metal sites on MIL-100-M (where M = Al, Sc, V, Fe, and In.) and aim to reveal the effect of trivalent metal sites on SO_2 adsorption. Moreover, the water stability problem of MOFs featuring OMSs is also addressed by a post-synthetic metal insertion process.

Post-synthetic modification through OMSs provides a versatile and effective approach to tailor MOFs for specific applications. It involves introducing additional functional groups or species onto the MOF structure after its synthesis. This strategy allows for the customization and enhancement of MOF properties for gas separation. It enables the introduction of additional functional groups or active sites, which can enhance the MOF's adsorption capacity, selectivity, or catalytic activity. These functional groups can interact with target molecules, such as gases or pollutants, improving the performance of the MOF. Additionally, post modification through OMSs offers a way to address stability concerns associated with MOFs containing exposed metal sites. OMSs can initiate framework degradation or unwanted reactions with moisture or other reactive species. By

post-synthetic modifying the MOF structure, stability can be improved through the coordination or bonding of additional functional groups, protecting the OMSs and enhancing the overall robustness of the MOF material. In Chapter 4, ionic liquids (ILs) containing nitrogen functional sites are introduced post-synthesis into MIL-101 to improve the capacity and selectivity for SO_2 capture. Furthermore, by coordinating with the open metal sites, the ILs effectively protect the framework from the intrusion of "invader" molecules, further enhancing the material's stability.

Lastly, the ligand functionalization of MOFs is one of the most common and efficient approaches that can enhance MOFs properties over the parent material for adsorption-based separations. The decorated functional sites on ligands play a crucial role in determining the adsorptive capacity and selectivity by dictating the type of adsorbent-adsorbate interaction, and consequently the enthalpy of adsorption. Amongst this field, incorporating nitrogen-based sites on MOF ligands has proven a feasible approach for achieving the desired affinity for CO_2 or water molecules at low relative pressures. Chapter 5 investigates the effect of a variety of nitrogen sites on MOFs ligands on SO_2 capture and provides insights into establishing basic rules for the design of MOFs with N-containing functional groups for SO_2 adsorption.

In summary, by exploring three distinct categories of modifications for Metal-Organic Frameworks (MOFs), namely the substitution of metals in OMS MOFs, coordination of ionic liquids to OMS, and functionalization of ligands, this dissertation delves into the intricacies of these modifications and their impact on enhancing the adsorption properties of MOFs and develops the possible strategies that can be applied to tune MOFs properties effectively and designedly for SO_2 adsorption.

CHAPTER 1. INTRODUCTION

1.1 Flue gas desulfurization

1.1.1 Sulfur dioxide (SO_2)

SO_2 is a colourless gas with a pungent, irritating odour. It is a common air pollutant that is primarily produced by the burning of fossil fuels, such as coal and oil, in power plants and other industrial processes. SO_2 can also be produced naturally by volcanic activity and wildfires. In small amounts (at about 15 ppb)[1], SO_2 is a normal component of the atmosphere, but in high concentrations, it can be harmful to human health and the environment.

SO_2 is a highly reactive gas that can undergo a variety of chemical reactions in the atmosphere. In the presence of sunlight, it can react with other compounds to form sulfuric acid (H_2SO_4), which can contribute to the formation of acid rain. Acid rain can damage crops, forests, and buildings, and can make bodies of water too acidic to support aquatic life.[2] SO_2 can also react with oxygen in the atmosphere to form sulfur trioxide (SO_3), which can contribute to the formation of particulate matter (i.e., tiny particles suspended in the air). Therefore, the emission of SO_2 can cause respiratory problems, especially in people with pre-existing respiratory conditions such as asthma. Research reveals that concentrations of SO_2 of 100 ppm or greater have been designated immediately dangerous to life or health.[3] For that reason, SO_2 has been considered a criteria air pollutant by the U.S. Environmental Protection Agency (EPA) and is regulated under the Clean Air Act to protect human health and the environment. According to the policies standardized by U.S. EPA and World Health Organization (WHO), the maximum exposure levels for humans are 20 g/m^3 (8 ppb) for daily averages and 500 g/m^3 (175 ppb) over a period of 10 minutes.[4]

Nonetheless, SO_2 plays an important role in industrial manufacturing. SO_2 can be used as a reducing agent in chemical reactions due to its ability to donate electrons. Specifically, it is a useful reducing bleach for papers and delicate materials such as clothes. SO_2 can also be used in the production of sulfuric acid, which is a key industrial chemical used in the production of fertilizers, batteries, and other products. In 2021, the global market volume of sulfuric acid amounted to around 260 million metric tons, and it is forecast to surpass 300 million metric tons by 2028. By that same year, the market value of sulfuric acid is expected to surpass 12 billion U.S. dollars.[5]

1.1.2 Flue gas

Figure 1-1 illustrates the global contributions of major industry sectors and natural sources (volcanoes) to total SO_2 emissions in 2019. Flue gas is the biggest source of SO_2 in the air. Flue gas is the gas that is emitted from combustion processes, such as the burning of fossil fuels in power plants and industrial processes. It is typically composed of nitrogen, carbon dioxide (CO_2), water vapor, and small amounts of other gases, such as SO_2, nitrogen oxides (NOx), and carbon monoxide (CO).

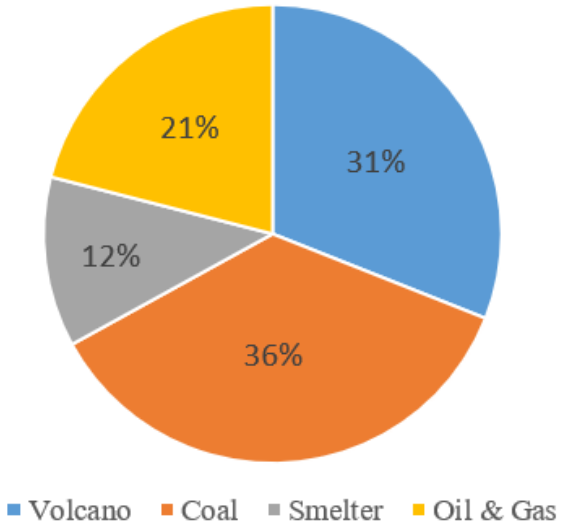

Figure 1-1: Global contributions of major industry sectors and natural sources (volcanoes) to total SO_2 emissions in 2019. Image reproduced from Dahiya[6]

The concentration of SO_2 in flue gas can vary widely depending on the type of fuel burned and the type of combustion process used. The concentration of SO_2 in a typical flue gas can range from a few parts per million (ppm) to several thousand ppm (See in Table 1-1.). For example, the concentration of SO_2 in the flue gas of a coal-fired power plant can be as high as several thousand ppm[7], whereas the concentration of SO_2 in the flue gas of a natural gas-fired power plant is generally much lower, typically less than 100 ppm[8].

Table 1-1: A typical flue gas compositions

Components	Percentage
SO_2	0.05-0.3% (500-3000 ppm)
CO_2	10-15%
H_2O	5-7%
O_2	3-4%
N_2	~75%

Compared to other components, there is only a tiny percentage of SO_2 in the flue gas. However, considering the standards set by U.S. EPA and WHO (8 ppb for daily averages and 175 ppb over 10 minutes), the concentration of SO_2 is substantial and can cause great harm to humans and the environment. In 2020, approximately 1.7 million tons of SO_2 were emitted in the U.S., and globally, it was about 40 million tons of SO_2. Historically, well-known smog events such as the Maas Valley haze, the London smog, and the Donora smog have all been associated with SO_2 contamination.[9] Moreover, the burning of fossil fuels or the production of flue gas containing SO_2 is unavoidable considering that currently more than 80% of global energy is supplied by fossil fuels and the transition to renewable energy is progressing slowly. Thus, flue gas desulfurization must be carried out before its emission, which is critical to environmental protection and human health.

1.1.3 Flue gas desulfurization

Flue gas desulfurization (FGD) is the approach most frequently utilized to mitigate the SO_2 problem at the industrial level due to its simplicity and high desulfurization efficiency.[10] FGD works by using a chemical process to convert the SO_2 in the flue gas into a liquid or solid compound that can be removed from the gas stream. Based on the condition of sorbents, FGD can be classified into dry, semi-dry, and wet methods. The most common FGD method is the wet scrubbing process which involves a gas-liquid reaction.

Wet scrubbing is likely to be the most reliable at removing up to 95% of the SO_2 from flue gas, and it is the most widely used FGD technology in power plants and other industrial processes around the world.[11-12] Wet scrubbing processes generally introduce SO_2 into slurries containing alkaline absorption media, as such, acid gases are neutralized through acid-base reactions. It can provide a wide range of chemical reagents as absorbing liquids, such as sodium hydroxide[13], calcium-based solution[14], and amine-based solvents[15]. Because of the presence of alkaline compounds, the wet scrubber can act as a buffer that keeps the pH level favourable for SO_2 absorption. Among these different kinds of wet absorbents, limestone takes the lead and accounts for around 50% of the global FGD market owing to the availability and relative low cost of limestone. The limestone wet scrubbing process typically involves several stages, including absorption, oxidation, and neutralization as shown in Figure 1-1. During the absorption stage, the slurry of limestone or lime and water is sprayed into the flue gas stream, and the SO_2 is absorbed into the slurry. In the oxidation stage, the slurry is mixed with air, which converts the SO_2 into H_2SO_4. Finally, in the neutralization stage, the slurry is treated with an alkali, such as caustic soda (NaOH), which neutralizes the acid and produces the gypsum. However, limestone is not

regenerative, and the method produces tremendous wastewater. Moreover, the byproduct gypsum may pollute the environment.

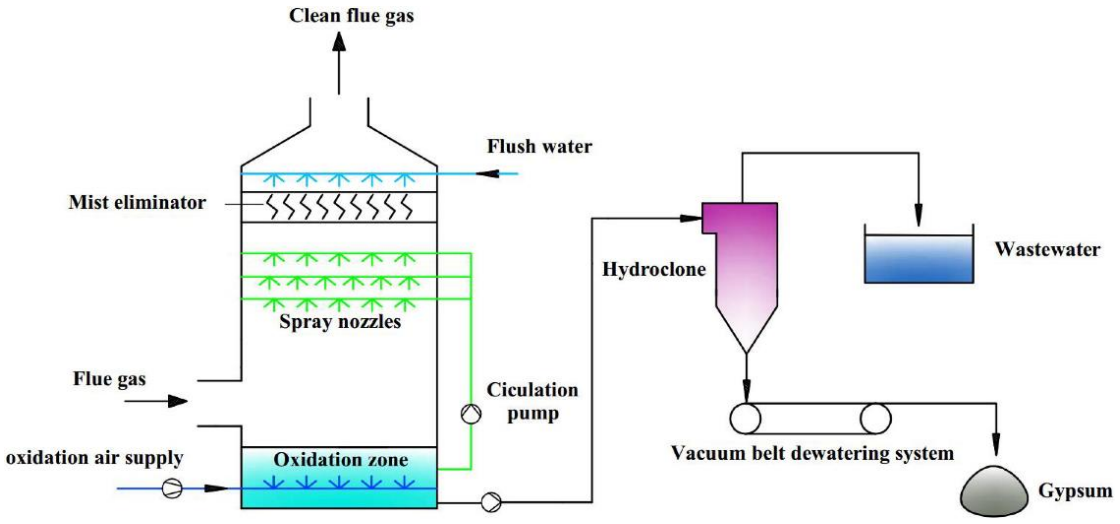

Figure 1-2: Schematic diagram of wet scrubbing process for FGD. Image reproduced from Duan and Anthony[16]

Amine-based absorbent wet scrubbing is another competitive and mature technique to realize FGD. As early as 1940, a process with dimethylaniline for SO_2 removal had already been patented.[17] The presence of amine can increase the quantity of SO_2 dissolved in water, resulting in a high absorption capacity. The key advantages of amine-based absorbents over limestone are their regenerability and selectivity. Dan and coworkers employed a mixture of N-methylated ethylene imine polymer and 1-ethyl-3-methylimidazolium tetrazolate capturing low-concentration SO_2.[18] It demonstrated that the amine mixture exhibited a stronger affinity towards SO_2 with a solubility of 0.308 g/g (SO_2/absorbent), and can maintain its absorption performance after regeneration. An amino silane absorbent named DTSMA reported by Hao and coworkers can be not only almost regenerated within just 60 minutes at 100 °C after SO_2 absorption, but also exhibited selective absorption towards SO_2 in the presence of CO_2.[19] However, their practical application has been

limited due to the poor SO_2 uptakes, the serious volatile loss of solvents, and the required intensive energy for solvent regeneration.

1.2 Adsorption

Adsorption is the process by which a substance, called the adsorbate, adheres to the surface of a solid material, referred to as the adsorbent. The attraction between the adsorbate and the adsorbent can be due to a range of forces, such as van der Waals forces, hydrogen-bonding, or electrostatic interactions. The adsorption process can be categorized as physical or chemical, depending on the nature of the adsorbate and adsorbent. Physical adsorption is driven by weak intermolecular forces and can be easily reversed by changing the conditions of the system, such as temperature or pressure. In contrast, chemical adsorption involves a stronger chemical bond that is more difficult to break.

Gas separation has been a major application of adsorption. Adsorption is a more selective process compared to absorption, as it can be used to selectively remove specific gases from a gas stream. The adsorbent material has a high surface area and can selectively adsorb certain gas molecules while allowing others to pass through. The selectivity of the adsorbent material depends on the size and shape of the gas molecules as well as the surface chemistry of the adsorbent. Different types of adsorbents can be used for different gas separation requirements.

1.2.1 Adsorption for flue gas desulfurization

Adsorption is an effective and efficient technique for FGD, offering a promising solution for reducing SO_2 emissions from industrial processes. In FGD using adsorption, a solid adsorbent material is used to selectively adsorb SO_2 from the flue gas. Adsorption FGD has several

advantages over traditional wet scrubbing techniques. It does not require the use of water or produce a wastewater stream, making it more environmentally friendly. It also has a smaller footprint and requires less maintenance compared to wet scrubbing systems. However, it can be more expensive to operate and requires careful selection of adsorbent materials for optimal performance. The most common adsorbent materials used for FGD are activated carbon, zeolites, and metal oxides. These materials have a high surface area, which provides ample space for the SO_2 molecules to adsorb onto the surface.

1.2.1.1 Carbon materials

Carbon-based adsorbents are the preferred materials for removing SO_2 through adsorption due to their excellent physical and chemical stability to high temperature and corrosive gases. A wide variety of carbon materials (Figure 1-3) have been investigated for SO_2 adsorption, such as activated carbon (AC)[20-21], carbon nanotubes (CNTs)[22], and graphene oxide (GO)[23].

Activated carbon (AC) refers to a type of black carbonaceous porous solid material with high porosity and large surface areas. It is the most common adsorbent used for gas adsorption and is often considered a benchmark material to verify the adsorption performance of new adsorbent materials. The global AC production was estimated at 5.4 million metric tons and is projected to be around 9 million metric tons by 2029. A significant application segment for the AC demand is gas adsorption.

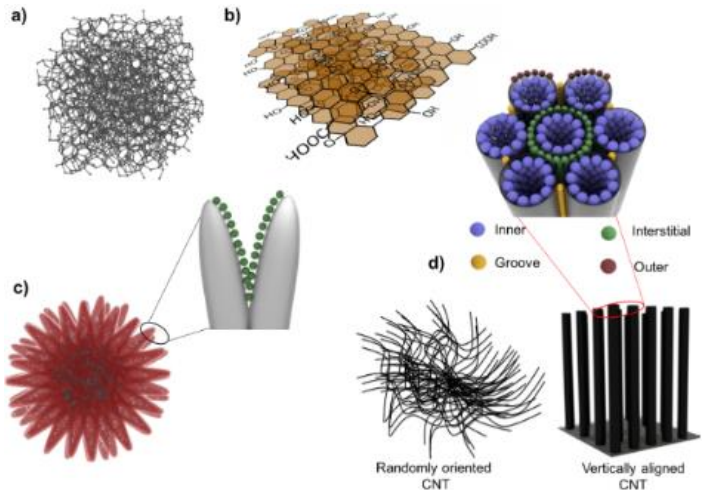

Figure 1-3: Schematic of different carbon-based adsorbents: a) activated carbon, b) graphene oxide, GO; c) carbon nano-horns, d) carbon nanotubes. Image reproduced from Babu and Schneider[24]

The synthesis of AC consists of two fundamental steps: carbonization and activation. Carbonization aims to decrease the volatile components of raw materials by subjecting them to pyrolysis, resulting in the production of char that has a substantial amount of fixed carbon and primary porosity. In contrast, activation seeks to enhance the specific surface area or pore volume of AC.[25] In general, AC can adsorb between 5% to 50% of its weight in gas, depending on factors such as the type of AC precursors, the size and shape of the AC particles, and the operation conditions. Adsorption of SO_2 in AC has been studied extensively, and considerations were made for several factors, such as porosity, surface chemistry, and constituents of ash.[21, 26-30] However, low percentage of SO_2 in flue gas is a significant challenge for AC due to the weak interaction between AC surface with SO_2. To overcome this shortcoming, extra surface modifications were applied, nonetheless, the post-developed functional groups or sites were generally less reactive or unstable. [31]

Carbon nanotubes (CNTs), a type of cylindrical carbon-based nanomaterials have shown promising potential as a material for SO_2 capture due to their high surface area, unique morphology, and high chemical stability.[22, 32] However, there are several drawbacks that need to be considered when applying for SO_2 capture. CNTs have a lower selectivity for SO_2 capture compared to other gases, and their production is expensive and not scalable for industrial-scale applications. Furthermore, CNTs require functionalization to improve their SO_2 capture capacity and selectivity, making the synthesis process complex and costly. Additionally, CNTs are highly sensitive to moisture, which can limit their use in humid environments or require additional steps to remove moisture. Moreover, CNTs pose potential health and environmental risks, such as respiratory toxicity and ecological impacts, requiring proper handling and disposal procedures.

1.2.1.2 Zeolites

Zeolites are a group of natural (about 40 identified in the past 200 years) or synthetic (more than 150) minerals with a unique, crystalline structure characterized by a three-dimensional tetrahedral network of interconnected channels and pores.[33] They are typically tetrahedral units composed of aluminum, silicon, and oxygen atoms, with other elements such as sodium, potassium, and calcium often present (See in Figure 1-4). One of the most important properties of zeolites is their uniformly distributed pore structure that enables them function as molecule sieves to separate specific molecules from molecule mixtures based on their size, shape, and polarity. This makes them attractive and useful in a wide range of industrial applications, including catalysis, gas separation, and water purification.[34-37]

Zeolites offer numerous advantages for gas adsorption, including high selectivity, outstanding capacity, and remarkable chemical stability, which make them an adaptable and

efficient adsorbent for gas separation and purification. Their unique sieving mechanism allows them to achieve high selectivity to certain gas molecules, while their vast surface area enables them to adsorb substantial amounts of gas per unit of weight or volume. Zeolites usually exhibit remarkable chemical stability, and can endure a broad range of operating conditions, even in harsh industrial environments such as high temperatures, acidic or basic environments, and exposure to corrosive gases.

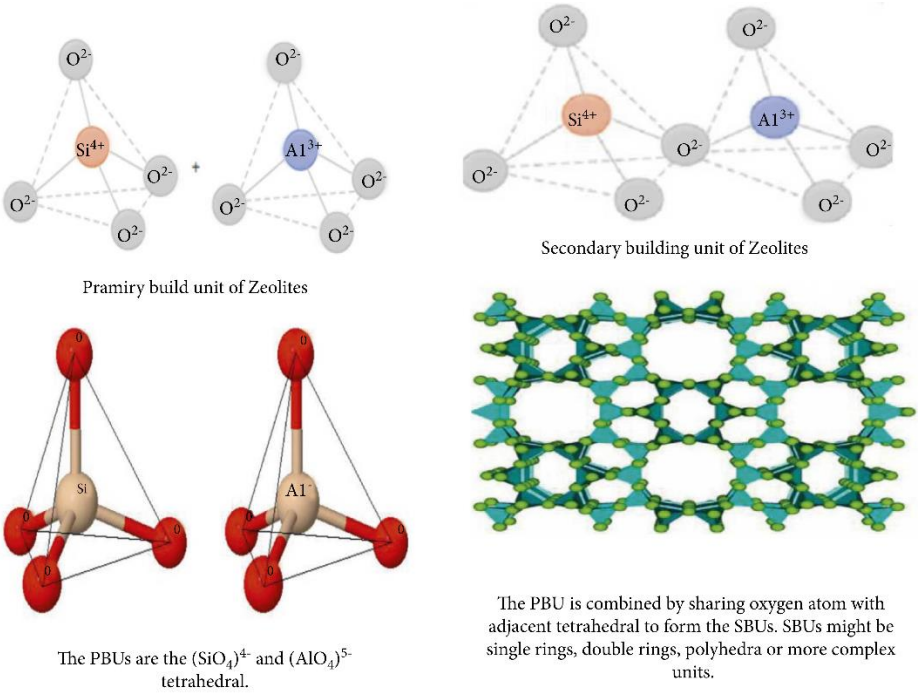

Figure 1-4: Structure diagram of zeolites. Image reproduced from Derbe and Bitew[37]

Zeolites have shown promise as an effective adsorbent for FGD, owing to their favorable characteristics. According to a study by Mohammad et al., the small size of zeolites contributes to their ability to efficiently remove SO_2, while also exhibiting strong thermal regeneration capabilities.[38] Similarly, Marcu and Sandulescu investigated the use of Y type zeolites for SO_2 adsorption, concluding that the adsorbed SO_2 molecule is likely anchored to one or two hydroxyl groups on the zeolite's surface through hydrogen-bonding.[39] In addition to their adsorption

properties, zeolites can serve as catalyst supports for the reactive adsorption of SO_2, as demonstrated by previous research[40-42]. Unfortunately, zeolites often cannot achieve a high level of selectivity for SO_2 over CO_2 due to the challenge of molecular sieving, which cannot effectively separate gases with similar molecular sizes.

1.3 Metal-organic frameworks

Metal-Organic Frameworks (MOFs) are a type of crystalline porous material made up of metal ions or clusters linked together by organic ligands. Figure 1-5 illustrates the MOFs structure and some representative MOFs. The synthesis of MOFs typically involves mixing the metal ions or clusters with the organic ligands in a solvent and allowing them to self-assemble into a three-dimensional framework. The earliest report of MOFs[43] can be traced back to 1995 when a research group led by Professor Omar M. Yaghi at Arizona State University and Lawrence Berkeley National Laboratory synthesized a new porous material, denoted as MOF-5. The material was made by linking zinc oxide clusters with terephthalic acid ligands, forming a highly ordered porous framework. This discovery opened up a new avenue for designing and synthesizing a wide range of porous materials with tunable properties and diverse applications.[44-47] Since then, MOFs have become a rapidly growing field of research, attracting significant interest from scientists and engineers around the world.

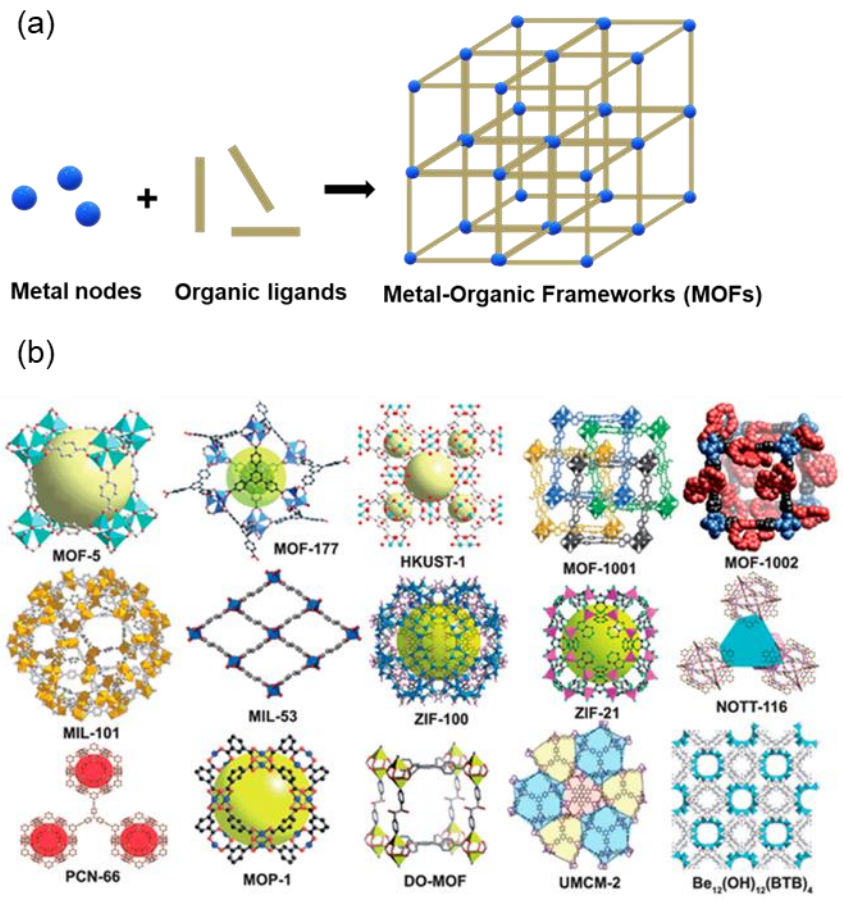

Figure 1-5: (a) Schematic of the metal-organic frameworks (MOFs) structure. (b) Structures of common MOFs. Image reproduced from Kampouraki and Deliyanni[48]

As implied by MOFs' name, MOFs bring together metal and organic components to leverage the most desirable qualities of both. Therefore, the choice of metal ions and organic ligands used in the synthesis of MOFs can have a significant impact on the properties of the resulting material. Various metal ions (about eighty-four metals are listed on the periodic table) can be used, including zinc, copper, zirconium, and iron, while there are thousands of unique organic bridging ligands that can be used for the construction of MOFs, such as carboxylates, amines, and pyridines. The fine-tuning of their functionalities for desired applications can be readily established by varying the type of metal nodes or organic ligands for MOFs' synthesis. Post-synthesis modification of established MOFs can be another powerful tactic to achieve novel

structures with targeted chemical properties for MOFs. This technique proves particularly advantageous in cases where incorporating specific functional groups through direct synthesis is challenging or unfeasible. Obstacles may arise due to the instability or insolubility of the precursors, their unfavorable secondary reactivity, or the incompatibility of functional groups with the required synthesis conditions. By replacing the metal nodes or organic linkers, or by functionalizing them, MOFs can undergo post-synthetic transformations.[49-52]

1.3.1 MOFs for gas adsorption

Extensive research has been carried out on MOFs due to their exceptional capacity for adsorption (See in Figure 1-6). The process of gas adsorption in MOFs involves trapping gas molecules within the material's pores. The adsorption mechanism can be regulated by altering the metal ion and organic molecule constituents or adjusting the pore size and surface functional groups of the MOFs. This enables the targeted adsorption of particular gases. Additionally, MOFs offer the benefit of having a high adsorption capacity. With surface areas ranging from hundreds to thousands of square meters per gram, MOFs provide ample room for gas molecules to adsorb.

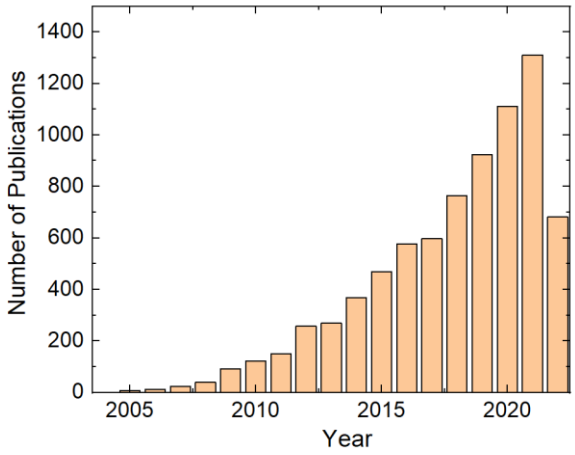

Figure 1-6: Number of publications of MOFs for gas adsorption (Data from Web of Science, until May 2022).

MOFs have shown potential for a variety of gas adsorption and separation applications, including CO_2 capture, H_2 storage, water harvesting, and natural gas purification.[53-55] Table 1-2 lists specific gas processing applications for MOFs. MOFs possessing extensive surface areas have been utilized for capturing and concentrating CO_2, and subsequently for its storage and transportation. As an example, employing MOF-177, a MOF material having a Brunauer–Emmett–Teller (BET) surface area of 4500 m^2/g, in a gas cylinder can trap and store approximately nine times the amount of CO_2 compared to the same cylinder without the MOF-177.[56] MOFs have been investigated as potential materials for hydrogen storage. At a temperature of -196 °C and a pressure of 100 bar, MOFs have surpassed the 2020 onboard gravimetric hydrogen storage technical targets (4.5 wt%) set by the US Department of Energy (DOE).[57] Although MOFs are not yet able to do so at ambient conditions, with continued advancements in MOF design and synthesis, they may become a viable option for hydrogen storage in the future. The potential for natural gas purification using MOFs is also remarkably promising.[58-60]

Table 1-2: List of MOFs for specific gas adsorption/separation

Gas processing	MOFs(performance)	Ref.
CO_2 adsorption	Mg-MOF-74 (37.8 wt% at 25 ℃ and 1 bar) CAU-1 (15 wt% at 25 ℃ and 1 bar) Zn-BTZ (18 wt% at 25 ℃ and 1 bar)	61-63
CO_2/N_2 separation	Bio-MOF-11 (a selectivity of 75) CuBTTri (a selectivity of 327)	64-65
CH_4 storage	HKUST-1 (227 cm^3/cm^3 at 25 ℃ and 35 bar) Ni-MOF-74 (230 cm^3/cm^3 at 25 ℃ and 35 bar) PCN-11 (194 cm^3/cm^3 at 25 ℃ and 35 bar) NOTT-103 (193 cm^3/cm^3 at 25 ℃ and 35 bar)	66-69
H_2 storage	MIL-100 (1.9 wt% at -196 ℃ and 1 bar) HKUST-1 (2.9 wt% at -196 ℃ and 1 bar) NOTT-103 (2.56 wt% at -196 ℃ and 1 bar) PCN-12 (3.05 wt% at -196 ℃ and 1 bar)	70-73
H_2O capture	MIL-160 (35 wt% at P/P0 = 0.4) Cr-soc-MOF-1 (75 wt% at P/P0 = 0.4)	74-77

	DUT-67 (48 wt% at P/P0 = 0.4)	
	MOF-303 (33 wt% at P/P0 = 0.4)	
NH_3 adsorption	UiO-66-OH (5.7 mmol/g at 25 ℃ and 1 bar)	78-80
	HKUST-1 (6.8 mmol/g at 25 ℃ and 1 bar)	
	Ni_2Cl_2-BBTA (12.2 mmol/g at 25 ℃ and 1 bar)	
CO adsorption	Fe_2-DOBDC (6 mmol/g at 25 ℃ and 1 bar)	81-82
	Co-MOF-74 (5.8 mmol/g at 25 ℃ and 1 bar)	
	Cu-AIP-H_2O (7.8 mmol/g at 25 ℃ and 1 bar)	
C_2H_6/C_2H_4 separation	ZIF-7 (a selectivity of 2.5)	83-86
	MAF-49 (a selectivity of 2.7)	
	NIIC-20-GI (a selectivity of 8.7)	
	Co-AIN_2 (a selectivity of 3)	

1.3.2 MOFs for flue gas desulfurization and challenges

MOFs have been explored for use in flue gas desulfurization and have exhibited unprecedentedly high performance. The porous structure and high surface area of MOFs make them suitable for the adsorption of SO_2 from flue gas emissions. Several studies have demonstrated the potential of MOFs for FGD. For example, a study conducted by researchers at Tongji University showed that two Al-based MOFs (MIL-160 (MIL stands for Material Institute Lavoisier) and MFM-300 (MFM stands for Manchester Framework Material)) were able to

selectively adsorb SO_2 from simulated SO_2/CO_2 mixture streams.[87] According to the findings, MIL-160 exhibited exceptional selectivity for SO_2/CO_2, reaching a value of 220 at 25 ℃ and 1 bar, which was significantly higher than the selectivity of MFM-300, which was found to be 53. The study revealed that the furan oxygen responsible for SO_2 binding in MIL-160 showed a stronger affinity than the hydroxyl groups found in MFM-300. The study also found that the presence of H_2O in the streams can dramatically reduce the capacity of SO_2 in MOFs. Another study conducted by Chen and co-workers at Institute of Zhejiang University, explored the use of a family of isostructural gallate-based MOFs with an ample number of hydrogen bond donors lining the pore channel for SO_2 capture.[88] The study reported that these MOFs can selectively absorb SO_2 and resulted in a tight packing of SO_2 through multiple hydrogen-bonding interactions. Notably, Co-gallate MOFs demonstrated an outstanding ultrahigh SO_2 adsorption uptake at an extremely low pressure of 0.002 bar, with a value of 6.13 mmol/cm, surpassing all other state-of-the-art MOFs reported to date. The researchers also noted that the use of MOFs for FGD could potentially reduce the energy consumption and cost associated with traditional wet scrubbing techniques.

Despite the promising results of these studies, in the context of flue gas desulfurization, MOFs must meet several requirements to be effective in capturing SO_2. Firstly, MOFs with a high affinity for SO_2 are necessary. The requirement for MOFs with high affinity for SO_2 is due to the low concentration of this gas in flue gas emissions, which can range from less than 1% to as low as 0.04%. High affinity ensures that the MOFs can effectively capture SO_2 from the flue gas stream. However, it is important to note that excessive binding could result in irreversible adsorption, which can reduce the MOF's capacity to capture SO_2 and make it difficult to regenerate the material for reuse. Moreover, the presence of CO_2 in flue gas is another important factor to

consider. Since MOFs are porous materials, they can potentially capture other gases, including CO_2. This can lead to a reduced capacity for SO_2 capture, as well as additional energy costs associated with separating the captured gases. Therefore, MOFs must have high selectivity for SO_2 over CO_2 to ensure efficient and selective capture of SO_2. In addition to these factors, the reaction of SO_2 with oxygen and water in flue gas can lead to the formation of sulfur acid, which is a highly corrosive substance that can damage the MOF material. This can lead to a loss of porosity and surface area, reducing the MOF's ability to adsorb gases. Therefore, MOFs employed for flue gas desulfurization must exhibit strong chemical and physical stability to withstand these harsh conditions and avoid degradation.

Overall, achieving optimal performance and effective capture of SO_2 from flue gas emissions requires a careful balance of factors such as affinity, selectivity, and stability. The design and selection of MOFs for this application must be based on a thorough understanding of the underlying principles of gas adsorption and the specific requirements of the process. By addressing these key factors, MOFs can offer a promising solution for the removing SO_2 selectively, quantitatively, and preferably reversibly from flue gas emissions and contribute to a cleaner and more sustainable environment.

1.4 Dissertation overview

This dissertation aims to learn the fundamental principles of MOFs for SO_2 adsorption and provide insight into MOF design for specific gas capture by studying (1) the interaction between trivalent metals with SO_2 molecules, (2) the enhancement of SO_2 capture by post-modified MOFs with ionic liquids, and (3) the effect of various nitrogen sites on MOF linkers for SO_2 adsorption.

Chapter 3 focuses on the relationship between the nature of trivalent metals on MOFs with SO_2. A series of MIL-100-M MOFs were synthesized as the platform to examine the interaction between trivalent metals on MOFs with adsorbed SO_2 molecules. MIL-100 MOFs had been chosen because they can be made of a variety of trivalent metals, and those trivalent metal sites can be released after a simple activation process. The capacity, selectivity, and stability of these MOFs were investigated. It was found that MIL-100-Sc was the best adsorbent candidate for SO_2 capture with high uptake at low partial pressures, remarkably IAST selective values to SO_2 over CO_2, and strong stability to humid SO_2 exposure. The high SO_2 capture capability may contribute to the less electronegativity of Sc. The metal insertion process for the function of trivalent metals on MOFs were then evaluated. To avoid the stability challenge of MOFs with open metal sites (OMSs) while maintaining the functions of OMSs, UiO-66-2COOH (UiO stands for University of Oslo) was selected as a parent MOFs for extra metal sites impregnation. Among all UiO-66-2COOM samples, UiO-66-2COOSc demonstrated the highest capacity as the same MIL-100-Sc was the best in MIL-100-M MOFs. The results proved that the functionality of OMSs on MOFs can be mimicked through metal insertion processes.

Chapter 4 aims to inspect the practicality of using MOFs as amine compound supports for enhanced SO_2 adsorption at low partial pressures. Taking the advantage of the OMSs on MIL-101 with large pore volumes, diethylenetriamine (DETA) and their corresponding ion liquids were introduced into MIL-101 and stabilized through the coordination of open metal sites Chromium and nitrogen sites on the post-introduced compounds. The introduction of these ILs post-synthesis led to remarkable improvements in SO_2 adsorption capacity compared to MIL-101. This can be attributed to the presence of functional sites on the ILs, which enhance the affinity between the framework and SO_2 molecules. Notably, among the modified composites, MIL-101-DETA-Lac

displayed an unprecedented IAST selectivity of a thousand-fold towards SO_2 compared to CO_2. This underscores the significant impact that the choice of IL anion can have on the material's properties. Furthermore, the post-introduced ILs also contribute to the stability of the MOFs. By coordinating with the open metal sites, the ILs effectively protect the framework from the intrusion of "invader" molecules, further enhancing the material's stability.

Chapter 5 explores the effect of different nitrogen sites on MOFs for SO_2 adsorption. A series of nitrogen-modified (N-modified) UiO-66 MOFs were synthesized with ligands containing different N sites (amino, nitro, pyridine, pyrazine, and pyrazole) and their SO_2 adsorption behaviors have been examined for this chapter. SO_2 isotherms and Ideal Adsorbed Solution Theory (IAST) calculation revealed that pyridine exhibited higher affinity toward SO_2 than that of amino and pyrazine. ATR-IR experiments showed that the introduced N sites can act as favorable adsorption sites for SO_2. These results were also supported by first-principles calculations. Energy decomposition and natural bond orbital analyses highlighted the influence of chemical environment (like symmetry) of linkers on the overall adsorption behaviors of MOFs. To check if this trend is applicable for other MOFs or other functional sites, CAU-10 MOFs were prepared with pyridine-N and amino-N, furan-O and hydroxyl-O. Results showed that CAU-10-pyridine-N and CAU-10-furan-O adsorbed more SO_2 than their counterparts, respectively. Overall, this study provides insights into establishing basic rules for the design of MOFs with N-containing functional groups for SO_2 adsorption.

Altogether, this dissertation research first focused on understanding the relationship between OMSs on MOFs with adsorbed SO_2, found out the stability would be a big concern for MOFs with OMSs. Then, we modified MOFs with extra functional sites by making use of the OMSs while avoiding stability issues and learned that nitrogen sites can be favorable for SO_2 capture. Last, we

synthesized MOFs decorated with distinct nitrogen sites by one-post synthesis methods eluding post modification and verified that functional sites in heterocyclic aromatic rings are more beneficial for SO_2 adsorption. The aim of this work is to offer comprehension and elucidation on the utilization of MOF-based materials in SO_2 capture, and to identify strategies that can improve the performance and applicability of MOFs.

1.5 References

1. U.S.EPA, Sulfur Dioxide Trends. **2021**.

2. Grennfelt, P.; Engleryd, A.; Forsius, M.; Hov, Ø.; Rodhe, H.; Cowling, E., Acid rain and air pollution: 50 years of progress in environmental science and policy. *Ambio* **2020,** *49*, 849-864.

3. Pohl, H. R., Toxicological profile for sulfur dioxide. **1998**.

4. Martínez-Ahumada, E.; López-Olvera, A.; Jancik, V.; Sánchez-Bautista, J. E.; González-Zamora, E.; Martis, V.; Williams, D. R.; Ibarra, I. A., MOF Materials for the Capture of Highly Toxic H_2S and SO_2. *Organometallics* **2020,** *39* (7), 883-915.

5. U.S.DOI, U.S. Geological Survey: mineral commodity summaries **2023**.

6. Dahiya, S.; Anhäuser, A.; Farrow, A.; Thieriot, H.; Kumar, A.; Myllyvirta, L., Ranking the World's Sulfur Dioxide (SO_2) Hotspots: 2019–2020. *Delhi Center for Research on Energy and Clean Air-Greenpeace India: Chennai, India* **2020,** *48*.

7. Lee, J.-Y.; Keener, T. C.; Yang, Y. J., Potential flue gas impurities in carbon dioxide streams separated from coal-fired power plants. *Journal of the Air & Waste Management Association* **2009,** *59* (6), 725-732.

8. Nurhisanah, S.; Hasyim, H., Environmental health risk assessment of sulfur dioxide (SO_2) at workers around in combined cycle power plant (CCPP). *Heliyon* **2022,** *8* (5), e09388.

9. Li, X.; Han, J.; Liu, Y.; Dou, Z.; Zhang, T.-a., Summary of research progress on industrial flue gas desulfurization technology. *Separation and Purification Technology* **2022,** *281*, 119849.

10. Hanif, M. A.; Ibrahim, N.; Abdul Jalil, A., Sulfur dioxide removal: An overview of regenerative flue gas desulfurization and factors affecting desulfurization capacity and sorbent regeneration. *Environmental Science and Pollution Research* **2020,** *27*, 27515-27540.

11. Poullikkas, A., Review of Design, Operating, and financial considerations in flue gas desulfurization systems. *Energy Technology & Policy* **2015,** *2* (1), 92-103.

12. Crevecoeur, S.; Smith, K., Evaluation of Wet FGD Technologies to meet requirements for post CO_2 removal of Flue Gas streams.

13. Schultes, M., Absorption of sulphur dioxide with sodium hydroxide solution in packed columns. *Chemical Engineering & Technology: Industrial Chemistry‐Plant Equipment‐Process Engineering‐Biotechnology* **1998,** *21* (2), 201-209.

14. Zhang, L.; Wu, S.; Gao, Y.; Sun, B.; Luo, Y.; Zou, H.; Chu, G.; Chen, J., Absorption of SO2 with calcium-based solution in a rotating packed bed. *Separation and Purification Technology* **2019,** *214*, 148-155.

15. Mehrara, H.; Shishesaz, M.; Rouzbehani, B., A novel selective flue gas SO_2 removal with an amine absorbent. *International Journal of Science Emerging Tech* **2013,** *6*, 216-221.

16. Duan, L.; Cui, J.; Jiang, Y.; Zhao, C.; Anthony, E. J., Partitioning behavior of Arsenic in circulating fluidized bed boilers co-firing petroleum coke and coal. *Fuel Processing Technology* **2017,** *166*, 107-114.

17. Gleason, G. H. M., N. J.; Loonam, A. C., Recovery of sulphur dioxide. *U. S. Patent* **1940**.

18. Li, D.; Kang, Y., Significantly promoted SO_2 uptake by the mixture of N-methylated ethylene imine polymer and 1-ethyl-3-methylimidazolium tetrazolate. *Journal of Hazardous Materials* **2021,** *404*, 124101.

19. Hao, B.; Zhao, W.; Feng, D.; Xu, S.; Chen, Y., Synthesis of dibutyl-trimethylsilanylmethyl-amine and its application towards SO_2 absorption with phase change behaviors. *New Journal of Chemistry* **2020,** *44* (48), 21228-21237.

20. Furmaniak, S.; Terzyk, A. P.; Gauden, P. A.; Kowalczyk, P.; Szymański, G. S., Influence of activated carbon surface oxygen functionalities on SO_2 physisorption–Simulation and experiment. *Chemical Physics Letters* **2013,** *578*, 85-91.

21. Bagreev, A.; Bashkova, S.; Bandosz, T. J., Adsorption of SO_2 on activated carbons: The effect of nitrogen functionality and pore sizes. *Langmuir* **2002,** *18* (4), 1257-1264.

22. Sun, F.; Gao, J.; Zhu, Y.; Chen, G.; Wu, S.; Qin, Y., Adsorption of SO_2 by typical carbonaceous material: a comparative study of carbon nanotubes and activated carbons. *Adsorption* **2013,** *19*, 959-966.

23. Long, Y.; Zhang, C.; Wang, X.; Gao, J.; Wang, W.; Liu, Y., Oxidation of SO_2 to SO_3 catalyzed by graphene oxide foams. *Journal of Materials Chemistry* **2011,** *21* (36), 13934-13941.

24. Babu, D. J.; Puthusseri, D.; Kühl, F. G.; Okeil, S.; Bruns, M.; Hampe, M.; Schneider, J. J., SO_2 gas adsorption on carbon nanomaterials: a comparative study. *Beilstein journal of nanotechnology* **2018,** *9* (1), 1782-1792.

25. Gao, Y.; Yue, Q.; Gao, B.; Li, A., Insight into activated carbon from different kinds of chemical activating agents: A review. *Science of the Total Environment* **2020,** *746*, 141094.

26. Rosas, J. M.; Ruiz-Rosas, R.; Rodríguez-Mirasol, J.; Cordero, T., Kinetic study of SO_2 removal over lignin-based activated carbon. *Chemical Engineering Journal* **2017,** *307*, 707-721.

27. Guo, Y.; Li, Y.; Zhu, T.; Ye, M., Investigation of SO_2 and NO adsorption species on activated carbon and the mechanism of NO promotion effect on SO_2. *Fuel* **2015,** *143*, 536-542.

28. Li, B.; Ma, C., Study on the mechanism of SO_2 removal by activated carbon. *Energy Procedia* **2018,** *153*, 471-477.

29. Guo, Y.; Li, Y.; Zhu, T.; Ye, M., Effects of concentration and adsorption product on the adsorption of SO_2 and NO on activated carbon. *Energy & fuels* **2013,** *27* (1), 360-366.

30. Boutillara, Y.; Tombeur, J. L.; De Weireld, G.; Lodewyckx, P., In-situ copper impregnation by chemical activation with CuCl2 and its application to SO_2 and H_2S capture by activated carbons. *Chemical Engineering Journal* **2019,** *372*, 631-637.

31. Abdulrasheed, A.; Jalil, A.; Triwahyono, S.; Zaini, M.; Gambo, Y.; Ibrahim, M., Surface modification of activated carbon for adsorption of SO_2 and NO_X: A review of existing and emerging technologies. *Renewable and Sustainable Energy Reviews* **2018,** *94*, 1067-1085.

32. Zhang, S.; Li, Z.; Yang, Y.; Jian, W.; Ma, D.; Jia, F., Kinetics and thermodynamics of SO_2 adsorption on metal-loaded multiwalled carbon nanotubes. *Open Physics* **2020,** *18* (1), 1201-1214.

33. Zhang, Z.; Ibrahim, M. H.; El-Naas, M. H.; Cai, J., Zeolites nanocomposite membrane applications in CO_2 capture. In *Handbook of Nanomaterials for Industrial Applications*, Elsevier: 2018; pp 916-921.

34. Liang, J.; Shan, G.; Sun, Y., Catalytic fast pyrolysis of lignocellulosic biomass: Critical role of zeolite catalysts. *Renewable and Sustainable Energy Reviews* **2021,** *139*, 110707.

35. Li, Y.; Yu, J., Emerging applications of zeolites in catalysis, separation and host–guest assembly. *Nature Reviews Materials* **2021,** *6* (12), 1156-1174.

36. Nazir, L. S. M.; Yeong, Y. F.; Chew, T. L., Methods and synthesis parameters affecting the formation of FAU type zeolite membrane and its separation performance: a review. *Journal of Asian Ceramic Societies* **2020,** *8* (3), 553-571.

37. Derbe, T.; Temesgen, S.; Bitew, M., A short review on synthesis, characterization, and applications of zeolites. *Advances in Materials Science and Engineering* **2021,** *2021*, 1-17.

38. Al-Harahsheh, M.; Shawabkeh, R.; Batiha, M.; Al-Harahsheh, A.; Al-Zboon, K., Sulfur dioxide removal using natural zeolitic tuff. *Fuel Processing Technology* **2014,** *126*, 249-258.

39. Marcu, I.-C.; Sđndulescu, I., Study of sulfur dioxide adsorption on Y zeolite. *Journal of the Serbian Chemical Society* **2004,** *69* (7), 563-569.

40. Marcewicz-Kuba, A.; Olszewska, D., The Activity of SO_2 Removal from Combustion Gases by the DESONOX Type Catalyst Supported on by the DESONOX Type Catalyst Supported on Montmorillonite and Zeolite. *Polish Journal of Chemistry* **2008,** *82* (1-2), 43-47.

41. Razavi, Z.; Mirghaffari, N.; Alemrajabi, A. A.; Davar, F.; Soleimani, M., Adsorption and photocatalytic removal of SO_2 using natural and synthetic zeolites-supported TiO_2 in a solar parabolic trough collector. *Journal of Cleaner Production* **2021,** *310*, 127376.

42. Amini, N.; Soleimani, M.; Mirghaffari, N., Photocatalytic removal of SO_2 using natural zeolite modified by TiO_2 and polyoxypropylene surfactant. *Environmental Science and Pollution Research* **2019,** *26*, 16877-16886.

43. Yaghi, O. M.; Li, G.; Li, H., Selective binding and removal of guests in a microporous metal–organic framework. *Nature* **1995,** *378* (6558), 703-706.

44. Cui, Y.; Yue, Y.; Qian, G.; Chen, B., Luminescent functional metal–organic frameworks. *Chemical reviews* **2012,** *112* (2), 1126-1162.

45. Allendorf, M. D.; Houk, R. J.; Andruszkiewicz, L.; Talin, A. A.; Pikarsky, J.; Choudhury, A.; Gall, K. A.; Hesketh, P. J., Stress-induced chemical detection using flexible metal− organic frameworks. *Journal of the American Chemical Society* **2008,** *130* (44), 14404-14405.

46. Horcajada, P.; Chalati, T.; Serre, C.; Gillet, B.; Sebrie, C.; Baati, T.; Eubank, J. F.; Heurtaux, D.; Clayette, P.; Kreuz, C., Porous metal–organic-framework nanoscale carriers as a potential platform for drug delivery and imaging. *Nature materials* **2010,** *9* (2), 172-178.

47. Eddaoudi, M.; Kim, J.; Rosi, N.; Vodak, D.; Wachter, J.; O'Keeffe, M.; Yaghi, O. M., Systematic design of pore size and functionality in isoreticular MOFs and their application in methane storage. *Science* **2002,** *295* (5554), 469-472.

48. Kampouraki, Z.-C.; Giannakoudakis, D. A.; Nair, V.; Hosseini-Bandegharaei, A.; Colmenares, J. C.; Deliyanni, E. A., Metal organic frameworks as desulfurization adsorbents of DBT and 4, 6-DMDBT from fuels. *Molecules* **2019,** *24* (24), 4525.

49. Mandal, S.; Natarajan, S.; Mani, P.; Pankajakshan, A., Post‐synthetic modification of metal‐organic frameworks toward applications. *Advanced Functional Materials* **2021,** *31* (4), 2006291.

50. Yin, Z.; Wan, S.; Yang, J.; Kurmoo, M.; Zeng, M.-H., Recent advances in post-synthetic modification of metal–organic frameworks: New types and tandem reactions. *Coordination Chemistry Reviews* **2019,** *378*, 500-512.

51. Yu, Q.; Li, Z.; Cao, Q.; Qu, S.; Jia, Q., Advances in luminescent metal-organic framework sensors based on post-synthetic modification. *TrAC Trends in Analytical Chemistry* **2020,** *129*, 115939.

52. Ma, D.; Li, B.; Shi, Z., Multi-functional sites catalysts based on post-synthetic modification of metal-organic frameworks. *Chinese Chemical Letters* **2018,** *29* (6), 827-830.

53. Li, J.-R.; Kuppler, R. J.; Zhou, H.-C., Selective gas adsorption and separation in metal–organic frameworks. *Chemical Society Reviews* **2009,** *38* (5), 1477-1504.

54. Petit, C., Present and future of MOF research in the field of adsorption and molecular separation. *Current opinion in chemical engineering* **2018,** *20*, 132-142.

55. Wu, D.; Zhang, P.-F.; Yang, G.-P.; Hou, L.; Zhang, W.-Y.; Han, Y.-F.; Liu, P.; Wang, Y.-Y., Supramolecular control of MOF pore properties for the tailored guest adsorption/separation applications. *Coordination Chemistry Reviews* **2021,** *434*, 213709.

56. Millward, A. R.; Yaghi, O. M., Metal− organic frameworks with exceptionally high capacity for storage of carbon dioxide at room temperature. *Journal of the American Chemical Society* **2005,** *127* (51), 17998-17999.

57. Zhao, D.; Yuan, D.; Zhou, H.-C., The current status of hydrogen storage in metal–organic frameworks. *Energy & Environmental Science* **2008,** *1* (2), 222-235.

58. Sahoo, R.; Das, M. C., C2s/C1 hydrocarbon separation: The major step towards natural gas purification by metal-organic frameworks (MOFs). *Coordination Chemistry Reviews* **2021,** *442*, 213998.

59. Yang, H.; Xue, L.; Yang, X.; Xu, H.; Gao, J., Advances in Metal-Organic Frameworks for Efficient Separation and Purification of Natural Gas. *Chinese Journal of Structural Chemistry* **2023**, 100034.

60. Li, Z.; Zhang, Y.; Liu, B.; Chen, G.; Smit, B., Multilevel screening of computation‐ready, experimental metal‐organic frameworks for natural gas purification. *AIChE Journal* **2021,** *67* (7), e17279.

61. Bao, Z.; Yu, L.; Ren, Q.; Lu, X.; Deng, S., Adsorption of CO_2 and CH_4 on a magnesium-based metal organic framework. *Journal of colloid and interface science* **2011,** *353* (2), 549-556.

62. Si, X.; Jiao, C.; Li, F.; Zhang, J.; Wang, S.; Liu, S.; Li, Z.; Sun, L.; Xu, F.; Gabelica, Z., High and selective CO_2 uptake, H_2 storage and methanol sensing on the amine-decorated 12-connected MOF CAU-1. *Energy & Environmental Science* **2011,** *4* (11), 4522-4527.

63. Cui, P.; Ma, Y.-G.; Li, H.-H.; Zhao, B.; Li, J.-R.; Cheng, P.; Balbuena, P. B.; Zhou, H.-C., Multipoint interactions enhanced CO_2 uptake: a zeolite-like zinc–tetrazole framework with 24-nuclear zinc cages. *Journal of the American Chemical Society* **2012,** *134* (46), 18892-18895.

64. An, J.; Geib, S. J.; Rosi, N. L., High and selective CO_2 uptake in a cobalt adeninate metal− organic framework exhibiting pyrimidine-and amino-decorated pores. *Journal of the American Chemical Society* **2010,** *132* (1), 38-39.

65. McDonald, T. M.; D'Alessandro, D. M.; Krishna, R.; Long, J. R., Enhanced carbon dioxide capture upon incorporation of N, N′ -dimethylethylenediamine in the metal‐organic framework CuBTTri. *Chemical Science* **2011,** *2* (10), 2022-2028.

66. Peng, Y.; Krungleviciute, V.; Eryazici, I.; Hupp, J. T.; Farha, O. K.; Yildirim, T., Methane storage in metal–organic frameworks: current records, surprise findings, and challenges. *Journal of the American Chemical Society* **2013,** *135* (32), 11887-11894.

67. Wang, X.-S.; Ma, S.; Rauch, K.; Simmons, J. M.; Yuan, D.; Wang, X.; Yildirim, T.; Cole, W. C.; López, J. J.; Meijere, A. d., Metal− organic frameworks based on double-bond-coupled di-isophthalate linkers with high hydrogen and methane uptakes. *Chemistry of Materials* **2008,** *20* (9), 3145-3152.

68. Mason, J. A.; Veenstra, M.; Long, J. R., Evaluating metal–organic frameworks for natural gas storage. *Chemical Science* **2014,** *5* (1), 32-51.

69. He, Y.; Zhou, W.; Yildirim, T.; Chen, B., A series of metal–organic frameworks with high methane uptake and an empirical equation for predicting methane storage capacity. *Energy & Environmental Science* **2013,** *6* (9), 2735-2744.

70. Sumida, K.; Her, J.-H.; Dinca, M.; Murray, L. J.; Schloss, J. M.; Pierce, C. J.; Thompson, B. A.; FitzGerald, S. A.; Brown, C. M.; Long, J. R., Neutron Scattering and Spectroscopic Studies of Hydrogen Adsorption in Cr_3 $(BTC)_2$ A Metal− Organic Framework with Exposed Cr^{2+} Sites. *The Journal of Physical Chemistry C* **2011,** *115* (16), 8414-8421.

71. Liu, J.; Culp, J. T.; Natesakhawat, S.; Bockrath, B. C.; Zande, B.; Sankar, S.; Garberoglio, G.; Johnson, J. K., Experimental and theoretical studies of gas adsorption in Cu_3 $(BTC)_2$: an effective activation procedure. *The Journal of Physical Chemistry C* **2007,** *111* (26), 9305-9313.

72. Lin, X.; Telepeni, I.; Blake, A. J.; Dailly, A.; Brown, C. M.; Simmons, J. M.; Zoppi, M.; Walker, G. S.; Thomas, K. M.; Mays, T. J., High capacity hydrogen adsorption in Cu (II) tetracarboxylate framework materials: the role of pore size, ligand functionalization, and exposed metal sites. *Journal of the American Chemical Society* **2009,** *131* (6), 2159-2171.

73. Wang, X. S.; Ma, S.; Forster, P. M.; Yuan, D.; Eckert, J.; López, J. J.; Murphy, B. J.; Parise, J. B.; Zhou, H. C., Enhancing H2 Uptake by “Close‐Packing” Alignment of Open Copper Sites in Metal–Organic Frameworks. *Angewandte Chemie* **2008,** *120* (38), 7373-7376.

74. Cadiau, A.; Lee, J. S.; Damasceno Borges, D.; Fabry, P.; Devic, T.; Wharmby, M. T.; Martineau, C.; Foucher, D.; Taulelle, F.; Jun, C. H., Design of hydrophilic metal organic framework water adsorbents for heat reallocation. *Advanced Materials* **2015,** *27* (32), 4775-4780.

75. Abtab, S. M. T.; Alezi, D.; Bhatt, P. M.; Shkurenko, A.; Belmabkhout, Y.; Aggarwal, H.; Weseliński, Ł. J.; Alsadun, N.; Samin, U.; Hedhili, M. N., Reticular chemistry in action: A hydrolytically stable MOF capturing twice its weight in adsorbed water. *Chem* **2018,** *4* (1), 94-105.

76. Furukawa, H.; Gandara, F.; Zhang, Y.-B.; Jiang, J.; Queen, W. L.; Hudson, M. R.; Yaghi, O. M., Water adsorption in porous metal–organic frameworks and related materials. *Journal of the American Chemical Society* **2014,** *136* (11), 4369-4381.

77. Fathieh, F.; Kalmutzki, M. J.; Kapustin, E. A.; Waller, P. J.; Yang, J.; Yaghi, O. M., Practical water production from desert air. *Science advances* **2018,** *4* (6), eaat3198.

78. Jasuja, H.; Peterson, G. W.; Decoste, J. B.; Browe, M. A.; Walton, K. S., Evaluation of MOFs for air purification and air quality control applications: Ammonia removal from air. *Chemical Engineering Science* **2015,** *124*, 118-124.

79. Petit, C.; Huang, L.; Jagiello, J.; Kenvin, J.; Gubbins, K. E.; Bandosz, T. J., Toward understanding reactive adsorption of ammonia on Cu-MOF/graphite oxide nanocomposites. *Langmuir* **2011,** *27* (21), 13043-13051.

80. Rieth, A. J.; Tulchinsky, Y.; Dinca, M., High and reversible ammonia uptake in mesoporous azolate metal–organic frameworks with open Mn, Co, and Ni sites. *Journal of the American Chemical Society* **2016,** *138* (30), 9401-9404.

81. Bloch, E. D.; Hudson, M. R.; Mason, J. A.; Chavan, S.; Crocellà, V.; Howe, J. D.; Lee, K.; Dzubak, A. L.; Queen, W. L.; Zadrozny, J. M., Reversible CO binding enables tunable CO/H_2 and CO/N_2 separations in metal–organic frameworks with exposed divalent metal cations. *Journal of the American Chemical Society* **2014,** *136* (30), 10752-10761.

82. Sato, H.; Kosaka, W.; Matsuda, R.; Hori, A.; Hijikata, Y.; Belosludov, R. V.; Sakaki, S.; Takata, M.; Kitagawa, S., Self-accelerating CO sorption in a soft nanoporous crystal. *Science* **2014,** *343* (6167), 167-170.

83. Chen, D.-L.; Wang, N.; Xu, C.; Tu, G.; Zhu, W.; Krishna, R., A combined theoretical and experimental analysis on transient breakthroughs of C_2H_6/C_2H_4 in fixed beds packed with ZIF-7. *Microporous and Mesoporous Materials* **2015,** *208*, 55-65.

84. Lysova, A. A.; Samsonenko, D. G.; Kovalenko, K. A.; Nizovtsev, A. S.; Dybtsev, D. N.; Fedin, V. P., A series of mesoporous metal‐organic frameworks with tunable windows sizes and exceptionally high ethane over ethylene adsorption selectivity. *Angewandte Chemie International Edition* **2020,** *59* (46), 20561-20567.

85. Liao, P.-Q.; Zhang, W.-X.; Zhang, J.-P.; Chen, X.-M., Efficient purification of ethene by an ethane-trapping metal-organic framework. *Nature communications* **2015,** *6* (1), 8697.

86. Kang, M.; Kang, D. W.; Choe, J. H.; Kim, H.; Kim, D. W.; Park, H.; Hong, C. S., A robust hydrogen-bonded metal–organic framework with enhanced ethane uptake and selectivity. *Chemistry of Materials* **2021,** *33* (15), 6193-6199.

87. Liu, J.-X.; Li, J.; Tao, W.-Q.; Li, Z., 3. Al-Based Metal-Organic Framework MFM-300 and MIL-160 for SO2 Capture: A Molecular Simulation Study. *Fluid Phase Equilibria* **2021,** *536*, 112963.

88. Chen, F.; Lai, D.; Guo, L.; Wang, J.; Zhang, P.; Wu, K.; Zhang, Z.; Yang, Q.; Yang, Y.; Chen, B., Deep desulfurization with record SO_2 adsorption on the metal–organic frameworks. *Journal of the American Chemical Society* **2021,** *143* (24), 9040-9047.

CHAPTER 2. EXPERIMENTAL MATERIALS AND METHODS

2.1 Materials

All the MOF materials discussed in this dissertation were synthesized using solvothermal methods according to previous articles or with some modifications where necessary. In general, the MOFs discussed can be classified into three highly porous structures that are well-known: MIL-100, MIL-101, and UiO-66. As for the ionic liquids (ILs), there are two types: Diethylenetriamine (DETA) -based ILs and Tris(2-aminoethyl)amine (TETA) -based ILs. For brevity, the detailed synthesis methods are not presented in this chapter, but at the beginning of each following respective objective for ease of reference. This chapter only provides the general motivations for the materials chosen.

2.1.1 Material sources

The raw materials required for synthesizing MOFs and ILs were purchased from Sigma Aldrich and Fisher Scientific and treated without any further purification.

2.1.2 MOFs

2.1.2.1 MIL-100

MIL-100 refers to a specific category of mesoporous MOFs that are composed of trimeric metal (III) octahedra, connected via trimesate ligands (BTC: 1,3,5-benzene tricarboxylic acid) and sharing a common oxygen atom, as depicted in Figure 2-1. These MOFs exhibit a cubic zeo-type structure and contain two distinct types of meso-cages (2.5 and 2.9 nm) that can be accessed

through microporous windows of approximately 0.47 × 0.55 nm and 0.86 nm in size, respectively, as reported in [1].

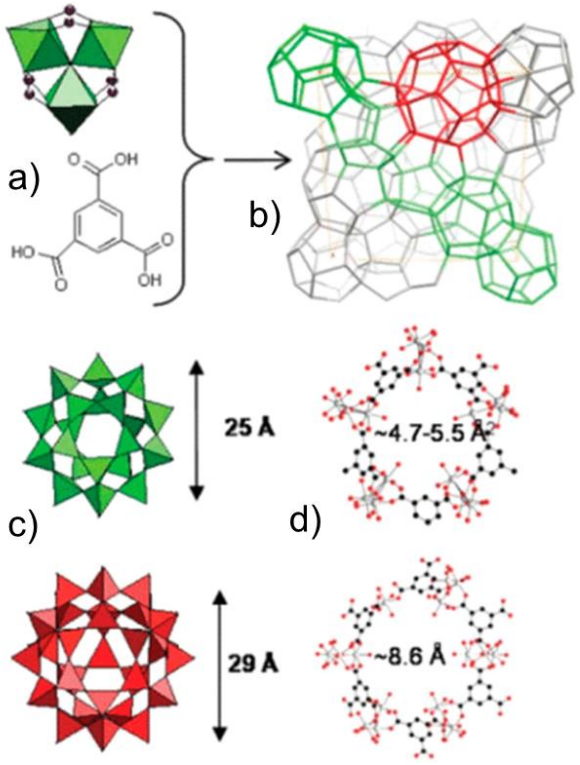

Figure 2-1: Structure of MIL-100. (a) The trimer of metal octahedra and the trimesic acid. (b) One unit cell of MIL-100. (c) The free apertures of the two types of cages. (d) Pentagonal and hexagonal windows of the mesoporous cages. Image reproduced from Zhong and Zhang[2]

MIL-100 has been extensively studied for its potential applications in various fields, including hydrogen storage[3], water purification[4], and catalysis[5]. One of the most intriguing aspects of MIL-100 is its high tunability and designability. A wide range of trivalent metals can be used for the synthesis of MIL-100, and these metal sites on the metal trimers can be released through a sample activation process, resulting in MOFs with diverse properties. For instance, a series of MIL-100(M) (M = Al, Cr, Fe, In, Sc, and V) has been investigated in the context of the synthesis reaction of nopoh, and it was found that the catalytic activities of MIL-100(M) correlated linearly

with the concentrations of accessible Lewis acid sites (i.e., the metal sites) and increased in the following order: MIL-100(In) < MIL-100(Cr) < MIL-100(Al) < MIL-100(Fe) << MIL-100(Sc) < MIL-100(V).[6] Similarly, the role of metal sites in MIL-100 has been explored for the removal of N/S-heterocyclic contaminants from fuels, and it was found that MIL-100(V) is the most effective adsorbent for the deep and selective removal of nitrogen contaminants from fuel feeds.[7] Due to the high degree of tunability afforded by the metal centers in MIL-100, it was selected as the platform for studying the relationship between the nature of trivalent metals on MOFs with SO_2 in Chapter 3. In addition, the metal insertion process for the function of trivalent metals on MIL-100 MOFs has also been evaluated due to its potential to overcome water stability issues of MIL-100.

2.1.2.2 MIL-101(Cr)

MIL-101(Cr) is one of the most representative materials of the MIL series MOFs that are constructed of chromium and terephthalic acid (BDC) ligands. With a structure similar to that of MIL-100, MIL-101(Cr) also exhibit a zeolite-like structure featuring two types of meso-cages with internal diameters of 2.7 nm and 3.4 nm associated with pentagonal and hexagonal windows of 1.17 nm and 1.6 nm, as illustrated in Figure 2-2.[8]

The exceptionally high specific surface area, large pore volume, and impressively strong thermal, chemical, and water stability make MIL-101 attractive in multiple applications, such as gas adsorption and separation[9-10], sensing[11], and drug transport[12]. Additionally, the presence of unsaturated Lewis acid sites (i.e., OMSs: uncoordinated chromium sites) in their structure would be beneficial for post functionalization extending their utilization. For example, Lee and co-workers reported the synthesis of MIL-101(Cr) and its derivatives (Post-modified with ethylenediamine (ED), diethylenetriamine (DETA), and N-(phosphonomethyl)iminodiacetic acid

(PMIDA)), and explored their effectiveness in the separation and recovery of rare earth elements.[13] It showed that MIL-101-PMIDA behaved with superior adsorption capacities because of the surface complexation (COO^-, PO_3^{2-}, and free NH_2) and the electrostatic attraction between -NH_2OH^- and rare earth elements. In Chapter 4, MIL-101 was chosen as a host material for the post-functionalization of DETA, TETA, and their corresponding ILs, and their adsorptive performances for SO_2 were examined. Particularly, the impact of neutral and positive charged nitrogen sites on SO_2 selective adsorption was inspected.

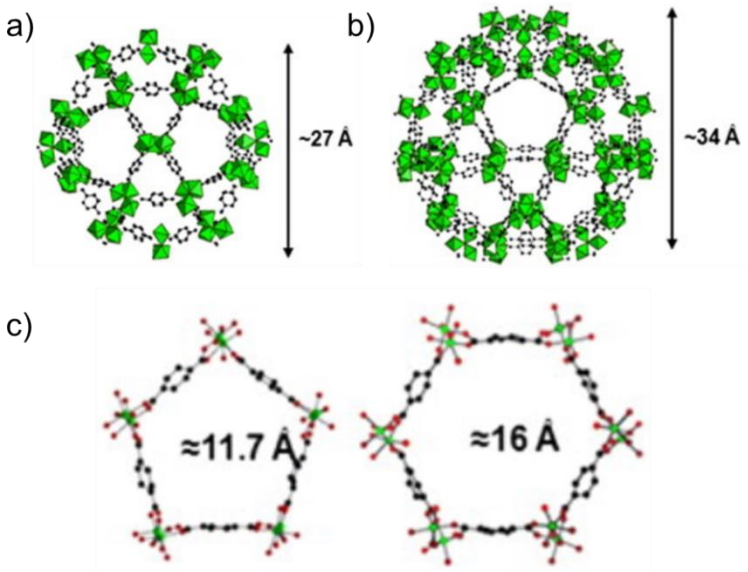

Figure 2-2: Structure of MIL-101. (a) The small cage. (b) The large cage. (c) Pentagonal and hexagonal windows of the mesoporous cages. Image reproduced from Trung and Ferey[8]

2.1.2.3 UiO-66

UiO-66 is a type of metal-organic framework (MOF) that was first synthesized in 2008 by researchers at the University of Oslo (UiO)[14]. It is composed of zirconium oxide clusters ($Zr_6(OH)_4O_4$) connected by terephthalic acid (BDC) linkers, which form a three-dimensional porous structure. The pores of UiO-66 are made up of interconnected approximately 1.1 nm

octahedral cages and 0.8 nm tetrahedral cages, which are connected through 0.6 nm triangular windows, as shown in Figure 2-3. It always shows remarkable stability in harsh conditions due to the strong Zr-O bonds and the ability of the inner Zr_6-cluster to undergo reversible rearrangement upon the removal or addition of μ3-OH groups, without any changes in the connecting carboxylates.[14]

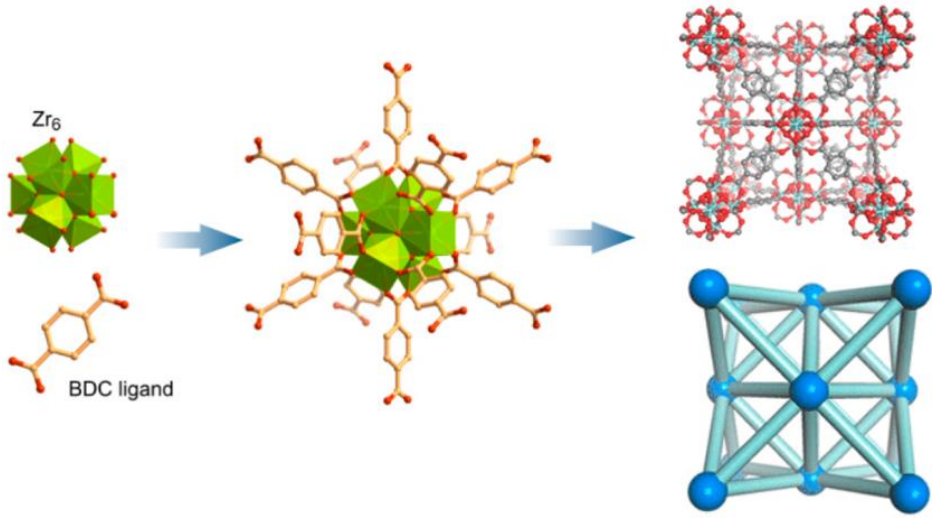

Figure 2-3: Structural details of UiO-66. Image reproduced from Rui and Feng[15-16]

UiO-66 is a highly studied metal-organic framework that has garnered significant attention due to its unique structural properties and potential applications in various fields[17-19]. Notably, UiO-66 has a significant advantage in its ability to undergo ligand functionalization, allowing for the introduction of various functional groups by modifying the ligands used in its synthesis. Back in 2012, the Walton research group at Georgia Institute of Technology synthesized several UiO-66 variations with BDC ligands functionalized with amino, nitro, methoxy, and naphthyl groups, and investigated the effects of the functional groups on the adsorption properties of UiO-66 for CO_2, CH_4, N_2, and water vapor.[20] The introduced function groups can alter the polar, basic, and hydrophobic characteristics of UiO-66, resulting in different adsorption behaviours. The study in

Chapter 5 was inspired by this work. In Chapter 5, a series of UiO-66 with different ligands containing distinct nitrogen sites were synthesized, and the effects of the nitrogen sites on SO_2 adsorption have been examined.

2.2 Experimental methods

Two primary techniques are employed in this work. The first is for material characterization, which includes techniques such as powder X-ray diffraction, N_2 adsorption measurements, and thermogravimetric analysis. The second main type of method involves testing and analyzing the adsorption performance of the materials, including gas adsorption isotherm, breakthrough measurements, infrared spectroscopy, and more.

2.2.1 Powder X-ray diffraction (PXRD)

Powder X-ray diffraction (PXRD) is a non-destructive analytical technique used to determine the crystal structure of a wide range of materials. The mechanism of PXRD involves the interaction of X-rays with the crystal lattice of a material. When a beam of X-rays is directed onto a crystal, the X-rays interact with the electrons in the atoms within the crystal. This interaction causes the X-rays to scatter in different directions, creating a diffraction pattern that is unique to the crystal structure of the material. The diffraction pattern produced by PXRD is a series of peaks that correspond to the different crystal planes within the material. The intensity of each peak is related to the number of atoms in the crystal plane and the angle of diffraction. By analysing the diffraction pattern, it is able to determine the crystal structure of the material, including the unit cell dimensions, the arrangement of atoms within the crystal, and the symmetry of the crystal lattice.

In this work, PXRD can help identify the specific MOF materials, and confirm the crystallinity of MOF samples.

2.2.2 N_2 adsorption measurement

N_2 adsorption measurement at -196 °C is a commonly used method to determine the surface area and porosity of porous materials. The technique is based on the principle that gas molecules will adsorb onto the surface of the material, filling the pores and increasing the pressure of the gas in the surrounding environment. The adsorption process results in the formation of a multilayer of gas molecules on the surface of the solid, which is used to calculate the BET surface area. The BET (Brunauer-Emmett-Teller) theory is a mathematical model that describes the physical adsorption of gas molecules onto the surface of a solid material. The BET equation is

$$\frac{p}{v(p_0-p)} = \frac{c-1}{v_m c}\frac{p}{p_0} + \frac{1}{v_m c} \qquad \text{Equation 2.1}$$

where p and p_0 are the equilibrium and the saturation pressure of adsorbates at the temperature of adsorption, respectively; v is the adsorbed gas quantity (for example, in volume units) while v_m is the monolayer adsorbed gas quantity, c is the BET constant.

In practice, a line of $\frac{p}{v(-p)}$ verse $\frac{p}{p_0}$ for experimental data over $0.05 \leq \frac{p}{p_0} \leq 0.3$ is first plotted. The slope refers to $\frac{c-1}{v_m c}$, and the y-intercept is $\frac{1}{v_m c}$. The BET surface area is calculated through the below equation

$$S_{BET} = \frac{v_m N_{av} s}{v m_{sample}} \qquad \text{Equation 2.2}$$

where N_{av} is the Avogadro number, s is the adsorption cross-section of the adsorbate, and m_{sample} is the mass of the solid sample.

In this study, N_2 adsorption measurement and BET calculation can assist in verifying the high porosity feature of MOF samples.

2.2.3 Thermogravimetric analysis (TGA)

Thermogravimetric analysis (TGA) is a thermal analysis technique used to study the changes in the mass of a material as a function of temperature or time in a controlled environment. It is a powerful tool for studying the thermal properties of materials. TGA is widely used in various fields, including materials science, chemistry, polymers, pharmaceuticals, and food science. It is often used in conjunction with other thermal analysis techniques, such as differential scanning calorimetry (DSC) or evolved gas analysis (EGA), to obtain more comprehensive information about the thermal behaviour of materials.

In TGA, a small sample of the material is heated at a constant rate in a furnace while its weight is continuously monitored. The sample can be heated under different conditions, such as in an inert atmosphere (e.g., nitrogen) or in an oxidative atmosphere (e.g., air). The temperature and heating rate can also be varied according to the needs of the experiment. As the sample is heated, it undergoes physical and chemical changes, which can be detected by measuring the changes in its weight. These changes may include the loss of moisture, decomposition, oxidation, or reduction reactions, phase transitions, and others. By analysing the TGA curve, it is possible to determine the thermal properties of the material, such as the thermal stability, the onset and peak temperatures of decomposition, the amount of mass loss, and the reaction kinetics.

This work employs TGA to ascertain the loading amounts of DETA, TETA, and their corresponding ILs in MOFs, and to examine the thermal stability of the introduced compounds.

2.2.4 Volumetric adsorption system

A volumetric adsorption system is a type of instrument used for measuring gas adsorption isotherms of porous materials. The system operates by exposing the material to a known pressure of a gas at a constant temperature and measuring the amount of gas adsorbed by the material. Figure 2-4 illustrates the home-built pressure decay volumetric adsorption system used in this work. The basic components of a volumetric adsorption system include high-pressure gas sources, a sample cell containing the porous material, pressure transducers, and a gas flow control system. The gas source provides the gas to be adsorbed which is typically a pure gas. The sample cell is designed to hold the porous material and allow the gas to flow through it. The pressure transducer measures the pressure of the gas in the sample cell, which is used to calculate the amount of gas adsorbed. The gas flow control system regulates the flow rate of gas into the sample cell and maintains constant pressure and temperature. Typically, the measurement involves exposing the sample to a series of increasing pressures of gas and recording the corresponding amount of gas adsorbed at each pressure. The resulting data can be used to construct gas adsorption isotherms, which describe the relationship between the amount of gas adsorbed and its pressure at a constant temperature.

This study utilizes the home-built volumetric adsorption equipment to gather SO_2 isotherm data for MOF samples. Additionally, the isotherms for other gases, including CO_2, N_2, and water vapor, are measured using a Micromeritics 3Flex instrument.

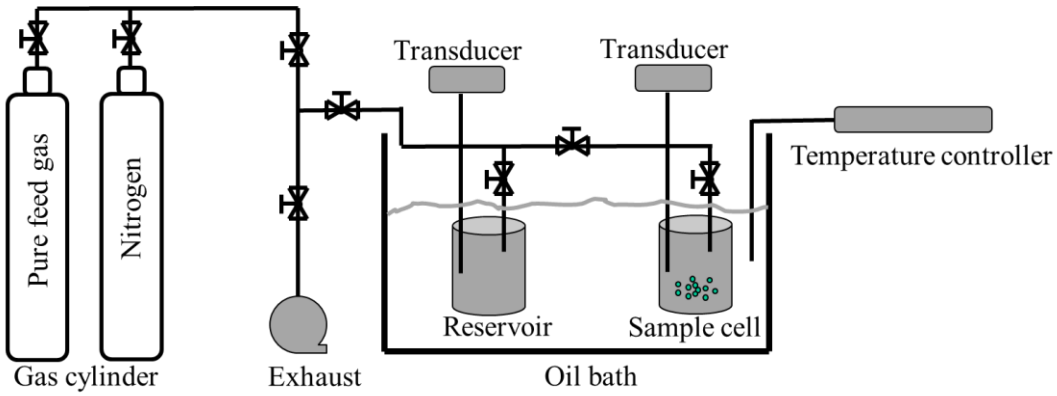

Figure 2-4: Illustration of the home-built volumetric adsorption system.

2.2.5 Breakthrough system

In contrast to the volumetric adsorption system, breakthrough systems allow the collection of dynamic adsorption data that can be used to evaluate the performance of the material in removing a specific contaminant from a gas stream over time. As illustrated in Figure 2-5, the measurement process typically involves passing the contaminated gas or vapor through the adsorbent material for a specified period and monitoring the concentration of the contaminant in the gas stream both before and after it passes through the adsorbent material. The breakthrough point is reached when the concentration of the contaminant in the gas stream exiting the test chamber exceeds a predetermined threshold, indicating that the adsorbent material has become saturated and can no longer remove the additional contaminant.

In this work, a gas mixture of 1000 ppm SO_2/balanced N_2 is introduced into the breakthrough system with a flow rate of 20 mL/min. The mixture passes through the adsorption column, and the concentrations of different species are tested by an IR spectrometer.

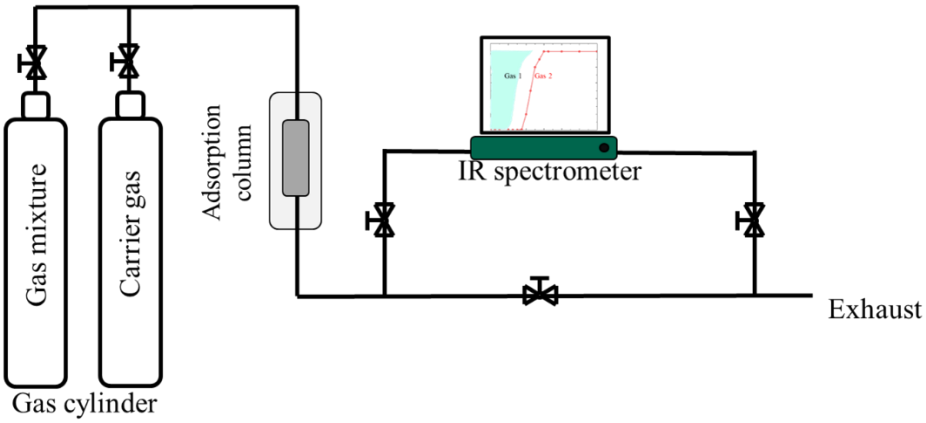

Figure 2-5: Illustration of the home-built breakthrough system.

2.2.6 Infrared spectroscopy (IR)

Infrared spectroscopy (IR) is a powerful analytical technique used to identify and characterize organic and inorganic compounds based on their absorption or transmission of infrared radiation. IR radiation falls in the range of the electromagnetic spectrum between visible light and microwave radiation, with wavelengths ranging from 0.78 to 1000 micrometres. In IR spectroscopy, a sample is exposed to infrared radiation, and the resulting spectrum is analysed to determine the unique vibration frequencies of the sample's molecular bonds. These frequencies can be used to identify functional groups, determine the degree of unsaturation, and provide information about the molecular structure and composition of the sample.

In this study, IR is employed to determine the presence of different functional groups including ILs and various nitrogen sites, and to characterize the interaction between these functional groups with adsorbed SO_2 molecules.

2.3 References

1. Cabello, C. P.; Rumori, P.; Palomino, G. T., Carbon dioxide adsorption on MIL-100 (M)(M= Cr, V, Sc) metal–organic frameworks: IR spectroscopic and thermodynamic studies. *Microporous and Mesoporous Materials* **2014,** *190*, 234-239.

2. Zhong, G.; Liu, D.; Zhang, J., Applications of porous metal–organic framework MIL-100 (M)(M= Cr, Fe, Sc, Al, V). *Crystal Growth & Design* **2018,** *18* (12), 7730-7744.

3. Latroche, M.; Surblé, S.; Serre, C.; Mellot‐Draznieks, C.; Llewellyn, P. L.; Lee, J. H.; Chang, J. S.; Jhung, S. H.; Férey, G., Hydrogen storage in the giant‐pore metal‐organic frameworks MIL‐100 and MIL‐101. *Angewandte Chemie* **2006,** *118* (48), 8407-8411.

4. Jun, J. W.; Tong, M.; Jung, B. K.; Hasan, Z.; Zhong, C.; Jhung, S. H., Effect of central metal ions of analogous metal–organic frameworks on adsorption of organoarsenic compounds from water: plausible mechanism of adsorption and water purification. *Chemistry–A European Journal* **2015,** *21* (1), 347-354.

5. Horcajada, P.; Surblé, S.; Serre, C.; Hong, D.-Y.; Seo, Y.-K.; Chang, J.-S.; Grenèche, J.-M.; Margiolaki, I.; Férey, G., Synthesis and catalytic properties of MIL-100 (Fe), an iron (III) carboxylate with large pores. *Chemical Communications* **2007,** (27), 2820-2822.

6. Gómez‐Pozuelo, G.; Cabello, C. P.; Opanasenko, M.; Horáček, M.; Čejka, J., Superior Activity of Isomorphously Substituted MOFs with MIL‐100 (M= Al, Cr, Fe, In, Sc, V) Structure in the Prins Reaction: Impact of Metal Type. *ChemPlusChem* **2017,** *82* (1), 152-159.

7. Van de Voorde, B.; Boulhout, M.; Vermoortele, F.; Horcajada, P.; Cunha, D.; Lee, J. S.; Chang, J.-S.; Gibson, E.; Daturi, M.; Lavalley, J.-C., N/S-heterocyclic contaminant removal from fuels by the mesoporous metal–organic framework MIL-100: The role of the metal ion. *Journal of the American Chemical Society* **2013,** *135* (26), 9849-9856.

8. Trung, T. K.; Ramsahye, N. A.; Trens, P.; Tanchoux, N.; Serre, C.; Fajula, F.; Férey, G., Adsorption of C5–C9 hydrocarbons in microporous MOFs MIL-100 (Cr) and MIL-101 (Cr): A manometric study. *Microporous and Mesoporous Materials* **2010,** *134* (1-3), 134-140.

9. Song, C.; Li, R.; Fan, Z.; Liu, Q.; Zhang, B.; Kitamura, Y., CO_2/N_2 separation performance of Pebax/MIL-101 and Pebax/NH2-MIL-101 mixed matrix membranes and intensification via sub-ambient operation. *Separation and Purification Technology* **2020,** *238*, 116500.

10. Bhattacharjee, S.; Chen, C.; Ahn, W.-S., Chromium terephthalate metal–organic framework MIL-101: synthesis, functionalization, and applications for adsorption and catalysis. *Rsc Advances* **2014,** *4* (94), 52500-52525.

11. Iacomi, P.; Gulcay-Ozcan, E.; Pires Conti, P.; Biswas, S.; Steunou, N.; Maurin, G.; Rioland, G.; Devautour-Vinot, S., MIL-101 (Cr) MOF as an effective siloxane sensor. *ACS Applied Materials & Interfaces* **2022,** *14* (15), 17531-17538.

12. Horcajada, P.; Serre, C.; Vallet‐Regí, M.; Sebban, M.; Taulelle, F.; Férey, G., Metal‐organic frameworks as efficient materials for drug delivery. *Angewandte chemie* **2006,** *118* (36), 6120-6124.

13. Lee, Y.-R.; Yu, K.; Ravi, S.; Ahn, W.-S., Selective adsorption of rare earth elements over functionalized Cr-MIL-101. *ACS applied materials & interfaces* **2018,** *10* (28), 23918-23927.

14. Cavka, J. H.; Jakobsen, S.; Olsbye, U.; Guillou, N.; Lamberti, C.; Bordiga, S.; Lillerud, K. P., A new zirconium inorganic building brick forming metal organic frameworks with exceptional stability. *Journal of the American Chemical Society* **2008,** *130* (42), 13850-13851.

15. Faria, R. G.; Julião, D.; Balula, S. S.; Cunha-Silva, L., Hf-Based UiO-66 as Adsorptive Compound and Oxidative Catalyst for Denitrogenation Processes. *Compounds* **2021,** *1* (1), 3-14.

16. Feng, Y.; Chen, Q.; Jiang, M.; Yao, J., Tailoring the properties of UiO-66 through defect engineering: A review. *Industrial & Engineering Chemistry Research* **2019,** *58* (38), 17646-17659.

17. Ahmadijokani, F.; Molavi, H.; Rezakazemi, M.; Tajahmadi, S.; Bahi, A.; Ko, F.; Aminabhavi, T. M.; Li, J.-R.; Arjmand, M., UiO-66 metal–organic frameworks in water treatment: A critical review. *Progress in Materials Science* **2022,** *125*, 100904.

18. Dhakshinamoorthy, A.; Santiago‐Portillo, A.; Asiri, A. M.; Garcia, H., Engineering UiO‐66 metal organic framework for heterogeneous catalysis. *ChemCatChem* **2019,** *11* (3), 899-923.

19. Liu, X., Metal-organic framework UiO-66 membranes. *Frontiers of Chemical Science and Engineering* **2020,** *14*, 216-232.

20. Cmarik, G. E.; Kim, M.; Cohen, S. M.; Walton, K. S., Tuning the adsorption properties of UiO-66 via ligand functionalization. *Langmuir* **2012,** *28* (44), 15606-15613.

CHAPTER 3. INFLUENCE OF TRIVALENT OPEN METAL SITES ON SO_2 ADSORPTION IN MOFS

3.1 Introduction

MOFs possessing coordinatively unsaturated metal sites (referred to as open metal sites, OMSs) exhibit high affinity to specific gas molecules. [1-5] For example, MOF PCN-14 was reported to provide an impressive methane adsorption behavior attributed to its coordinatively unsaturated Cu ions.[3] OMSs are a regular feature of MOF materials. In some MOFs, metal nodes or clusters are not fully coordinated by organic ligands but partially by solvent or water molecules. Removing these molecules under vacuum and high temperature can expose the metal sites that are essential to MOFs' capacity and selectivity for gas adsorption at low partial pressures by acting as Lewis acid centers and binding sites. This attractive feature of MOF materials makes them an excellent candidate for SO_2 removal since, compared to other components in flue gas, the concentration of SO_2 (SO_2's partial pressure) is extremely low requiring high binding energy between adsorbents and SO_2 molecules. Although a few studies have investigated MOFs with divalent OMSs (e.g. Cu-BTC[6], Zn-MOF-74[7], etc.) that generally show irreversible adsorption, few efforts have been devoted to studying MOFs with trivalent OMSs for SO_2 adsorption systematically. A thorough understanding of the interactions between trivalent metals with SO_2 molecules is necessary to further design and synthesis of MOF materials for SO_2 adsorption and separation.

MIL-100 MOFs represent an excellent platform for studying the relationship between the nature of trivalent metals and their SO_2 adsorption. MIL-100s are mesoporous MOFs constructed by trimers of metal octahedra with 1,3,5-benzene tricarboxylic acid (BTC) ligands, and various trivalent metals can be used to assemble into the MIL-100 framework.[8-9] In each trimer, three metal

atoms with octahedral geometry share a common vertex μ_3-O. The four axial coordination positions of each metal atom are linked by μ_2-bridging trimesate ligands to generate hybrid supertetrahedra resulting in two different interconnected mesoporous cages, which are 24 Å and 29 Å in diameter.[10] The three apical terminals of the trimer are occupied by solvent molecules and one anionic charge species in such a way MIL-100 can possess corresponding OMSs easily after removing solvent molecules by an appropriate activation process. In this work, a series of MIL-100-M (M = Al, Sc, V, Fe, and In.) MOFs was successfully prepared with identical crystal structures and comparable porosity. Their adsorption performance and stability for SO_2 capture were investigated. Among these materials, MIL-101-Sc exhibited the most favorable performance, demonstrating the highest uptake of SO_2 at low partial pressures, the greatest IAST selectivity for SO_2 over CO_2, and the strongest stability when exposed to SO_2.

While MOFs with OMSs provide good binding sites for adsorption, they often exhibit weak stability, especially under humid conditions.[11] The degradation is mainly due to the metal clusters or metal ions that construct MOFs lacking the electronic requirements needed to sustain the stability of open metal sites.[12] The highly corrosive and reactive features of flue gas can lead to severe structural degradation of some MIL-100-M materials. To avoid the stability issues of MIL-100-M, a post-synthetic metal insertion process has been applied to a UiO-66-2COOM synthesis by post-synthetically introducing OMSs in MIL-100-M materials into the robust MOF UiO-66-2COOH. Post-synthetic metal insertion process offers a facile and flexible approach to modifying MOFs by incorporating a wide variety of metal species with free functional groups in robust MOFs. That can lead to the robust MOFs featuring OMSs that may have a high affinity towards specific gas molecules while maintaining their stability.[13-18] Figure 3-1 illustrates an example of post-synthetic metal insertion for UiO-66-2COOH. The ligand of UiO-66-2COOH has four

carboxyl groups, two of these groups are utilized in the construction of the framework, while the remaining two are available for additional metal insertion. In this work, UiO-66-2COOM (M = Al, Sc, Fe, Ga, and In.) materials were also synthesized to study the similarity of pristine OMSs in MIL-100-M and post-synthetically introduced OMSs in UiO-66-2COOM for SO_2 adsorption. Furthermore, the stability of UiO-66-2COOM was assessed under relevant conditions. The results obtained revealed that the functionality of OMSs in MIL-100-M can be replicated through the post-metal insertion process in UiO-66-2COOM, providing valuable insights into SO_2 adsorption mechanisms, and UiO-66-2COOM demonstrated good stability to humid SO_2 exposure.

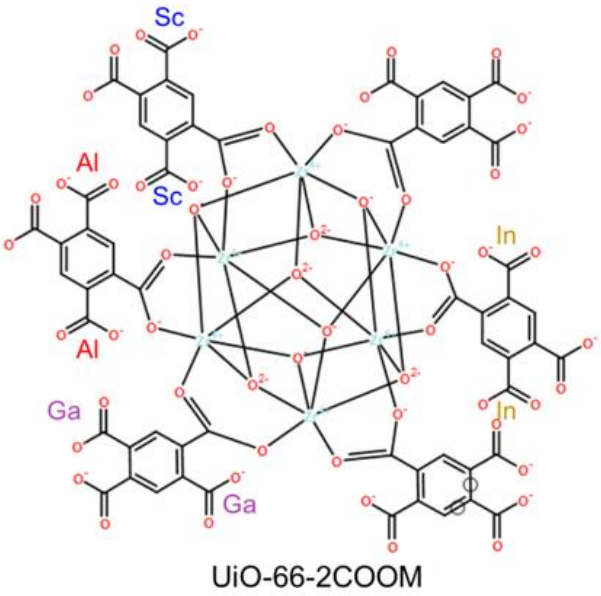

Figure 3-1: Schematic structure of UiO-66-2COOM.

3.2 Experimental section

3.2.1 Materials

MIL-100-Al: The synthesis of MIL-100-Al was based on a method previously reported by Volkringert and Taulelle et al.[19] as follows: 0.61 mmol (0.230 g) of aluminum nitrate nonahydrate

($Al(NO_3)_3 \cdot 9H_2O$) and 0.41 mmol (0.104 g) of trimethyl 1,3,5-benzenetricarboxylate (Me-BTC) were mixed in 0.77 mL of nitric acid (1M HNO_3) and 2.8 mL of water. The mixture was transferred to a 23 mL PTFE-lined autoclave with a stainless-steel casing and placed in an isothermal oven at 210 ℃ for 3.5 h (the temperature went up to 210°C in 1 h). The as-synthesized product was then collected by centrifugation, washed with purified water, and dried at room temperature.

MIL-100-Sc: The MIL-100-Sc materials were prepared following the procedure reported in the literature[20]. A mixture of 2 mmol (0.61 g) of scandium trinitrate ($Sc(NO_3)_3 \cdot xH_2O$) and 1.2 mmol (0.25 g) of 1,3,5-benzenetricarboxylate (BTC) dissolved in 45 mL of DMF was stirred at room temperature for 30 minutes. Subsequently, the mixture was placed in a 100 mL PTFE-lined autoclave and heated at 150 ℃ for 36 h in an isothermal oven. The resulting white product was collected by centrifugation, washed with DMF, thermally treated in ethanol at 100 ℃ for 16 h, and then dried at room temperature.

MIL-100-V: MIL-100-V was synthesized following a published procedure.[8] Briefly, a mixture of 8 mmol (1.25 g) of vanadium chloride (VCl_3) and 4 mmol (1.17 g) of triethyl-1,3,5-benzenetricarboxylate (Et-BTC) in 10 mL of water was placed in a 46 mL PTFE-lined autoclave and heated at 220 ℃ for 72 h. The resulting product was centrifuged, washed with hot ethanol, and dried at room temperature.

MIL-100-Fe: A molar ratio metal : ligand : 65% HNO_3 : H_2O of 1 : 0.67 : 0.6 : 166 was reported being used for the synthesis of MIL-100-Fe[21]. A mixture of 24.1 mmol (3.26 g) of iron chloride hexahydrate ($FeCl_3 \cdot 6H_2O$), 16.15 mmol (1.70 g) of BTC, 0.5 mL HNO_3, and 36 mL water was added in a 46 mL PTFE-lined autoclave and heated at 150 ℃ for 12 h. The light pink solid product was collected by centrifugation and washed with water. To remove unreacted ligands

residing in the frameworks, the as-synthesized MIL-100-Fe was purified by soaking in water at 80 ℃ for 1 h, followed by ethanol at 60 ℃ for 3 h.

MIL-100-In: MIL-100-In was synthesized following a previously reported procedure[8] by a thermal reaction of 0.95 mmol (0.21 g) of indium chloride ($InCl_3$) and 1.05 mmol (0.22 g) of BTC in a solution (40 mL total) of DMF (17.5 mL), ethanol (17.5 mL), and water (5 mL) at 120 ℃ for 24 h. The product was collected by centrifugation and then washed with DMF and ethanol and dried at room temperature.

UiO-66-2COOH: The synthesis of UiO-66-2COOH followed the procedure reported by Joshi and Walton et al..[22] In brief, 0.93 mmol (0.3 g) of zirconyl chloride octahydrate ($ZrOCl_2 \cdot 8H_2O$) and 0.93 mmol (0.234 g) of 1,2,4,5-benzenetetracarboxylic acid, 9 mL of N-N dimethylacetamide (DMA) and 3.6 mL of formic acid were loaded in a 23 mL PTFE-lined autoclave. The mixture was reacted at 150 ℃ for 24 h (heated to 150 ℃ with a ramp rate of 2.2°C/min). The white solid product was washed by DMF, and ethanol several times, then left to dry at room temperature.

UiO-66-2COOM (M = Al, Sc, Fe, Ga, and In.): Dissolved 1 mmol of metal chloride ($AlCl_3$, $ScCl_3 \cdot 6H_2O$, $FeCl_3 \cdot 6H_2O$, $GaCl_3$, or $InCl_3$) in 6 mL of ethanol, then 0.2 g of activated UiO-66-2COOH were added to the solution. The mixture was stirred for 4 h and then left statically for 20 h. The resulting solid was collected by centrifugation and washed with fresh ethanol twice.

3.2.2 Characterization and measurements

PXRD and BET surface areas: PXRD (Powder X-ray diffraction) patterns of the synthesized MIL-100-M and UiO-66-2COOH were collected using an XPert PRO Alpha-1 diffraction system with Cu Kα radiation (λ = 1.542 Å) under ambient conditions with 2θ ranging from 2 to 30°. The data were recorded continuously with a step size of 0.0167° per second. Surface areas were calculated from N_2 physisorption measurements at -196 ℃ and calculated via the Brunauer, Emmett, and Teller (BET) model using a pressure range of $0.005 < P/P_0 < 0.03$.[23] All samples were first activated at 150 ℃ under vacuum for 15 h before adsorption measurements.

SO_2 and CO_2 adsorption isotherms: SO_2 and CO_2 adsorption isotherms were obtained using a home-built pressure decay system and a Micromeritics 3Flex Surface Characterization Analyzer with ultrapure grade SO_2 and CO_2, respectively. Both were carried out with controlled changes of partial pressures in the sample chamber or tube under a constant temperature. SO_2 and CO_2 isotherms were recorded at 25 ℃ and all samples were activated at 150 ℃ for 15 h under vacuum prior to the measurements. Ideal Adsorbed Solution Theory (IAST) calculations were conducted through IAST++ interface.[24]

Humid SO_2 exposure: A stream of 1000 ppm SO_2 in N_2 was used as the acid gas source. Ultra-high purity air was used to generate a humid stream with a humidity bottle supplied by Fuel Cell Technologies Inc. A mixture of acid gas and the humid stream (RH: 60 %) was fed into an exposure unit to maintain a desired acid gas concentration for 24 h under 25 ℃. A diagram of the device can be found in Appendix Figure A-1.

3.3 Results and discussion

3.3.1 Crystallinity and porosity of materials

The crystallinity of the obtained MIL-100-M was checked by powder X-ray diffraction (PXRD), and the results are depicted in Figure 3-2(a). The PXRD patterns of all five MIL-100-M MOFs exhibited distinct peaks associated with MIL-100, demonstrating good agreement with the simulated pattern. This observation confirms the successful synthesis of MIL-100-M materials with high crystallinity and structural consistency. Additionally, the N_2 adsorption isotherms conducted at -196 ℃ displayed typical type I sorption behaviors as displayed in Figure 3-2(b). Estimations based on the BET analysis revealed that the surface areas of all five MIL-100-M MOFs were around 1400 m^2/g, consistent with existing literature.[8] This further confirms the achievement of highly porous MIL-100-M MOFs. These findings collectively highlight the similarity of the structure of these synthesized samples and the primary differentiating factor among the five MIL-100-M MOFs - the distinct metal centers. Consequently, these materials offer exceptional platforms for investigating the interactions between trivalent metals and SO_2 molecules.

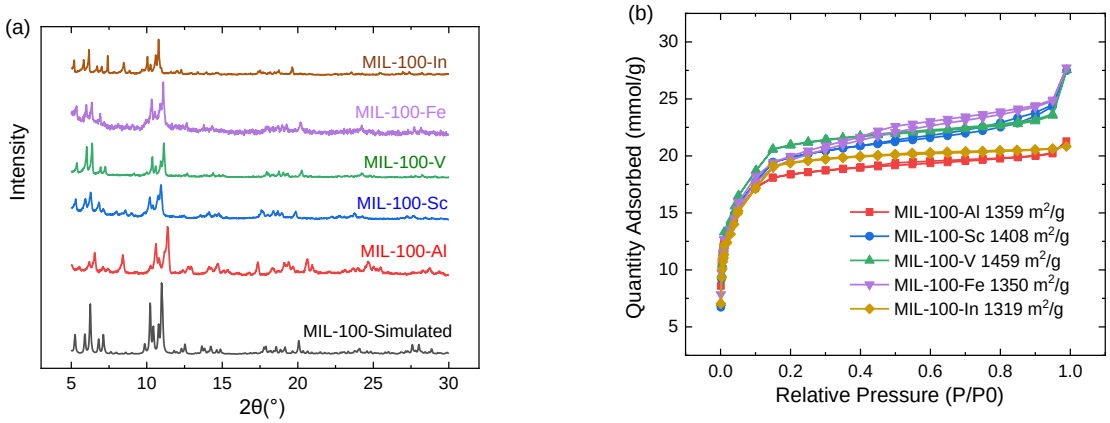

Figure 3-2: (a), PXRD of MIL-100-M; (b), N_2 adsorption isotherms of MIL-100-M.

3.3.2 SO_2 adsorption of MIL-100-M and IAST selectivity

Isothermal SO_2 experiments were conducted on activated MIL-100-M materials to evaluate their adsorption capacities. The results, illustrated in Figure 3-3(a), reveal that all five MIL-100-M MOFs exhibit similar SO_2 loadings of approximately 12 mmol/g at 800 mbar and 25 ℃. Notably, the adsorption patterns displayed a linear relationship between loading and pressure from 100 mbar to 800 mbar, suggesting that the surface area of the materials govern the adsorption behavior within this pressure range. Due to the comparable surface areas and pore volumes of the five MOFs, the adsorption curves overlap, indicating similar adsorption performance within these pressure levels.

The focus of this study lies within the low-pressure region of the SO_2 adsorption curve, where the open metal sites (OMSs) on MOFs play the crucial role in binding SO_2 molecules. In contrast to the high-pressure region, the adsorption of SO_2 exhibited significant variations among the five MIL-100-M MOFs, as shown in Figure 3-3(b). MIL-100-Sc and MIL-100-In demonstrated notably higher SO_2 loadings compared to the other three MOFs (MIL-100-Al, MIL-100-V, and

MIL-100-Fe). Particularly, the adsorption isotherm of SO_2 on MIL-100-Sc displayed a type-I-like behavior, with a sharp uptake of 1.5 mmol/g at 5 mbar, possibly indicating favorable interactions between OMS-Sc and SO_2 molecules. Interestingly, it was observed that MOFs containing lighter metals exhibited higher SO_2 uptakes than those with lighter metals in the same row of the periodic table (MIL-100-Sc > MIL-100-V > MIL-100-Fe). One hypothesis to explain this behavior is that trivalent metals with less electronegativity will demonstrate higher uptake of SO_2 because the OMSs are more polar in the structure of the materials. Computational approaches will be further applied to acquire a comprehensive understanding of the molecular mechanisms underlying the adsorption behaviors of SO_2 for all five MIL-100-M MOFs in the next section.

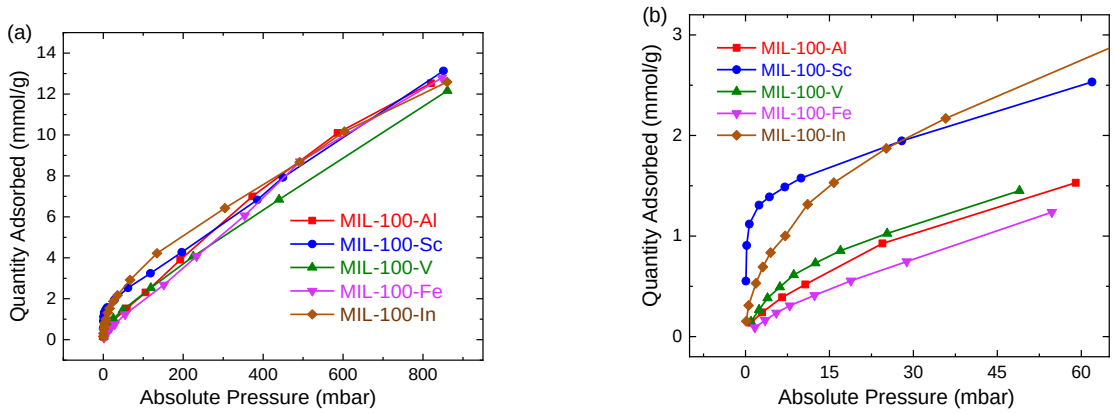

Figure 3-3: (a), SO_2 isotherms of MIL-100-M; (b), SO_2 isotherms of MIL-100-M at low partial pressures.

CO_2 is a commonly present component in flue gas and often competes with SO_2 for binding sites in adsorbents due to their similar characteristics and higher concentrations. To assess the selective capability of trivalent metals in MIL-100-M towards SO_2 over CO_2, CO_2 adsorption isotherms were also measured for all MIL-100-M materials, as depicted in Figure 3-4(a), and a detailed comparison of SO_2 and CO_2 adsorption for MIL-100-Sc is illustrated in Figure 3-4(b). In

Figure 3-4(a), the results clearly demonstrate that different MIL-100-M MOFs exhibit varying CO_2 uptake at 25 ℃ and 1000 mbar, with the order of Sc ≈ In > Fe > V ≈ Al. The highest loading of CO_2 (1.65 mmol/g) was obtained in MIL-100-Sc, which is quite low when compared to the capacity for SO_2 adsorption. Figure 3-4(b) shows ultrahigh selectivity of MIL-100-Sc for SO_2 over CO_2, highlighting the potential of MIL-100-Sc for the selective capture of SO_2. The ideal adsorbed solution theory (IAST) selectivity of SO_2 over CO_2 was calculated with a ratio of SO_2/CO_2 of 1:99 (a common ratio of SO_2/CO_2 in a typical flue gas) at 25 ℃ and 1000 mbar, and the results are presented in Table 3-1. All calculated values were significantly greater than 1 demonstrating that OMSs interact more strongly with SO_2 molecules than CO_2 molecules. This behavior is likely attributed to the higher dipole moment (1.62 D) and polarizability (47.7×10^{-25} cm^3) of SO_2 compared to CO_2 (0 D and 26.5×10^{-25} cm^3).[25-26] Impressively, an outstanding MIL-100-Sc performed record-high selectivity of SO_2/CO_2 (415), significantly higher than the other reported results (the highest reported was 325 in the literature).[25-30] This high selectivity indicates that MIL-100-Sc could be a good adsorbent candidate for separating SO_2 selectively from a stream of flue gas containing a large amount of CO_2.

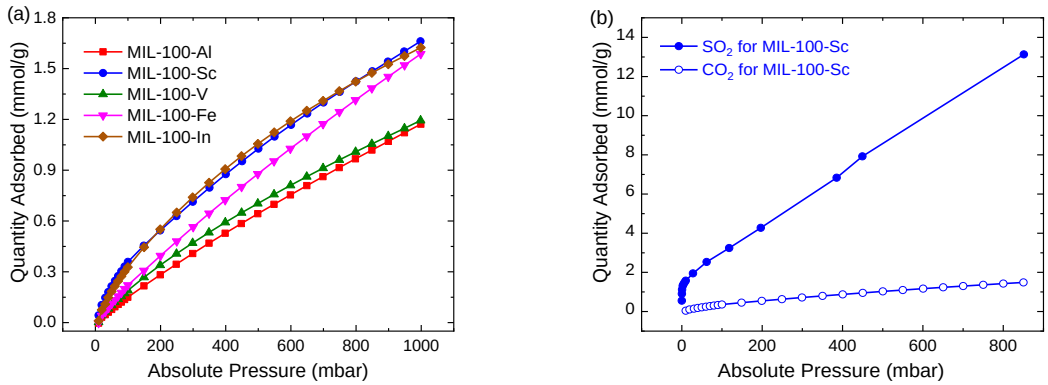

Figure 3-4: (a), CO_2 isotherms of MIL-100-M; (b), a comparison of SO_2 and CO_2 isotherms for MIL-100-Sc.

Table 3-1: IAST Selectivity of SO_2/CO_2 for MIL-100-M MOFs.

MOFs	IAST Selectivity calculated by IAST++
MIL-100-Al	43
MIL-100-Sc	415
MIL-100-V	48
MIL-100-Fe	15
MIL-100-In	96

3.3.3 SO_2 stability (Dry and humid)

The chemical stability of MOFs plays a vital role in their practical applications. The utilization of MOFs for SO_2 adsorption poses a significant challenge due to the highly corrosive and reactive nature of SO_2, which can result in severe structural degradation. In this chapter, the

stability of MIL-100-M MOFs was thoroughly investigated by examining their PXRD patterns and BET surface areas before and after exposure to dry SO_2, water vapor, and humid SO_2 (A mixture of 1000 ppm of SO_2 with 60% relative humidity). Figure 3-5 presents the PXRD results for Sc-MIL-100 and In-MIL-100 before and after each treatment. Remarkably, MIL-100-Sc exhibited consistent PXRD patterns before and after all three treatments, suggesting no significant change in its crystallinity and indicating its robust stability. Similarly, MIL-100-In maintained its characteristic peaks after exposure to dry SO_2, indicating its preserved crystallinity. However, notable alterations in the PXRD patterns of MIL-100-In were observed upon exposure to water vapor and humid SO_2, indicating its poor stability under these conditions, leading to varying degrees of structural destruction. Moreover, MIL-100-Al exhibited comparable behavior to MIL-100-Sc, while MIL-100-V and MIL-100-Fe displayed similar characteristics to MIL-100-In, suggesting their susceptibility to structural changes under the investigated conditions.

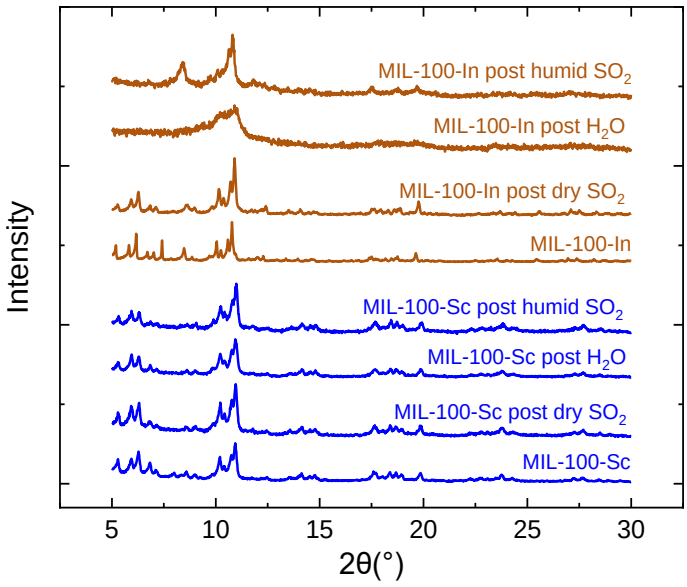

Figure 3-5: PXRD patterns of Sc-MIL-100 and In-MIL-100 with different treatments.

Furthermore, the BET surface areas of MIL-100-M after different treatments were also collected and are presented in Table 3-2. The results reveal that MIL-100-Al and MIL-100-Sc exhibit exceptional stability, as they retained approximately 90% of their original BET surface areas after all three exposures. Thus, these two MOFs appear to be capable of withstanding the corrosive and reactive nature of SO_2, water vapor, and humid SO_2 without compromising their porosity and surface areas, confirming their robust chemical stability and resistance to these harsh conditions. In the case of MIL-100-V, MIL-100-Fe, and MIL-100-In, the maintenance of BET surface areas after exposure to dry SO_2 suggests that these MOFs possess a certain level of stability against this specific gas. This observation aligns with the results obtained from the PXRD analysis, further confirming their ability to withstand the influence of dry SO_2 without significant structural deterioration. However, the significant reductions in BET surface areas observed after exposure to water vapor and humid SO_2 indicate that the pore structures of these MOFs are susceptible to collapse under these particular conditions. Apparently, the metal sites in MOFs play crucial roles in the stability of those materials. MIL-100-V, MIL-100-Fe, and MIL-100-In appear to collapse while MIL-100-Al and MIL-100-Sc maintain their crystallinity and porosity that may be attributed to the larger radius of V, Fe, and In compared to Al and Sc, resulting in lower charge density. Consequently, the metal-ligand bonds in MIL-100-V, MIL-100-Fe, and MIL-100-In are much weaker. On the other hand, V, Fe, and In are more prone to hydrolysis than Al and Sc. Hence, the presence of water vapor and humid SO_2 easily damages the structure of MIL-100-V, MIL-100-Fe, and MIL-100-In, leading to a decrease in surface area and potentially impacting their adsorption capabilities. These findings underscore the significance of the metal species for the stability of MOFs under diverse environmental conditions.

Table 3-2: Summary of BET surface areas of MIL-100-M with different treatments.

MIL-100-M	Pristine (m^2/g)	Post dry SO_2 (m^2/g)	Post water vapor (m^2/g)	Post humid SO_2 (m^2/g)
MIL-100-Al	1359	1281	1300	1212
MIL-100-Sc	1408	1362	1412	1250
MIL-100-V	1459	1267	247	375
MIL-100-Fe	1350	1221	719	145
MIL-100-In	1319	1192	423	159

3.3.4 Post trivalent metal insertion for UiO-66-2COOM

To examine the impact of post-synthetic metal insertion on the functionality of trivalent metals in MOFs, a series of UiO-66-2COOM (M = Al, Sc, Fe, Ga, and In.) was successfully synthesized. To ensure a diverse representation of elements in both a column and row of the periodic table, vanadium was omitted from the list and gallium was included compared to the trivalent metals for MIL-100-M study. The crystallinity of the obtained UiO-66-2COOM samples was checked by using a state-of-the-art XPert PRO Alpha-1 diffraction system with Cu Kα radiation (λ = 1.542 Å), and the resulting PXRD patterns are illustrated in Figure 3-6(a). Remarkably, all the synthesized samples exhibit identical PXRD patterns, indicating that the introduction of metals does not alter the crystalline structure of the parent MOFs, and they retain the same unit cell as UiO-66-2COOH, confirming the successful synthesis of UiO-66-2COOM,

enabling the evaluation of metal insertion and its influence on the functionality of trivalent metals in MOFs. To assess the porosity of UiO-66-2COOH and UiO-66-2COOM, N_2 adsorption measurements were conducted at a cryogenic temperature of -196 ℃. The analysis reveals that the BET surface areas of UiO-66-2COOM are slightly smaller than those of pristine UiO-66-2COOH as shown in Figure 3-6(b). This disparity can be attributed to the incorporation of metal species that occupy a portion of the pore space within the MOF structure.

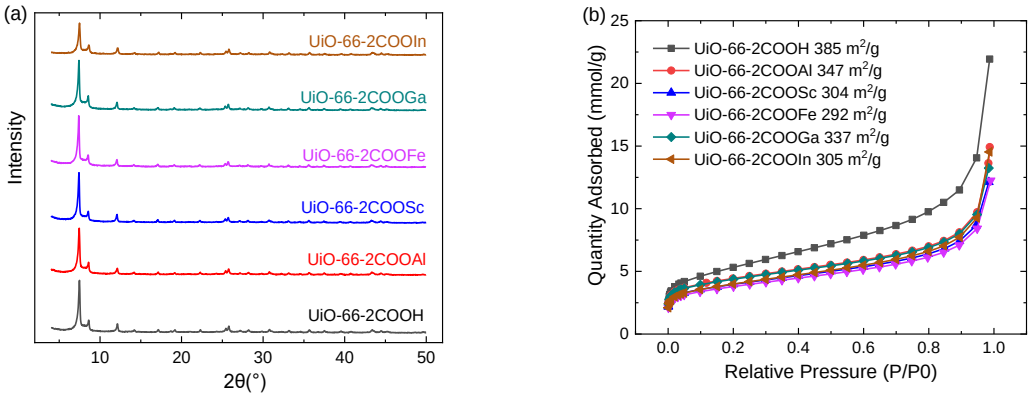

Figure 3-6: (a), PXRD of UiO-66-2COOM; (b), N_2 adsorption isotherms of UiO-66-2COOM.

3.3.5 Humid SO_2 stability

To tackle the significant challenge posed by water vapor-induced degradation of crystal structures observed in various MIL-100-M members, a strategic approach involving the implementation of a metal insertion process was applied to UiO-66-2COOH. Since the introduced post-synthesis metal sites are not the "structural pillar" of the framework, the attack of humid SO_2 on these sites will not cause the structural collapse of the pristine materials. To assess the stability of the resulting UiO-66-2COOM samples, comprehensive PXRD and N_2 adsorption experiments were conducted before and after subjecting them to humid SO_2 exposure. As depicted in Figure 3-

7, the diffractograms of all UiO-66-2COOM samples post-humid SO_2 exposure experiments closely match their respective origins, providing compelling evidence of the exceptional chemical stability exhibited by all variations of UiO-66-2COOM. Moreover, the outcomes of the N_2 adsorption experiments further solidify this assertion. As summarized in Table 3-3, all UiO-66-2COOM samples retain over 92% of their original BET surface areas, thus affirming their ability to preserve their crucial porosity even after being exposed to humid SO_2 stream.

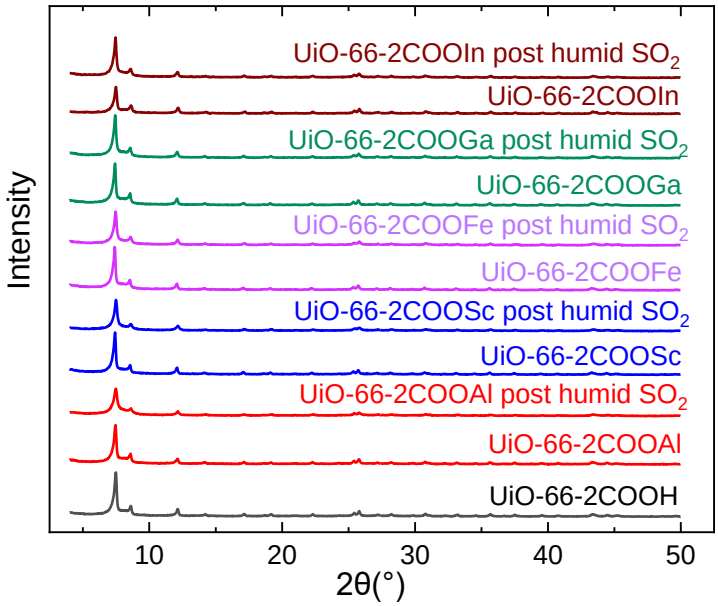

Figure 3-7: PXRD patterns of UiO-66-2COOM before and after humid SO_2 exposure

Table 3-3: BET surface areas of UiO-66-2COOM before and after humid SO_2 exposure

MOFs	BET Surface area (m^2/g)		Preserved
	Before	After	
UiO-66-2COOAl	347	337	97.0%
UiO-66-2COOSc	304	291	95.7%
UiO-66-2COOFe	292	292	100%
UiO-66-2COOGa	337	313	92.9%
UiO-66-2COOIn	305	298	97.7%

3.3.6 SO_2 adsorption of UiO-66-2COOM

As discussed earlier, the trivalent metals in the MIL-100-M framework showcased a diverse range of affinities toward SO_2 molecules. To investigate whether the introduced trivalent metals in the UiO-66-2COOM series will exhibit comparable behavior to their MIL-100-M counterparts, a comprehensive assessment of SO_2 isotherms was conducted on each UiO-66-2COOM sample. The resulting SO_2 isotherms are depicted in Figure 3-8(a). Notably, UiO-66-2COOSc and UiO-66-2COOIn prominently display the highest loadings of SO_2 among all the UiO-66-2COOM samples. This correlation between the SO_2 isotherms of the UiO-66-2COOM series and those of MIL-100-M underscores the similarity in the performance of the introduced metals within UiO-66-2COOM and the framework open metal sites (OMSs) found in MIL-100-M, specifically in relation to SO_2 adsorption. XPS results as shown in Figure 3-8(b) and (c)

confirmed that the inserted metals in UiO-66-2COOM exhibited the same chemical states as the OMSs in MIL-101-M. The consistent behavior observed across the two frameworks further validates the efficacy of the metal insertion approach employed in UiO-66-2COOM for harnessing the desired adsorption properties of trivalent metals. By combining the findings in section 3.3.5 with the results presented here, it has been demonstrated that post-synthetic metal insertion into UiO-66-2COOM accomplishes two significant goals. Firstly, it successfully addresses the potential stability concerns associated with OMS MOFs. Secondly, it effectively replicates the functionality of OMSs in MIL-100-M for SO_2 capture. This serves as a good example of the post-synthetic metal insertion process in MOFs, showcasing its ability to emulate OMS functions while overcoming stability challenges.

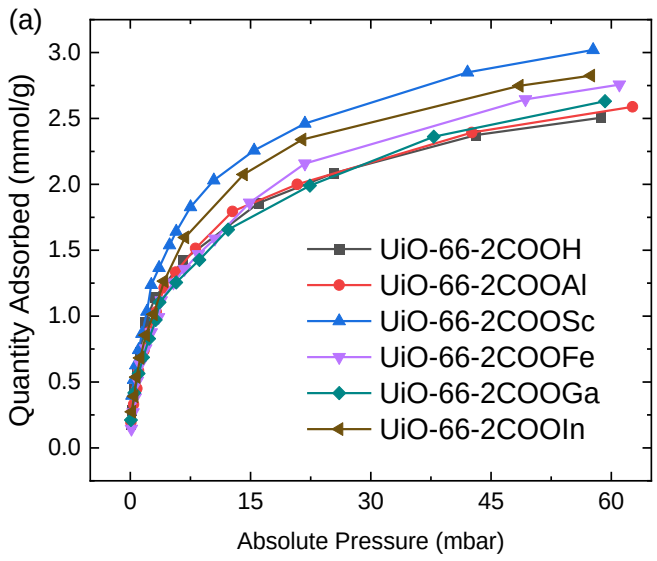

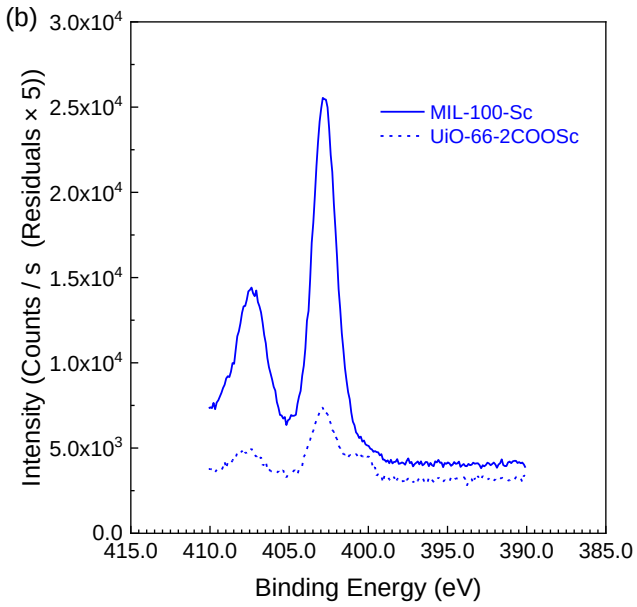

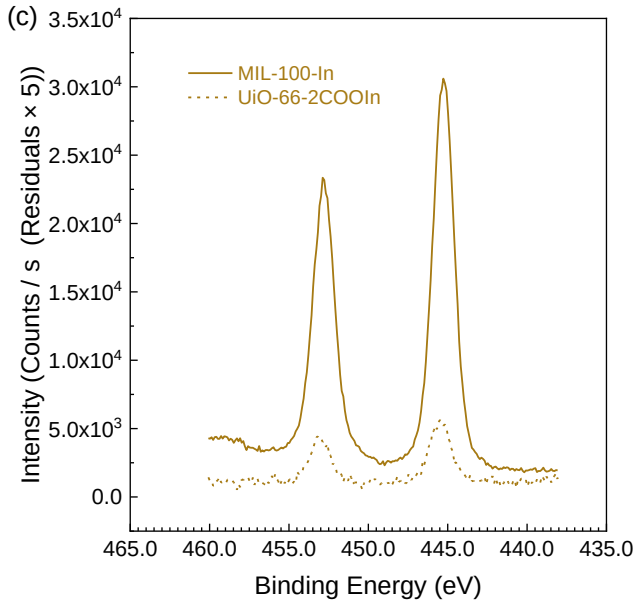

Figure 3-8: (a) SO_2 isotherms of UiO-66-2COOM, (b) Sc XPS spectra of MIL-100-Sc and UiO-66-2COOSc, and (c) In XPS spectra of MIL-100-In and UiO-66-2COOIn.

3.4 Conclusions

In conclusion, this chapter presented the synthesis and characterization of MIL-100-M compounds with diverse trivalent metal sites and investigated their adsorption properties for SO_2, specifically focusing on their interaction with SO_2 molecules. These MIL-100-M MOFs were successfully prepared with consistent crystallinity and similar porosity, ensuring a fair comparison of their properties. Through the analysis of SO_2 isotherms, a clear trend emerged, revealing that the affinity of trivalent metals towards SO_2 aligns with the electronegativity trend, with metals of lower electronegativity exhibiting a stronger affinity for SO_2 for metal elements in a same row of the periodic table. Among the MIL-100-M series, MIL-100-Sc stood out by demonstrating superior uptake of SO_2 at low partial pressures, larger IAST selectivity for SO_2 over CO_2, and excellent stability against water vapor and humid SO_2 exposure. Moreover, the post-metal insertion approach was applied to modify UiO-66-2COOH with trivalent metals, resulting in UiO-66-2COOM compounds that exhibited robust stability when exposed to humid SO_2 conditions. Notably, UiO-66-2COOSc and UiO-66-2COOIn displayed higher SO_2 uptake compared to the other UiO-66-2COOM samples, demonstrating that the post-introduced metals within UiO-66-2COOM can mimic the functionality of OMSs in MIL-100-M. These findings hold great promise for addressing stability challenges in MOFs featuring OMSs while simultaneously preserving their exceptional adsorption properties. Future research efforts can further explore and optimize the post-metal insertion strategy to enhance the stability and performance of MOFs with OMSs, contributing to the advancement of sustainable materials with tailored properties.

3.5 References

1. Poloni, R.; Lee, K.; Berger, R. F.; Smit, B.; Neaton, J. B., Understanding trends in CO_2 adsorption in metal–organic frameworks with open-metal sites. *The journal of physical chemistry letters* **2014,** *5* (5), 861-865.

2. Chen, B.; Ockwig, N. W.; Millward, A. R.; Contreras, D. S.; Yaghi, O. M., High H_2 adsorption in a microporous metal–organic framework with open metal sites. *Angewandte Chemie International Edition* **2005,** *44* (30), 4745-4749.

3. Wu, H.; Zhou, W.; Yildirim, T., High-capacity methane storage in metal− organic frameworks M_2 (dhtp): the important role of open metal sites. *Journal of the American Chemical Society* **2009,** *131* (13), 4995-5000.

4. Zhang, Y.; Li, B.; Krishna, R.; Wu, Z.; Ma, D.; Shi, Z.; Pham, T.; Forrest, K.; Space, B.; Ma, S., Highly selective adsorption of ethylene over ethane in a MOF featuring the combination of open metal site and π-complexation. *Chemical communications* **2015,** *51* (13), 2714-2717.

5. Li, W.; Li, J.; Duong, T. D.; Sapchenko, S. A.; Han, X.; Humby, J. D.; Whitehead, G. F.; Victórica-Yrezábal, I. J.; Da Silva, I.; Manuel, P., Adsorption of Sulfur Dioxide in Cu (II)-Carboxylate Framework Materials: The Role of Ligand Functionalization and Open Metal Sites. *Journal of the American Chemical Society* **2022,** *144* (29), 13196-13204.

6. Xie, J.; Yan, N.; Qu, Z.; Yang, S., Synthesis, characterization and experimental investigation of Cu-BTC as CO_2 adsorbent from flue gas. *Journal of Environmental Sciences* **2012,** *24* (4), 640-644.

7. Tan, K.; Zuluaga, S.; Wang, H.; Canepa, P.; Soliman, K.; Cure, J.; Li, J.; Thonhauser, T.; Chabal, Y. J., Interaction of acid gases SO_2 and NO_2 with coordinatively unsaturated metal organic frameworks: M-MOF-74 (M= Zn, Mg, Ni, Co). *Chemistry of Materials* **2017,** *29* (10), 4227-4235.

8. Gómez‐Pozuelo, G.; Cabello, C. P.; Opanasenko, M.; Horáček, M.; Čejka, J., Superior Activity of Isomorphously Substituted MOFs with MIL‐100 (M= Al, Cr, Fe, In, Sc, V) Structure in the Prins Reaction: Impact of Metal Type. *ChemPlusChem* **2017,** *82* (1), 152-159.

9. Zhong, G.; Liu, D.; Zhang, J., Applications of porous metal–organic framework MIL-100 (M)(M= Cr, Fe, Sc, Al, V). *Crystal Growth & Design* **2018,** *18* (12), 7730-7744.

10. Steenhaut, T.; Filinchuk, Y.; Hermans, S., Aluminium-based MIL-100 (Al) and MIL-101 (Al) metal–organic frameworks, derivative materials and composites: synthesis, structure, properties and applications. *Journal of Materials Chemistry A* **2021,** *9* (38), 21483-21509.

11. Burtch, N. C.; Jasuja, H.; Walton, K. S., Water stability and adsorption in metal–organic frameworks. *Chemical reviews* **2014,** *114* (20), 10575-10612.

12. Rowsell, J. L.; Yaghi, O. M., Strategies for hydrogen storage in metal–organic frameworks. *Angewandte Chemie International Edition* **2005,** *44* (30), 4670-4679.

13. Bohnsack, A. M.; Ibarra, I. A.; Bakhmutov, V. I.; Lynch, V. M.; Humphrey, S. M., Rational design of porous coordination polymers based on bis (phosphine) MCl_2 complexes that exhibit high-temperature H_2 sorption and chemical reactivity. *Journal of the American Chemical Society* **2013,** *135* (43), 16038-16041.

14. Mohamed, M. H.; Yang, Y.; Li, L.; Zhang, S.; Ruffley, J. P.; Jarvi, A. G.; Saxena, S.; Veser, G. t.; Johnson, J. K.; Rosi, N. L., Designing open metal sites in metal–organic frameworks for paraffin/olefin separations. *Journal of the American Chemical Society* **2019,** *141* (33), 13003-13007.

15. Ye, Z.; Liu, Y.; Fang, C.; Chen, W.; Ou, M.; Li, L.; Lin, X.; Rao, Z.; Liao, Y.; Zhao, R., Coordination induced electron redistribution to achieve highly reversible Li-ion insertion chemistry in metal–organic frameworks. *Chemical Communications* **2020**.

16. Getman, R. B.; Miller, J. H.; Wang, K.; Snurr, R. Q., Metal alkoxide functionalization in metal− organic frameworks for enhanced ambient-temperature hydrogen storage. *The Journal of Physical Chemistry C* **2011,** *115* (5), 2066-2075.

17. Liu, J.; Strachan, D. M.; Thallapally, P. K., Enhanced noble gas adsorption in Ag@ MOF-74Ni. *Chemical Communications* **2014,** *50* (4), 466-468.

18. Mulfort, K. L.; Farha, O. K.; Stern, C. L.; Sarjeant, A. A.; Hupp, J. T., Post-synthesis alkoxide formation within metal− organic framework materials: a strategy for incorporating highly coordinatively unsaturated metal ions. *Journal of the American Chemical Society* **2009,** *131* (11), 3866-3868.

19. Volkringer, C.; Popov, D.; Loiseau, T.; Férey, G.; Burghammer, M.; Riekel, C.; Haouas, M.; Taulelle, F., Synthesis, single-crystal X-ray microdiffraction, and NMR characterizations of the giant pore metal-organic framework aluminum trimesate MIL-100. *Chemistry of Materials* **2009,** *21* (24), 5695-5697.

20. Cabello, C. P.; Rumori, P.; Palomino, G. T., Carbon dioxide adsorption on MIL-100 (M)(M= Cr, V, Sc) metal–organic frameworks: IR spectroscopic and thermodynamic studies. *Microporous and Mesoporous Materials* **2014,** *190*, 234-239.

21. Simon, M. A.; Anggraeni, E.; Soetaredjo, F. E.; Santoso, S. P.; Irawaty, W.; Thanh, T. C.; Hartono, S. B.; Yuliana, M.; Ismadji, S., Hydrothermal synthesize of HF-free MIL-100 (Fe) for isoniazid-drug delivery. *Scientific reports* **2019,** *9* (1), 1-11.

22. Joshi, J. N.; Garcia-Gutierrez, E. Y.; Moran, C. M.; Deneff, J. I.; Walton, K. S., Engineering copper carboxylate functionalities on water stable metal–organic frameworks for enhancement of ammonia removal capacities. *The Journal of Physical Chemistry C* **2017,** *121* (6), 3310-3319.

23. Walton, K. S.; Snurr, R. Q., Applicability of the BET method for determining surface areas of microporous metal− organic frameworks. *Journal of the American Chemical Society* **2007,** *129* (27), 8552-8556.

24. Lee, S.; Lee, J. H.; Kim, J., User-friendly graphical user interface software for ideal adsorbed solution theory calculations. *Korean Journal of Chemical Engineering* **2018,** *35* (1), 214-221.

25. Zhang, Y.; Zhang, P.; Yu, W.; Zhang, J.; Huang, J.; Wang, J.; Xu, M.; Deng, Q.; Zeng, Z.; Deng, S., Highly selective and reversible sulfur dioxide adsorption on a microporous metal–organic framework via polar sites. *ACS applied materials & interfaces* **2019,** *11* (11), 10680-10688.

26. Chen, F.; Lai, D.; Guo, L.; Wang, J.; Zhang, P.; Wu, K.; Zhang, Z.; Yang, Q.; Yang, Y.; Chen, B., Deep desulfurization with record SO_2 adsorption on the metal–organic frameworks. *Journal of the American Chemical Society* **2021,** *143* (24), 9040-9047.

27. Zhang, Y.; Chen, Z.; Liu, X.; Dong, Z.; Zhang, P.; Wang, J.; Deng, Q.; Zeng, Z.; Zhang, S.; Deng, S., Efficient SO_2 removal using a microporous metal–organic framework with molecular sieving effect. *Industrial & Engineering Chemistry Research* **2019,** *59* (2), 874-882.

28. Brandt, P.; Nuhnen, A.; Lange, M.; Möllmer, J.; Weingart, O.; Janiak, C., Metal–organic frameworks with potential application for SO2 separation and flue gas desulfurization. *ACS applied materials & interfaces* **2019,** *11* (19), 17350-17358.

29. Zárate, J. A.; Sánchez-González, E.; Williams, D. R.; González-Zamora, E.; Martis, V.; Martínez, A.; Balmaseda, J.; Maurin, G.; Ibarra, I. A., High and energy-efficient reversible SO 2 uptake by a robust Sc (iii)-based MOF. *Journal of Materials Chemistry A* **2019,** *7* (26), 15580-15584.

30. Savage, M.; Cheng, Y.; Easun, T. L.; Eyley, J. E.; Argent, S. P.; Warren, M. R.; Lewis, W.; Murray, C.; Tang, C. C.; Frogley, M. D., Selective adsorption of sulfur dioxide in a robust metal–organic framework material. *Advanced materials* **2016,** *28* (39), 8705-8711.

CHAPTER 4. ENHANCING SO_2 CAPTURE: UNVEILING THE POTENTIAL OF DETA-BASED ILS FOR MIL-101 FUNCTIONALIZATION

4.1 Introduction

Ionic liquids (ILs) are promising materials formed by cations and anions that have received significant interest in academic research and industrial applications.[1-2] Unlike conventional salts, which typically have high melting points, ionic liquids are characterized by their low volatility and often exhibit liquid properties below 100°C. The distinctive feature of ionic liquids lies in their ability to remain in a liquid state due to the formation of strong electrostatic interactions between the cations and anions, rather than relying on a traditional molecular solvent framework. These strong ionic interactions give rise to unique properties, such as high thermal stability, low vapor pressure, and high ionic conductivity.[3-5] Ionic liquids have been considered one of the environmentally friendly alternatives to volatile organic solvents because of their attractive features. Moreover, they provide a broad range of tunability for different purposes by adjusting the combination of cations and anions. ILs have been studied for SO_2 capture, and guanidinium-, hydroxyl ammonium-, and imidazolium-based ILs are identified as suitable for SO_2 adsorption due to the presence of amine or nitrogen-related functional groups.[6-8] Although ILs meet several requirements of excellent candidates for flue-gas desulfurization, including mediate interactions that guarantee adsorption capacity, and resistance to high temperature, their high viscosity and low surface area limit their industrial applications.

Great efforts have been devoted to overcoming these issues by introducing ILs into porous substrates to enhance mass transport and diffusivity. Several types of substrate materials have been investigated for this purpose, such as activated carbon[9-10], silica gel[11-12], mesoporous silica materials (i.e. MCM-41 and SBA-15)[13-14], and metal-organic frameworks (MOFs)[15-16]. For example, Zhang and co-workers demonstrated that the grafting of 1,3-bispropyltriethoxysilane-imidazolium chloride into SBA-15 possessed rapid and facile adsorption properties for SO_2 with improved adsorption rate ($t_{0.9}$ value 1-2 orders of magnitude lower).[17] Clearly, a suitable substrate must have a high surface area and large pore volume for an amount of ILs immobilization and favorable interaction with ILs for their stabilization in the substrate.

MOFs are crystalline porous materials constructed by metal ions or clusters with organic ligands. Over the past decades, MOFs have shown great potential in gas adsorption and separation[18-19], catalysis[20], sensing[21], and drug delivery[22-23] applications due to their high surface area (up to 2.3 cm^3/g), large pore volume (up to 7 000 m^2/g), and functional tunability.[24] MOFs can perform as an ideal substrate for the incorporations of ILs, and the ILs-MOF composites have been reported to display remarkably enhanced properties in various fields[16]. For instance, Xu and co-workers demonstrated the utilization of acidic ILs-based UiO-67 for esterification and found that the ILs-UiO-67 performed the maximum isoctyl alcohol conversion of 98.6% with an outstanding cyclability.[25] ILs-MIL-53(Al) has been investigated for CO_2 capture and gave a 3.3 times higher CO_2/N_2 selectivity than that of the pristine MIL-53(Al). Therefore, incorporating ILs with MOFs is promising for flue-gas desulfurization.

In this chapter, MIL-101 has been selected as the substrate for ILs incorporation owing to its large surface area, pore volume and physical and chemical stability. Diethylenetriamine (DETA), diethylenetriamine chloride (DETA-Cl), diethylenetriamine acetate (DETA-Ace), and

diethylenetriamine lactate (DETA-Lac) have been used to modify MIL-101 through a post-synthetic functionalization approach (as displayed in Figure 4-1). The introduced post-synthesis compounds can be stabilized on MIL-101 by covalent coordination between the open Cr sites on MIL-101 and nitrogen sites of DETA or DETA-based ILs which could be evidenced by XPS measurements. Isotherm results confirmed that the grafting DETA or DETA-based ILs can facilitate SO_2 capture. Additionally, the DRIFTs results shed light on the reversibility of SO_2 adsorption on the modified composites, contrasting with the irreversible adsorption observed on MIL-101. Remarkably, the presence of the grafted compounds acted as guardians, shielding the MOF frameworks from potential intrusions by preventing the attachment of foreign species to the open metal sites. This protective function serves to fortify the structural integrity of the MOF materials.

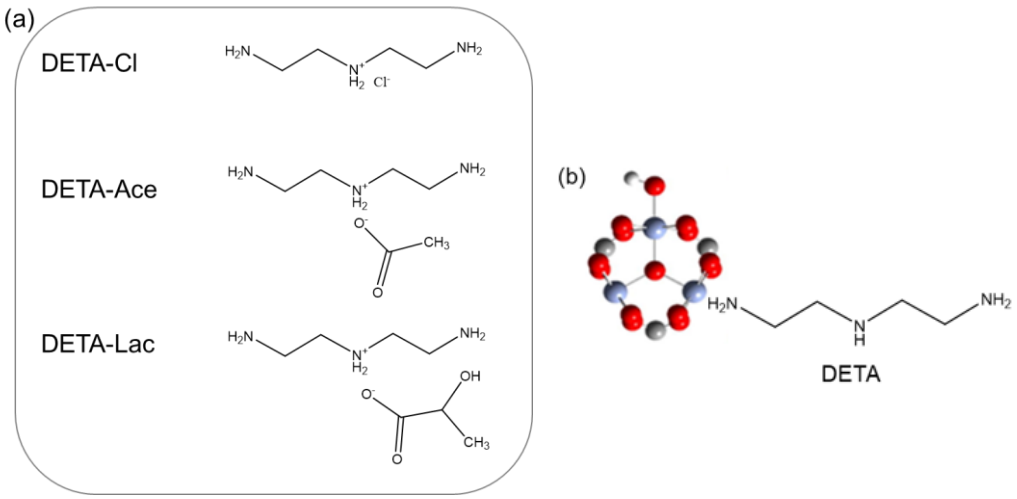

Figure 4-1: (a) Schematic structures of ILs, (b) DETA coordinated metal cluster of MIL-101.

4.2 Experimental section

4.2.1 Materials

MIL-101: To synthesize MIL-101, we followed the established procedures described by Lalit et al[26]. The synthesis process involved dissolving chromic nitrate ($Cr(NO_3)_3$) and 332 mg of terephthalic acid (BDC) in 10 mL of deionized water within a glass beaker. To modulate the reaction, 1.5 mL of 36% acetic acid was added to the solution. Additionally, 5 mg of MIL-101 crystals were introduced as seed crystals during the synthesis. Subsequently, the resulting mixture was transferred to a 100 mL PTFE-lined autoclave encased in stainless steel and placed inside an isothermal oven at a temperature of 200 ℃ for a duration of 12 hours. The synthesized product was then obtained by centrifugation at 8,000 rpm and subjected to a thorough washing process involving three cycles of dimethylformamide (DMF) followed by methanol rinses.

Ionic liquids: The ILs were all simple neutralizations of a 1:1 DETA : Acid (Hydrogen chloride, Acetic acid, or lactic acid) mixtures. In brief, a solution of the appropriate DETA was dissolved in water and the acid was added to this dropwise. The mixture was stirred at room temperature for 1 hour and then the water evaporated. The ILs were dried at 50 ℃ for 24 hours to yield the final viscous liquids or solids, and the structures are shown in Figure 4-1.

MIL-101-ILs: To incorporate ILs, a solution was prepared by dissolving 1 mmol of ILs in 10 mL of methanol. Subsequently, 0.2 g of activated MIL-101 was added to the solution. The resulting mixture was stirred at room temperature for 24 hours, allowing for sufficient interaction between the ILs and the MOF. Following the reaction, the solid was separated from the solution using centrifugation. To remove any unattached ILs, methanol was used for elution. Finally, the

obtained product was dried overnight at 60 ℃ to ensure its stability and readiness for further analysis.

4.2.2 Characterization and measurements

The PXRD patterns of the synthesized MIL-101 and MIL-101-ILs composites were acquired using an XPert PRO Alpha-1 diffraction system, employing Cu Kα radiation (λ = 1.542 Å) under ambient conditions. The range of 2θ spanned from 2 to 30°, and data were collected continuously with a step size of 0.0167° per second. To determine the surface areas, N_2 physisorption measurements were conducted at -196 ℃, and calculations were performed utilizing the Brunauer, Emmett, and Teller (BET) model within a pressure range of $0.005 < P/P0 < 0.03$[27]. Before the adsorption measurements, all samples were initially activated at 105 ℃ for 15 hours. Thermogravimetry analysis (TGA) were performed up to 600 ℃ at a heating rate of 5 ℃/min under a N_2 flow. X-ray photoelectron spectroscopy (XPS) was employed to investigate the chemical state of ILs in MIL-101 by using a Thermo K-Alpha XPS analyzer.

SO_2 and CO_2 adsorption isotherms: In order to determine the adsorption isotherms of SO_2 and CO_2, a home-built pressure decay system and a Micromeritics 3Flex Surface Characterization Analyzer were utilized. High-purity SO_2 and CO_2 gases were employed for the respective measurements. The adsorption experiments were conducted under constant temperature conditions, with precise control over the changes in partial pressures within the sample chamber or tube. The isotherms of SO_2 and CO_2 were recorded at 25 ℃, following a prior activation step of all samples under vacuum at 105 ℃ for a duration of 15 hours. For more detailed information regarding the design and setup of the pressure decay system, please refer to Appendix B. To

perform the necessary calculations, the Ideal Adsorbed Solution Theory (IAST) was applied, with the actual calculations carried out using the IAST++ interface[28].

DRIFTS measurements: Diffuse reflectance infrared Fourier transform spectroscopy (DRIFTS) experiments were conducted in situ with a resolution of 4 cm^{-1} using a Thermo Scientific Nicolet iS10 FTIR equipped with a Smart iTX accessory[29].

4.3 Results and discussion

4.3.1 Crystallinity and porosity of materials

MIL-101, MIL-101-DETA, and DETA-based MIL-101-IL composites were successfully synthesized and the crystal structures of these materials were confirmed through PXRD analysis. Notably, the PXRD patterns of both MIL-101-DETA and DETA-based MIL-101-ILs exhibited a high degree of consistency with that of the parent MOFs, MIL-101, as depicted in Figure 4-2(a). This observation indicates that the impregnation of DETA and ILs into the MOFs did not lead to any significant alterations or damage to the crystal structure. It is worth mentioning that noticeable variations in the intensity of the same characteristic peaks among the different samples was observed, which can be attributed to changes in electron density arising from the presence of ILs within the pores of the MOFs[30], suggesting that DETA and DETA-based ILs can be successfully incorporated into MIL-101 while maintaining its crystal structure.

The BET surface areas of the samples were determined through N_2 adsorption experiments conducted at -196 ℃, and the results are illustrated in Figure 4-2(b). As expected, MIL-101 exhibited a remarkably high BET surface area of 2315 m^2/g, indicating its potential as a suitable substrate for the post-introduction of ionic liquids. MIL-101-DETA, MIL-101-DETA-Cl, and

MIL-101-Ace demonstrated similar surface areas, around 1000 m^2/g, indicating their comparable closed porosity. However, MIL-101-DETA-Lac exhibited the lowest surface area value of 410 m^2/g among the samples. In comparison to MIL-101, a significant decrease in the BET surface area was observed for all the composites. This reduction can be attributed to the occupation of MOF pores by the introduced ILs. Despite this decrease, the modified composites still retained sufficient free pore space, which remained effective for gas capture applications.

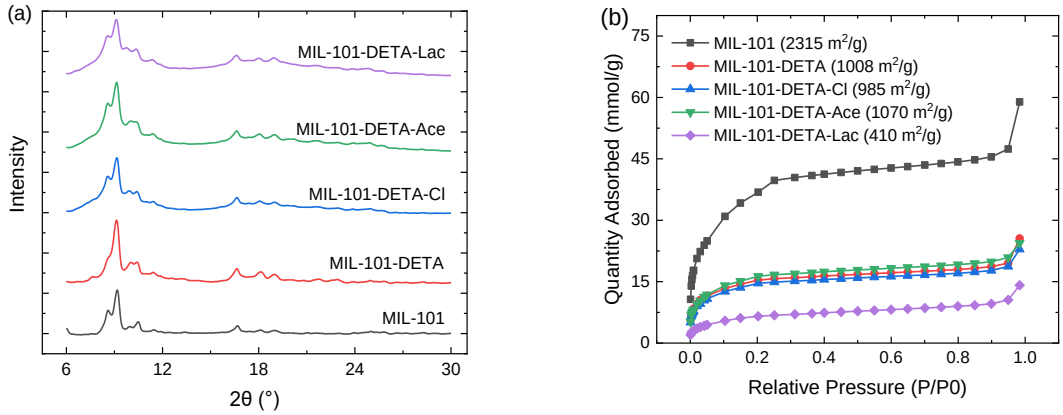

Figure 4-2: (a) PXRD patterns and (b) BET surface areas for MIL-101 and MIL-101 composites.

4.3.2 DETA and DETA-based ILs in MIL-101

Thermogravimetric analysis (TGA) was conducted to evaluate the loading of DETA and DETA-based ionic liquids (ILs) in MOF composites. TGA curves depicting the thermal behavior of the samples are presented in Figure 4-3. For MIL-101, and three degradation steps are observed. The first weight loss step occurs from room temperature to 150 ℃, which can be attributed to the removal of water present in the MOF pores and coordinated to the open Cr centers. The second step, spanning from 150 to 350 ℃, corresponds to the loss of lattice water or DMF molecules. The third step started at 350 ℃ indicates the decomposition of the organic linker within the MOFs.[31]

In the case of MIL-101-DETA-Lac, a similar three-step degradation pattern is observed. The first and third steps are attributed to the same processes as in MIL-101. However, the second step in MIL-101-DETA-Lac is assigned to the degradation of the impregnated DETA-Lac. Since lattice water or DMF molecules can be exchanged by the methanol used for impregnating DETA or DETA-based ILs, followed by their removal after synthesis, the overall weight loss of 22 % corresponds to the weight percentage of DETA-Lac in MIL-101-DETA-Lac. This value is further calculated to be 3.4 mmol/g based on the nitrogen content. The loadings of the other MOF composites are summarized in Table 4-1.

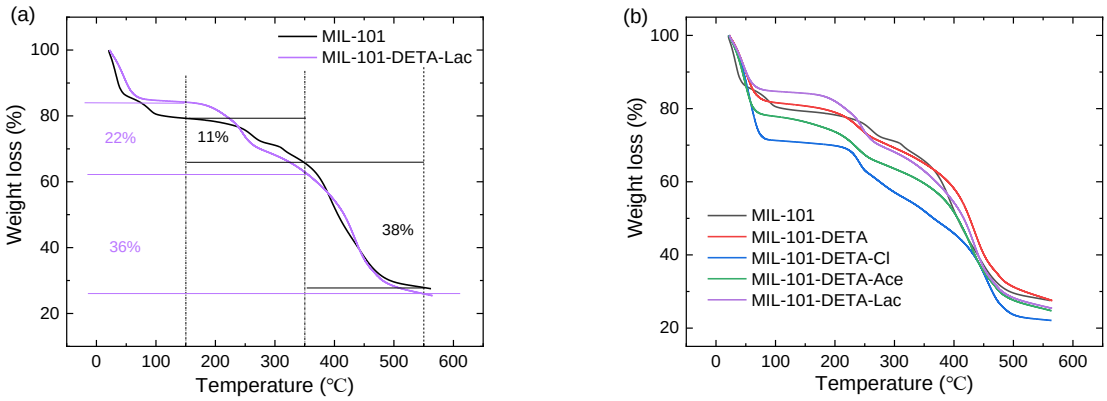

Figure 4-3: TGA curves of (a) MIL-101 and MIL-101-DETA-Lac and (b) MIL-101 and MIL-101 composites.

Table 4-1: Weight percentage of DETA or DETA-based ILs in MIL-101 composites.

Samples	Weight percentage of DETA or DETA-based ILs	N contents (mmol/g)
MIL-101-DETA	15%	4.3
MIL-101-DETA-Cl	18%	3.8
MIL-101-DETA-Ace	17%	3.1
MIL-101-DETA-Lac	22%	3.4

The chemical states and surface composition of the samples were examined through X-ray photoelectron spectroscopy (XPS) analysis, as shown in Figure 4-4. Figure 4-4(a) displays the XPS survey spectra of all five samples, revealing the presence of elements such as C, N, O, Cl, and Cr. In the case of MIL-101, a small peak corresponding to N1s was observed, which could be attributed to the residual solvent DMF used during sample synthesis. However, the percentage of nitrogen in MIL-101 was found to be relatively small (See Table 4-2). In contrast, sharp peaks at approximately 400 eV for N1s were prominently observed in the spectra of the other samples, strongly indicating the presence of DETA or DETA-based ionic liquids within the samples.

Figure 4-4(b) describes the XPS spectrum of chromium (Cr). In the MIL-101 sample, two distinct peaks at 587.1 eV and 577.3 eV were observed, corresponding to the energy levels of Cr 2p1/2 and Cr 2p3/2, respectively. Conversely, in MIL-101-DETA, the binding energies of Cr 2p1/2 and Cr 2p3/2 shifted to lower positions, specifically 586.5 eV and 576.6 eV, indicating an

enhanced electron density for the Cr(III) species. This shift suggests the occurrence of a covalent correlation between the exposed Cr sites and the nitrogen atoms of the NH_2 groups in DETA, confirming the interaction between MIL-101 and DETA. A similar trend was also observed for the other modified MIL-101 samples, further supporting the presence of chemical interactions between the MOF and the respective modifications, and highlighting the successful modification of the MOF with the desired functionality.

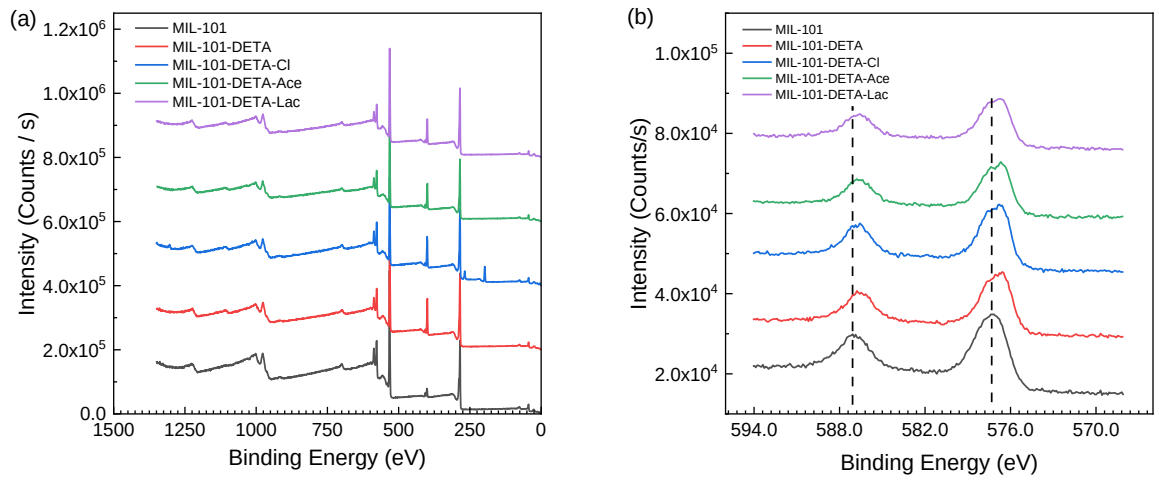

Figure 4-4: (a) XPS survey spectra (b) Cr XPS spectra of MIL-101 and MIL-101 composites.

Table 4-2: Atomic concentrations (at. %) of elements for the samples.

Elements	MIL-101	MIL-101-DETA	MIL-101-DETA-Cl	MIL-101-DETA-Ace	MIL-101-DETA-Lac
C	52.46	51.94	51.80	53.07	53.49
O	40.14	28.93	26.80	29.51	31.27
Cr	3.05	2.29	2.49	2.43	2.06
N	4.35	16.84	14.92	14.99	13.18
Cl	--	--	3.99	--	--

4.3.3 SO_2 adsorption and IAST selectivity

The adsorption behavior of SO_2 and CO_2 in MIL-101 and MIL-101 composites is elucidated in Figure 4-5. Figure 4-5(a) presents the SO_2 isotherms, revealing a distinct disparity between MIL-101 and its modified counterparts. Evidently, the modified MIL-101 materials exhibit significantly higher SO_2 adsorption compared to the pristine MIL-101, strongly implying that the incorporation of DETA and DETA-based ILs brings about notable benefits for SO_2 capture. Particularly in the ultra-low-pressure region (below 30 mbar), wherein binding sites play a pivotal role in the adsorption behavior, a remarkable enhancement in SO_2 uptake reaffirms the desirable nitrogen functionality of MIL-101. Notably, MIL-101-DETA-Ace exhibits the highest SO_2 adsorption capacity, followed by MIL-101-DETA-Cl and MIL-101-DETA-Lac, while MIL-101-DETA showcases slightly lower performance, indicating that the choice of anions in the ILs

also exerts a discernible impact on SO_2 capture. The influence of different anions of ILs on CO_2 adsorption is even more pronounced. Figure 4-5(b) showcases the CO_2 isotherms, where MIL-101-DETA-Ace outshines the other composites, demonstrating significantly higher CO_2 uptake compared to MIL-101-DETA-Cl and MIL-101-DETA-Lac. Notably, MIL-101-DETA-Lac and MIL-101 exhibit similar performance in CO_2 adsorption, likely owing to the shielding effect of lactate, which impedes the transfer of CO_2 to the nitrogen binding sites. These findings sheds light on the remarkable potential of MIL-101-DETA-Lac for effective SO_2 and CO_2 separation, with the choice of ILs and anions playing a pivotal role in achieving enhanced adsorption performance.

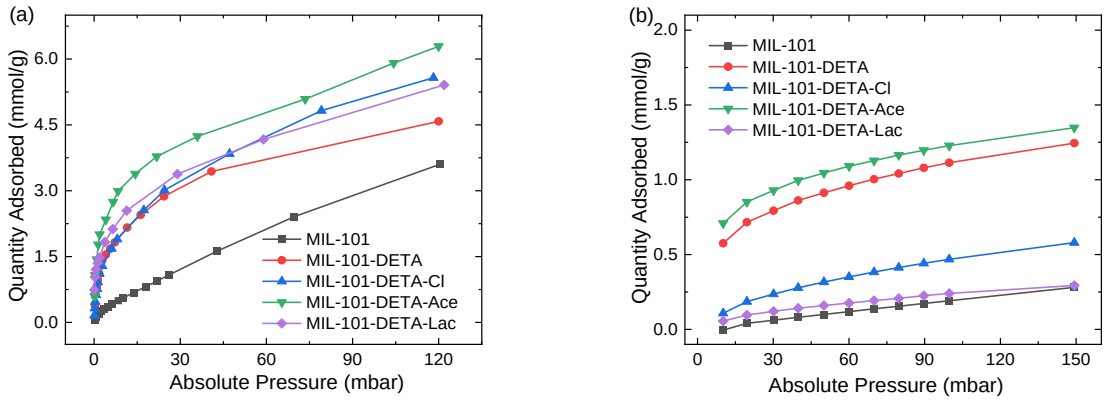

Figure 4-5: (a) SO_2 and (b) CO_2 isotherms for MIL-101 and MIL-101 composites.

IAST (Ideal Adsorbed Solution Theory) offers an effective approach for predicting the adsorption selectivity and equilibrium of gas mixtures based on the isotherms of individual components. The equation for calculating selectivity between Component 1 and Component 2 is expressed as follows:

$$S_{comp1/comp2} = \frac{y_{comp1}/x_{comp1}}{y_{comp2}/x_{comp2}}$$

where y and x represent the molar fractions of components in the adsorbed and gas phases, respectively.

To assess the selectivity of MIL-101 and its composites for SO_2 over CO_2, the IAST method was applied, employing IAST++ to fit the isotherms[32]. Figure 4-6 presents a comparison between the fitted models and the isotherm data for MIL-101 and MIL-101-DETA-Lac. The suggested models, dual-site Langmuir, exhibited correlation coefficients larger than 0.995. The IAST selectivity was evaluated at 25°C and 1000 mbar with an SO2/CO_2 ratio of 1/99, and the results are summarized in Table 4-3. All selectivity values are greater than 1, indicating a higher preference for SO_2 adsorption over CO_2 across all samples. Interestingly, MIL-101-DETA did not demonstrate significantly higher IAST selectivity for SO_2 over CO_2 compared to MIL-101. This can be attributed to the fact that the introduction of DETA benefits not only SO_2 capture but also CO_2 adsorption. However, all three DETA-based ILs modified MIL-101 exhibited relatively higher IAST selectivity, suggesting that the presence of anions enhances the material's affinity for binding SO_2 over CO_2. Remarkably, MIL-101-DETA-Lac displayed an exceptionally high IAST selectivity of 2859. Figure 4-7(a) elucidates a potential mechanism that explains how lactate impacts the material's selectivity for SO_2 over CO_2. In MIL-101-DETA-Lac, the hydroxyl group of lactate occupies the primary amine of the cation. The affinity between CO_2 and the primary amine is comparatively weaker than that between the hydroxyl group and the primary amine, leading to MIL-101-DETA-Lac not displaying an enhanced capability for CO_2 capture when compared to MIL-101. Conversely, the affinity between SO_2 and the primary amine is significantly stronger than that between the hydroxyl group and the primary amine. Consequently, a notable increase in SO_2 uptake is achieved in comparison to MIL-101. To validate this hypothesis, MIL-101-TETA-Lac was synthesized and subjected to SO_2 and CO_2 adsorption tests. Figure 4-7(b)

illustrates the structure of MIL-101-TETA-Lac, featuring three "arms" with one available for CO_2 adsorption. As per the hypothesis, MIL-101-TETA-Lac should exhibit a higher CO_2 uptake, which is indeed observed. Figure 4-7(c) presents the CO_2 isotherms of MIL-101, MIL-101-DETA-Lac, and MIL-101-TETA-Lac, clearly demonstrating a significant enhancement in CO_2 adsorption for MIL-101-TETA when compared to the other two materials. However, for SO_2 adsorption, MIL-101-TETA performs similarly to MIL-101-DETA-Lac, as depicted in Figure 4-7(d). These findings serve to verify our hypothesis.

Furthermore, it is important to note that IAST selectivity provides a qualitative analysis of a material's affinity for gases and may have some level of uncertainty. To better understand this uncertainty, the IAST selectivity was also calculated for isotherm data with a series of randomly generated errors from a normal distribution with a mean of 0 and a standard deviation of 0.05. As shown in Table 4-3, the results indicate that even a small change in the raw isotherm data can significantly impact the calculated value, particularly for samples with high IAST selectivity like MIL-101-DETA-Lac. Nonetheless, the observed trend aligns well with the isotherm data, confirming that DETA and DETA-based ILs can enhance SO_2 adsorption, and the choice of IL anions plays a crucial role in determining the selectivity.

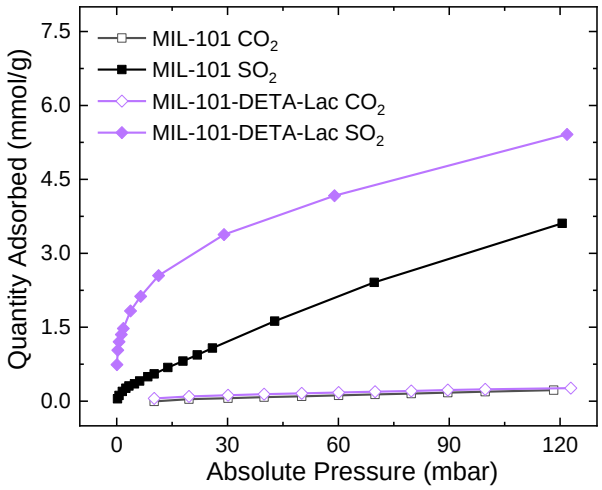

Figure 4-6: Dual-site Langmuir fitting of the SO_2 and CO_2 isotherms of MIL-101 and MIL-101-DETA-Lac.

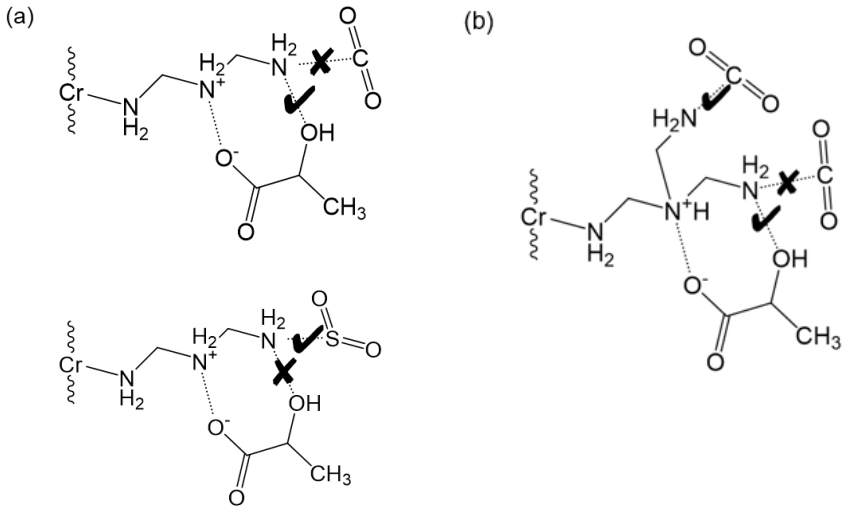

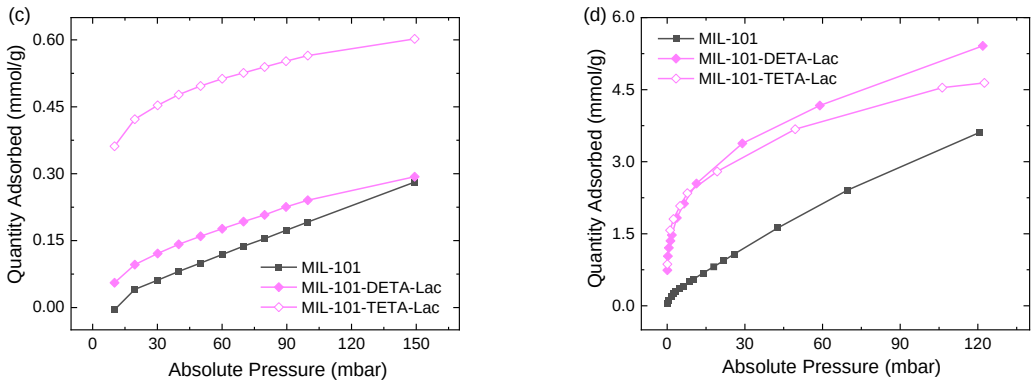

Figure 4-7: (a) Proposed interaction structure of MIL-101-DETA-Lac with CO_2 and SO_2, (b) Proposed interaction structure of MIL-101-TETA-Lac with CO_2, (c) CO_2 isotherms for MIL-101, MIL-101-DETA-Lac, and MIL-101-TETA-Lac, and (d) SO_2 isotherms for MIL-101, MIL-101-DETA-Lac, and MIL-101-TETA-Lac.

Table 4-3: The summarized calculated IAST selectivity.

Samples	Raw Data	Plus Random Error	Minus Random Error
MIL-101	32	28	30
MIL-101-DETA	43	49	39
MIL-101-DETA-Cl	155	198	168
MIL-101-DETA-Ace	125	147	125
MIL-101-DETA-Lac	2859	2132	1031

4.3.4 DRIFTS experiments

In-situ DRIFTs analysis was employed to investigate the adsorption behavior of the materials upon exposure to SO_2. Figure 4-8(a) and (b) illustrate the in-situ DRIFTs spectra of all pristine samples. In Figure 4-8(a), notable peaks emerge at 3262 and 3149 cm^{-1} for all modified MIL-101 composites compared to MIL-101, indicating the presence of primary amines through the assignment of asymmetric and symmetric stretching vibrations[33]. This confirms the inclusion of DETA or DETA-based ILs in MIL-101. Additional evidence can be observed in Figure 4-8(b), where a minor peak appeared at 1088 cm^{-1} for all modified composites, suggesting the occurrence of C-N stretching related to the introduced compounds[33]. Notably, MIL-101-DETA-Ace and MIL-101-DETA-Lac exhibit distinct bands at 921 cm^{-1}, attributed to the -COO stretching vibration of DETA-Ace and DETA-Lac anions, respectively. Moreover, the peak at 3394 cm^{-1} corresponds to the -OH stretching of lactate in DETA-Lac[34]. Moving to Figure 4-8(c) and (d), they present the in-situ DRIFTs spectra of MIL-101 and MIL-101-DETA-Lac before SO_2 exposure, during SO_2 sorption, and after reactivation, respectively. Notably, for MIL-101 (Figure 4-8(c)), significant discrepancies are observed in the DRIFTs spectra before SO_2 sorption and after reactivation, particularly at 1232, 865, and 795 cm^{-1}, suggesting an irreversible structural change and irreversible nature of SO_2 adsorption on MIL-101. Conversely, MIL-101-DETA-Lac (Figure 4-8(d)) exhibits a peak at 954 cm^{-1} after SO_2 sorption, assigned to S-O vibrational modes in chemisorbed sulfur oxide compounds[9]. Furthermore, the DRIFTs spectra for MIL-101-DETA-Lac before SO_2 exposure and after reactivation are identical, indicating the reversibility of SO_2 capture and the stability of MIL-101-DETA-Lac post-SO_2 exposure. Further investigations into stability were explored and will be discussed in the subsequent section.

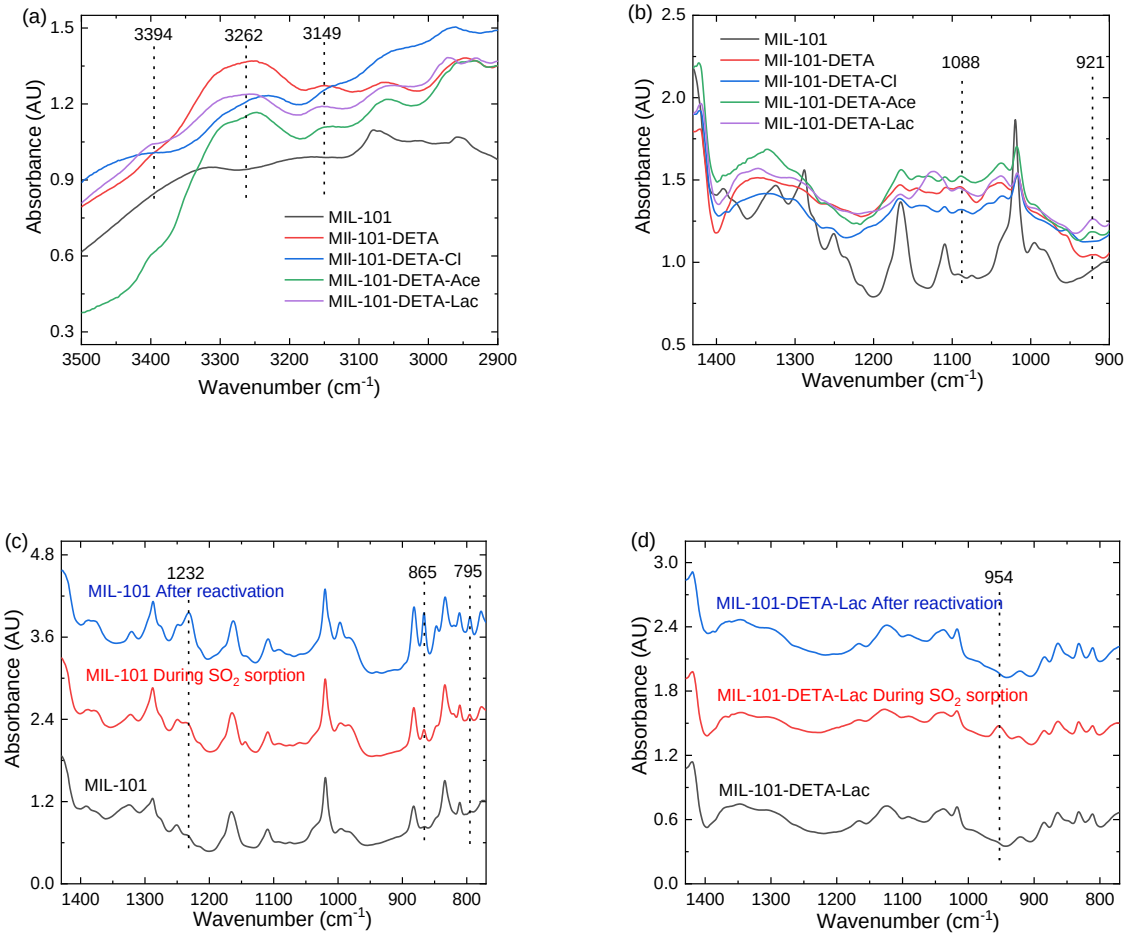

Figure 4-8: In-situ DRIFTS spectra for (a), (b) pristine MIL-101 and MIL-101 composites, (c) MIL-101 before, during SO_2 sorption, and after reactivation and (d) MIL-101-DETA-Lac before, during SO_2 sorption, and after reactivation.

4.3.5 Stability testing

SO_2 is a corrosive gas known to inflict damage on MOFs, posing a threat to their structural integrity and cyclability. In the context of flue gas desulfurization, the presence of water becomes a significant concern as well[35]. Consequently, investigating the stability of MIL-101 and MIL-101 composites in the presence of SO_2 and water is essential. Crystallinity and porosity assessments were conducted on the materials before and after SO_2 or water isotherm experiments, as depicted in Figure 4-9. The PXRD patterns presented in Figure 4-9(a) and (b) reveal that all DETA or

DETA-based ILs modified materials maintain high crystallinity after exposure to SO_2 or water, respectively, consistent with their initial states. This suggests that the crystallinity of the materials is not significantly affected by SO_2 or water exposure. However, a notable discrepancy can be observed in the post-SO_2 XRD spectra of MIL-101, indicating a loss of crystallinity, which aligns well with the DRIFTS results. N_2 adsorption experiments were conducted to assess the porosity of the materials before and after SO_2 or water isotherm experiments, and the summarized results can be found in Table 4-4. It becomes evident that all samples maintain their porosity after the water isotherm experiment. However, after exposure to SO_2, MIL-101 exhibits a considerable decrease in BET surface area as previous work reported[29], while all MIL-101 composites demonstrate robust SO_2 stability, retaining their original surface area and porosity. This can be attributed to the introduced compounds coordinating with open Cr sites, thereby protecting the framework from the detrimental effects of "invader" molecules.

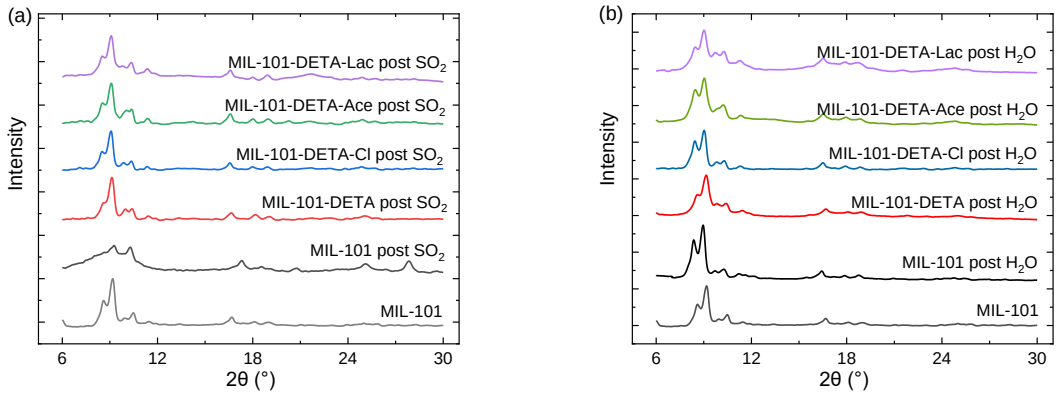

Figure 4-9: PXRD patterns of all samples (a) after SO_2 isotherm experiments, and (b) after H_2O isotherm experiments.

Table 4-4: BET surface areas of samples after different treatments.

Samples	Pristine (m^2/g)	Post SO_2 (m^2/g)	Post H_2O (m^2/g)
MIL-101	2315	1008	2313
MIL-101-DETA	1008	803	910
MIL-101-DETA-Cl	985	899	981
MIL-101-DETA-Ace	1070	958	893
MIL-101-DETA-Lac	410	365	338

4.4 Conclusions

In this chapter, MIL-101 was modified by post-introducing DETA and DETA-based ILs, which were stabilized through a covalent interaction between open Cr sites on MIL-101 and nitrogen sites on DETA or ILs. The modified MIL-101 composites exhibit higher SO_2 capacities compared to MIL-101, particularly in the low partial pressure region. This significant enhancement can be attributed to the nitrogen functional sites on DETA or DETA-based ILs, which have a high affinity for SO_2 molecules. The IAST selectivity was calculated for all samples at 1000 mbar with a SO_2/CO_2 ratio of 1/99. MIL-101-DETA demonstrates slightly higher selectivity than MIL-101, as DETA benefits both SO_2 and CO_2 capture. Moreover, all MIL-101-ILs composites displayed significantly higher selectivity than MIL-101 and MIL-101-DETA, indicating that the presence of ILs in MIL-101 composites aids in SO_2 adsorption over CO_2. Notably, MIL-101-DETA-Lac exhibited an unprecedented IAST selectivity of a thousand-fold for SO_2 over CO_2, highlighting

the influence of the anion, lactate. DRIFTS results indicate that SO_2 capture on MIL-101-ILs is reversible, whereas for MIL-101, it is not. Furthermore, the investigation of stability before and after SO_2 or water exposure reveals that the grafted ILs can protect the framework, demonstrating their potential as stable and efficient adsorbents for SO_2 capture.

4.5 References

1. Singh, S. K.; Savoy, A. W., Ionic liquids synthesis and applications: An overview. *Journal of Molecular Liquids* **2020,** *297*, 112038.

2. Zhuang, W.; Hachem, K.; Bokov, D.; Ansari, M. J.; Nakhjiri, A. T., Ionic liquids in pharmaceutical industry: A systematic review on applications and future perspectives. *Journal of Molecular Liquids* **2022,** *349*, 118145.

3. Ghandi, K., A review of ionic liquids, their limits and applications. *Green and sustainable chemistry* **2014,** *2014*.

4. Kaur, G.; Kumar, H.; Singla, M., Diverse applications of ionic liquids: A comprehensive review. *Journal of Molecular Liquids* **2022**, 118556.

5. Greer, A. J.; Jacquemin, J.; Hardacre, C., Industrial applications of ionic liquids. *Molecules* **2020,** *25* (21), 5207.

6. Wu, W.; Han, B.; Gao, H.; Liu, Z.; Jiang, T.; Huang, J., Desulfurization of flue gas: SO_2 absorption by an ionic liquid. *Angewandte Chemie International Edition* **2004,** *43* (18), 2415-2417.

7. Li, X.; Zhang, L.; Zheng, Y.; Zheng, C., Effect of SO_2 on CO_2 absorption in flue gas by ionic liquid 1-ethyl-3-methylimidazolium acetate. *Industrial & Engineering Chemistry Research* **2015,** *54* (34), 8569-8578.

8. Geng, Z.; Ma, S.; Li, Y.; Peng, C.; Jiang, B.; Liu, P.; Xu, Y., Guanidinium-based ionic liquids for high-performance SO_2 capture and efficient conversion for cyclic sulfite esters. *Industrial & Engineering Chemistry Research* **2022,** *61* (13), 4493-4503.

9. Severa, G.; Bethune, K.; Rocheleau, R.; Higgins, S., SO_2 sorption by activated carbon supported ionic liquids under simulated atmospheric conditions. *Chemical Engineering Journal* **2015,** *265*, 249-258.

10. Karousos, D.; Vangeli, O.; Athanasekou, C.; Sapalidis, A.; Kouvelos, E.; Romanos, G. E.; Kanellopoulos, N., Physically bound and chemically grafted activated carbon supported 1-hexyl-3-methylimidazolium bis (trifluoromethylsulfonyl) imide and 1-ethyl-3-

methylimidazolium acetate ionic liquid absorbents for SO_2/CO_2 gas separation. *Chemical Engineering Journal* **2016,** *306*, 146-154.

11. Lunstroot, K.; Driesen, K.; Nockemann, P.; Görller-Walrand, C.; Binnemans, K.; Bellayer, S.; Le Bideau, J.; Vioux, A., Luminescent ionogels based on europium-doped ionic liquids confined within silica-derived networks. *Chemistry of materials* **2006,** *18* (24), 5711-5715.

12. Zhao, Y.; Wang, J.; Jiang, H.; Hu, Y., Desulfurization performance of ether-functionalized imidazolium-based ionic liquids supported on porous silica gel. *Energy & Fuels* **2015,** *29* (3), 1941-1945.

13. Gao, S.; Zhang, P.; Wang, Z.; Cui, G.; Qiu, J.; Wang, J., Ionic liquid functionalized 3D mesoporous FDU-12 for effective SO_2 capture. *ACS Sustainable Chemistry & Engineering* **2019,** *8* (1), 586-593.

14. Li, X.; Zhang, L.; Zheng, Y.; Zheng, C., SO_2 absorption performance enhancement by ionic liquid supported on mesoporous molecular sieve. *Energy & Fuels* **2015,** *29* (2), 942-953.

15. Fujie, K.; Yamada, T.; Ikeda, R.; Kitagawa, H., Introduction of an ionic liquid into the micropores of a metal–organic framework and its anomalous phase behavior. *Angewandte Chemie* **2014,** *126* (42), 11484-11487.

16. Kinik, F. P.; Uzun, A.; Keskin, S., Ionic liquid/metal–organic framework composites: from synthesis to applications. *ChemSusChem* **2017,** *10* (14), 2842-2863.

17. Zhang, L.; Xiao, L.; Zhang, Y.; France, L. J.; Yu, Y.; Long, J.; Guo, D.; Li, X., Synthesis of ionic liquid-SBA-15 composite materials and their application for SO_2 capture from flue gas. *Energy & Fuels* **2018,** *32* (1), 678-687.

18. Li, J.-R.; Kuppler, R. J.; Zhou, H.-C., Selective gas adsorption and separation in metal–organic frameworks. *Chemical Society Reviews* **2009,** *38* (5), 1477-1504.

19. Li, J.; Bhatt, P. M.; Li, J.; Eddaoudi, M.; Liu, Y., Recent progress on microfine design of metal–organic frameworks: structure regulation and gas sorption and separation. *Advanced Materials* **2020,** *32* (44), 2002563.

20. Huang, Y.-B.; Liang, J.; Wang, X.-S.; Cao, R., Multifunctional metal–organic framework catalysts: synergistic catalysis and tandem reactions. *Chemical Society Reviews* **2017,** *46* (1), 126-157.

21. Dolgopolova, E. A.; Rice, A. M.; Martin, C. R.; Shustova, N. B., Photochemistry and photophysics of MOFs: steps towards MOF-based sensing enhancements. *Chemical Society Reviews* **2018,** *47* (13), 4710-4728.

22. Lázaro, I. A.; Forgan, R. S., Application of zirconium MOFs in drug delivery and biomedicine. *Coordination chemistry reviews* **2019,** *380*, 230-259.

23. Lawson, H. D.; Walton, S. P.; Chan, C., Metal–organic frameworks for drug delivery: a design perspective. *ACS applied materials & interfaces* **2021,** *13* (6), 7004-7020.

24. Kitagawa, S., Metal–organic frameworks (MOFs). *Chemical Society Reviews* **2014,** *43* (16), 5415-5418.

25. Xu, Z.; Zhao, G.; Ullah, L.; Wang, M.; Wang, A.; Zhang, Y.; Zhang, S., Acidic ionic liquid based UiO-67 type MOFs: a stable and efficient heterogeneous catalyst for esterification. *RSC advances* **2018,** *8* (18), 10009-10016.

26. Darunte, L. A.; Oetomo, A. D.; Walton, K. S.; Sholl, D. S.; Jones, C. W., Direct air capture of CO_2 using amine functionalized MIL-101 (Cr). *ACS Sustainable Chemistry & Engineering* **2016,** *4* (10), 5761-5768.

27. Walton, K. S.; Snurr, R. Q., Applicability of the BET method for determining surface areas of microporous metal− organic frameworks. *Journal of the American Chemical Society* **2007,** *129* (27), 8552-8556.

28. Lee, S.; Lee, J. H.; Kim, J., User-friendly graphical user interface software for ideal adsorbed solution theory calculations. *Korean Journal of Chemical Engineering* **2018,** *35* (1), 214-221.

29. Carter, E. A.; Hungerford, J. T.; Joshi, J. N.; DeWitt, S. J.; Jiang, X.; Marszalek, B.; Lively, R. P.; Walton, K. S., Chemical Stability of MIL-101 (Cr) upon Adsorption of SO_2 and NO_2 under Dry and Humid Conditions. *Industrial & Engineering Chemistry Research* **2023**.

30. Lin, Y.; Yan, Q.; Kong, C.; Chen, L., Polyethyleneimine incorporated metal-organic frameworks adsorbent for highly selective CO_2 capture. *Scientific reports* **2013,** *3* (1), 1859.

31. Wang, Y.; Du, K.; Chen, Y.; Li, Y.; He, X., Electrochemical determination of lead based on metal–organic framework MIL-101 (Cr) by differential pulse anodic stripping voltammetry. *Analytical Methods* **2016,** *8* (15), 3263-3269.

32. Lee, S.; Lee, J. H.; Kim, J., User-friendly graphical user interface software for ideal adsorbed solution theory calculations. *Korean Journal of Chemical Engineering* **2018,** *35*, 214-221.

33. Chen, C.; Feng, N.; Guo, Q.; Li, Z.; Li, X.; Ding, J.; Wang, L.; Wan, H.; Guan, G., Surface engineering of a chromium metal-organic framework with bifunctional ionic liquids for selective CO_2 adsorption: Synergistic effect between multiple active sites. *Journal of colloid and interface science* **2018,** *521*, 91-101.

34. Zhao, P.; Xu, F.; Chen, Y.; Huang, T.; Zhang, G., A novel durable flame retardant for cotton fabrics based on diethylenetriamine. *Polymer Degradation and Stability* **2022,** *195*, 109796.

35. Burtch, N. C.; Jasuja, H.; Walton, K. S., Water stability and adsorption in metal–organic frameworks. *Chemical reviews* **2014,** *114* (20), 10575-10612.

CHAPTER 5. NITROGEN-MODIFIED UIO-66 MOFS FOR ENHANCED SO_2 ADSORPTION: EXPERIMENTAL AND COMPUTATIONAL INVESTIGATIONS

5.1 Introduction

The functionality of ligands in metal-organic frameworks (MOFs) plays a pivotal role in shaping the properties and applications of these materials.[1-3] Ligands act as bridging entities, forming coordination bonds with metal ions or clusters, thereby determining the stability and topology of the MOF framework. Through careful selection of ligands, the pore sizes and surface areas of MOFs can be tailored, enabling specific gas sorption, separation, and catalytic processes. Ligands with diverse functional groups introduce chemical reactivity and interactions within the MOF structure, influencing host-guest interactions, selectivity, and the potential for controlled chemical transformations. Additionally, post-synthetic modifications of ligands offer opportunities to enhance the versatility of MOFs by introducing new functional groups or altering the pore environment.

The ligand functionalization of MOFs has become one of the most common and efficient approaches that can enhance MOFs properties over the parent material for adsorption-based separations.[4-9] The decorated functional sites on ligands would play a crucial role in determining the adsorptive capacity and selectivity by dictating the type of adsorbent-adsorbate interaction, and consequently the enthalpy of adsorption[1]. Amongst this field, incorporating nitrogen-based sites on MOF ligands has proven a feasible approach for achieving the desired affinity for CO_2 or water molecules at low relative pressures. For instance, higher adsorption enthalpies and uptakes at low

partial pressure regions for CO_2 adsorption have been reported for different amino decorated MOFs [10-12]. Similarly, immobilization of Lewis basic nitrogen sites into MOFs remarkably improved water uptake by strengthening water -hydrophilic nitrogen binding energy[13]. Despite numerous studies involving CO_2 and other vapors, fewer studies have examined the effects of different N sites on MOFs for SO_2 adsorption.

Herein, a series of UiO-66 type MOFs containing different N-based sites (amino, nitro, pyridine, pyrazine, and pyrazole) were synthesized and studied for SO_2 adsorption. UiO-66 was selected as parent MOF because it is constructed by hard high-valency Zr^{4+} ions with hard carboxylate-based terephthalic ligand, and has shown excellent thermal and chemical stabilities[14-15]. Aryl amine or nitrogen heterocycles with free electron donors were incorporated into UiO-66 that enabled the targeting interactions of hydrogen bonds with partial negative charged oxygen atom of SO_2 or chalcogen bonds with partial positive charged sulfur atom of SO_2[16]. Consequently, it was found that the introduced N sites enhanced the SO_2 capacities for these MOFs at various degrees due to the different levels of binding strength between N sites and adsorbed SO_2 molecules. It is important to note that the pyridine-based MOF performed the highest breakthrough capacity of 0.997 mmol/g of SO_2 and a record high IAST SO_2/CO_2 selectivity of 209. Furthermore, the influence of the chemical environment (like symmetry) of linkers on the overall adsorption behaviors of MOFs has also been revealed.

5.2 Experimental section

5.2.1 Materials

All chemicals are commercially available and were used as received. The structure of UiO-66 and the ligands used in the synthesis of nitrogen modified UiO-66 derivatives are shown in Figure 5-1.

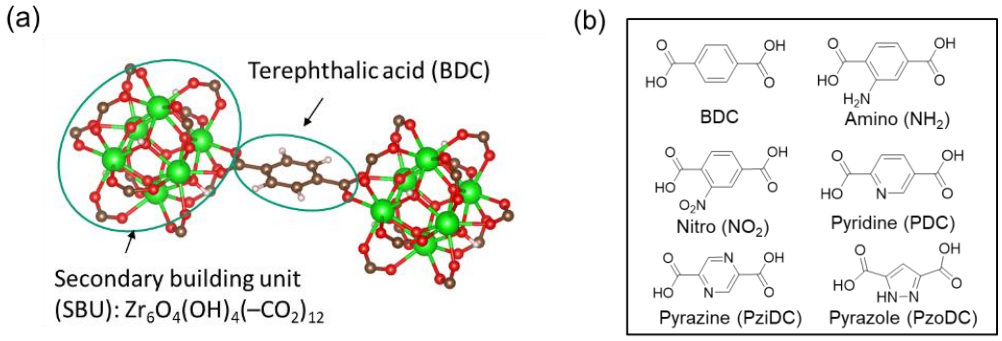

Figure 5-1: (a) Metal cluster and ligand of UiO-66, (b) Selected Ligands used in UiO-66 synthesis.

UiO-66: UiO-66 was synthesized following previously reported procedures by Cmarik et al[9]. 3.5 mmol (0.816 g) of Zirconium chloride ($ZrCl_4$) and 3.5 mmol (0.581 g) of Terephthalic acid (BDC) were dissolved by 40 mL of N,N-dimethylformamide (DMF) in a glass beaker. Then, the mixture was transferred to a 100 mL PTFE-lined autoclave with a stainless-steel casing and placed in an isotherm oven at 120 ℃ for 24 h. The product was obtained by centrifuge at 8,000 rpm and washed three times each with DMF and then acetone.

UiO-66-NH_2 and **UiO-66-NO_2**: UiO-66-NH_2 and UiO-66-NO_2 were produced following an identical procedure given above for UiO-66 synthesis replacing BDC with 2-Aminoterephthalic acid (BDC-NH_2: 3.5 mmol, 0.634 g) for UiO-66-NH_2 and 2-Nitroterephthalic acid (BDC-NO_2: 3.5 mmol, 0.7389 g) for UiO-66-NO_2.

UiO-66-2,5-PDC: UiO-66-2,5-PDC was prepared following a previous work reported by Reinsch H, et al[17]. 4.4 mmol (1.434 g) Zirconyl chloride octahydrate ($ZrOCl_2 \cdot 8H_2O$) and 4.4 mmol (0.733 g) of 2,5-Pyridinedicarboxylic acid (2,5-PDC) were dissolved in 45 ml formic acid and 5 mL water in a round bottom flask. Then, the flask was placed in an oil bath, heated at 120 ℃ for 3 h and refluxed under stirring. The solid product was separated by centrifugation and washed with water and ethanol three times each.

UiO-66-2,5-PziDC: UiO-66-2,5-PziDC was prepared by modifying a previous work reported by Barkhordarian et al[18]. 0.5 mmol (0.116 g) of $ZrCl_4$ was dispersed into 5 mL of DMF in a glass beaker, sonicated for 5 minutes followed by adding a 5 mL of concentrated (10.2 M) HCl solution. Then, the mixture was placed in a fume hood at room temperature for 2 h. Afterwards, 0.5 mmol (0.084 g) of 2,5-Pyrazinedicarboxylic acid (2,5-PziDC) was added to the mixture. The mixture was sonicated for 5 minutes to dissolve the 2,5-PziDC. The reactant solution was placed in a 23 mL PTFE-lined autoclave with a stainless-steel casing and heated at 80 ℃ for 40 h. The solid product was separated and washed with DMF and the acetone three times each.

UiO-66-3,5-PzoDC: UiO-66-3,5-PzoDC was synthesized according to the literature reported by Jacobsen et al.[19] 0.32 mmol (0.0557 g) of 3,5-Pyrazoledicarboxylic acid (3,5-PzoDC) was first dissolved in 0.8 mL of DMF in a glass reactor. Then, 0.302 mL of formic acid was added to the solution. Thereafter, 0.4 mL of Zirconium(IV) oxynitrate hydrate ($ZrO(NO_3)_2 \cdot H_2O$) aqueous solutions of 0.533 mol/L was introduced. Finally, the glass reactor was placed in an oil bath and heated at 100 ℃ for 15 minutes under stirring at 650 rpm. The product was centrifuged and washed three times each with DMF and then acetone.

5.2.2 Characterization and measurements

PXRD and BET surface areas: PXRD (Powder X-ray diffraction) patterns of the synthesized UiO-66 and CAU-10 derivatives were collected using an XPert PRO Alpha-1 diffraction system with Cu Kα radiation (λ = 1.542 Å) under ambient conditions with 2θ ranging from 2 to 30°. The data were recorded continuously with a step size of 0.0167° per second. Surface areas were calculated from N_2 physisorption measurements at 77 K and calculated via the Brunauer, Emmett, and Teller (BET) model using a pressure range of $0.005 < P/P_0 < 0.03$[20]. All samples were first activated at 150 ℃ for 15 h before adsorption measurements.

Breakthrough measurements: Breakthrough experiments were performed using a fixed-bed adsorption system to mimic the dynamic industrial gas separation process. 50 mg sample was packed in a fritted gas tube with a bed height of 1 cm, then the tube was placed into the home-built breakthrough system (SI Figure). Prior to any SO_2 breakthrough experiments, MOF samples were fully activated by a flow of dry nitrogen at 20 mL/min under 120 ℃ for 12 h. SO_2 breakthrough measurements were conducted at 25 ℃ with a gas mixture of 0.1% SO_2/balanced N_2. SO_2 concentration in inlet and outlet was detected by a California Analytical Instruments detector (600SC FTIR).

SO_2 and CO_2 adsorption isotherms: SO_2 and CO_2 adsorption isotherms were obtained using a home-built pressure decay system and a Micromeritics 3Flex Surface Characterization Analyzer with ultrapure grade SO_2 or CO_2, respectively. Both were carried out with controlled changes of partial pressures in the sample chamber or tube under a constant temperature. SO_2 and CO_2 isotherms were recorded at 25 ℃ and all samples were activated at 150 ℃ for 15 h under vacuum prior to the measurements. Scheme of the homebuilt pressure decay system can be found

in the SI. Ideal Adsorbed Solution Theory (IAST) calculation were conducted through IAST++ interface[21].

ATR-IR measurements: ATR-IR spectra were collected with a resolution of 4 cm^{-1} using a Thermo Scientific Nicolet iS10 FTIR equipped with a Smart iTX accessory.

Computational methods (Note: Dr. Kai Cui, my collaborator from the University of Wisconsin-Madison did these simulation work.)

(1) Adsorption calculation: Dispersion corrected density functional theory (PBE-D3[22-23]) was used to calculate the binding energies of SO_2 in four of the "SO_2 stable" MOFs: parent UiO-66, UiO-66-NH_2, UiO-66-2,5-PDC and UiO-66-2,5-PziDC. All calculations were performed in VASP[24-25] using a plane wave basis set with a 600 eV energy cutoff. Geometries of the bare adsorbents were first optimized. Both the lattice constant and atomic positions were relaxed until the forces on atoms were less than 0.05 eV/Å. SO_2 adsorbate was then added into the unit cell of MOFs at different sites. The geometries of these adsorbed complexes were optimized using the same methods but with lattice constant fixed. The binding energy is calculated as

$$\Delta E_{\text{bind}} = E_{\text{complex}} - E_{\text{MOF}} - E_{\text{SO}_2}$$

Beyond the binding energies, a multisite Langmuir model[26-28] was used to calculate the isotherm and the adsorption free energy at both PBE-D3 and local MP2 (LMP2)[29] (via a QM/QM approach[30]) level. The binding free energy ΔG_s of SO_2 on each site s in the MOF were first calculated as:

$$\Delta G_{\text{s}} = \Delta E_s + \Delta E_{\text{ZPE}} - T\Delta S_{\text{trans-rot}} - RT$$

where ΔE_s is the binding energy on site s, ΔE_{ZPE} is the zero-point energy change and $\Delta S_{\mathrm{trans-rot}}$ is the loss of translational and rotational entropy of SO_2 upon binding. The standard adsorption free energy is then calculated from the model via:

$$\Delta G_{ad}^{\ominus} = -k_B T \ln\left[\frac{p^{\ominus}}{c^{\ominus}} \sum_s c_s \exp(-\beta \Delta G_s)\right]$$

c_s is the concentration of site kind s in the MOF. More details can be found in the SI.

(2) Cluster calculation: A cluster models to decompose the short-range and long-range interactions was built. Clusters were carved from the optimized periodic structure with no further optimization. The cluster model contains the $Zr_6O_4(OH)_4(COO)_{12}$ SBU and three explicit BDC (or modified BDC) linkers that were closest to the adsorbates. The other nine linkers that also coordinate to the metal cluster were replaced by $HCOO^-$ groups. Hydrogen atoms were added to the dangling COO^- group in the explicitly modeled linkers to ensure the neutrality of the cluster and avoid any artifacts due to charged systems[30]. The structure of this cluster model (denoted as ML_3) can be found in the SI. SO_2 binding strengths on the N sites in UiO-66-2,5-PDC and UiO-66-2,5-PziDC were recalculated using the cluster model using periodic DFT with the same set up as in previous section. The box length of the cell was set to 30 Å.

(3) Natural bond orbital analysis: Natural bond orbital (NBO) analysis for the gas phase SO_2-linker associates at PBE level[31] with 6-31G(d) basis sets[32] in Gaussian 16[33] was performed. The stabilization energies $E^{(2)}$ between the lone pair electrons of the N atom in the linker to the Rydberg orbitals (unoccupied orbitals) of the S atom were calculated which describe the interaction strength due to the electron delocalization between a donor (N) and an acceptor (S) orbital pair.

5.3 Results and discussion

5.3.1 Crystallinity and porosity of materials

Six UiO-66 type MOF materials were synthesized using zirconium salts with the bi-carboxyl type ligands featuring varying nitrogen sites. The crystal structures of parent UiO-66 and its N-modified derivatives were confirmed through PXRD measurements. As shown in Figure 5-2(a), the PXRD patterns obtained for the MOF samples confirm that all the MOFs were successfully synthesized with high crystallinity. The characteristic reflections of UiO-66 at 7.4° and 8.5° which are attributed to its (111) and (200) crystal planes[34] are consistent with the simulated pattern of UiO-66, indicating that all the MOFs possess the same structure as UiO-66. Slight differences in patterns may be due to different unit cell parameters resulting from the slight structural differences of the ligands.

The BET surface areas were determined via N_2 physisorption isotherms experiments at 77 K, and the results are presented in Figure 5-2(b). The relatively high surface areas are in good agreement with literature values and suggest that these MOFs are promising candidates for gas adsorption applications. In comparison with parent UiO-66, the introduction of amino, pyridine, or pyrazine shows little impact on the surface area with respect to the parent MOF. UiO-66-NO_2 exhibits a lower surface area of 821 m^2/g than UiO-66-NH_2 due to the two larger O atoms on the ligands. UiO-66-3,5-PzoDC was calculated to have the lowest surface area among all the five UiO-66 derivatives, which may be attributed to its limited crystallinity and stability. Compared to the terephthalate-based framework, the titled secondary building units (SBU) in UiO-66-3,5-PzoDC are distorted to remedy the bent ligand (an angle between carboxylate groups: 147.4°) to form fcu topology[19].

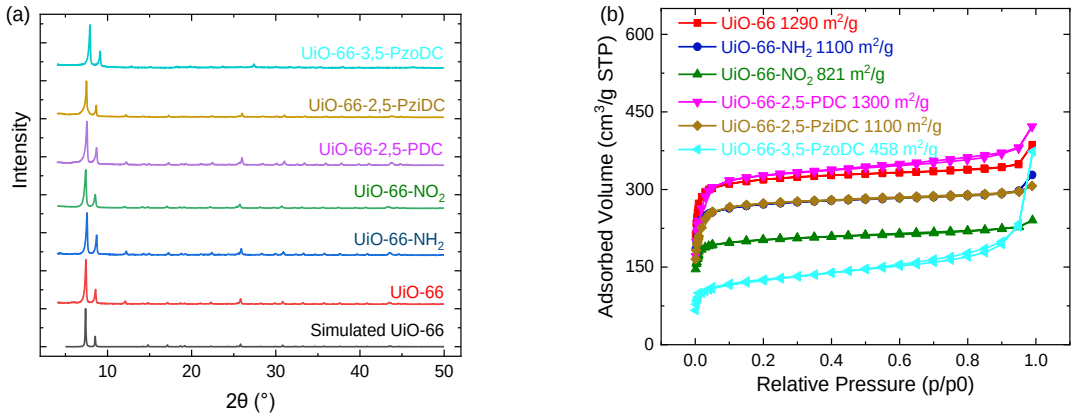

Figure 5-2: (a) PXRD patterns and (b) BET surface areas for UiO-66 type MOFs.

5.3.2 SO_2 Breakthrough Performance

To investigate the feasibility of MOF samples for the separation of SO_2/N_2 under dynamic conditions, breakthrough measurements were conducted with a gas mixture of 0.1%(1000 ppm) SO_2/balanced N_2 at 298 K and a flow rate of 20 mL/min. As presented in Figure 5-3(a), SO_2 breaks through much earlier for UiO-66-NO_2 than that of parent UiO-66 which demonstrates that nitro performed a negative impact on adsorption property for SO_2 capture. Clear enhancements in breakthrough capacity of SO_2 are observed for all the other N modified UiO-66 MOFs as summarized in Figure 5-3(b) with a rank of UiO-66 (0.137 mmol/g) < UiO-66-3,5-PzoDC (0.331 mmol/g) < UiO-66-NH_2 (0.374 mmol/g) < UiO-66-2,5-PziDC (0.503 mmol/g) < UiO-2,5-PDC (0.997 mmol/g). Since the only main difference between parent UiO-66 and amino, pyridine, and pyrazine modified UiO-66 MOFs is the presence of different N sites, the great increase in loadings can be attributed to the interaction between N sites with SO_2 molecules. For UiO-66-3,5-PzoDC, the increase may result from a synergistic effect of functional groups and surface areas. Notably, adsorption capacity does not positively correlate with materials' surface area under dynamic conditions in this work. Unexpectedly, UiO-66-2,5-PziDC possessing two N sites on its ligands

practices a lower loading of SO_2 than UiO-66-2,5-PDC which has only one N site on its ligands. Computational analyses reveal that this is likely due to N sites in symmetrical positions leading to reduced electron density on both (vide infra).

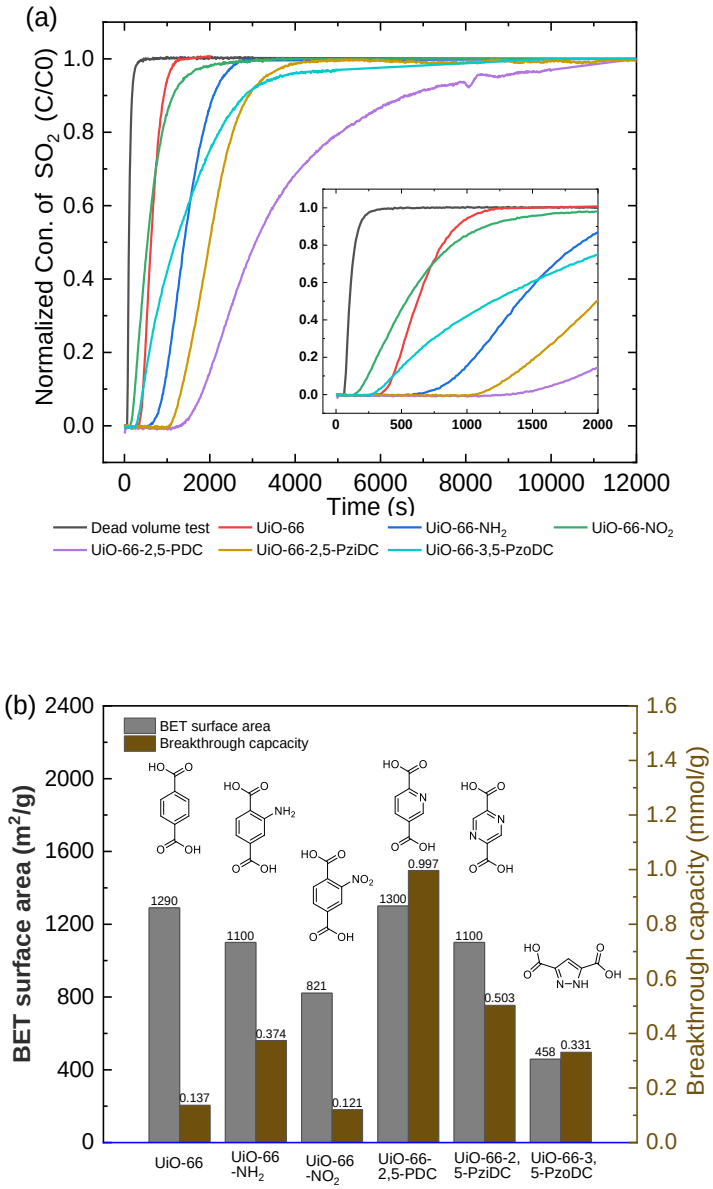

Figure 5-3: (a) SO_2 breakthrough curves and (b) Comparison of breakthrough capacity with BET surface areas for UiO-66 type MOFs.

5.3.3 Stability toward SO_2

As mentioned in the introduction, stability can be a large obstacle for use of MOFs in many fields including applications for acid gas separation and sequestration. To evaluate the stability of the MOFs in this work, PXRD patterns of MOF samples before and after SO_2 exposure (100 % SO_2 at 25 ℃ for 24 h) were collected (See Figure 5-4). Except for UiO-66-3,5-PzoDC, all the other MOFs maintain their patterns after SO_2 exposure, confirming stability in the presence of SO_2. As for UiO-66-3,5-PzoDC, decreasing peak intensities were observed, and in addition the typical UiO-66 peaks at 2θ positions of about 7.0° and 8.3° became broad, indicating the loss of crystallinity of UiO-66-3,5-PzoDC. BET surface area measurements provide further insight into the structural integrity of these materials. UiO-66-3,5-PzoDC displays a significant loss of its porosity. As shown in Table 5-1, UiO-66-3,5-PzoDC retained only 22.9 % of its original surface area after pure SO_2 exposure. While for all the other MOF samples, they maintain more than 90 % of their porosities, evidencing their impressive SO_2 stability.

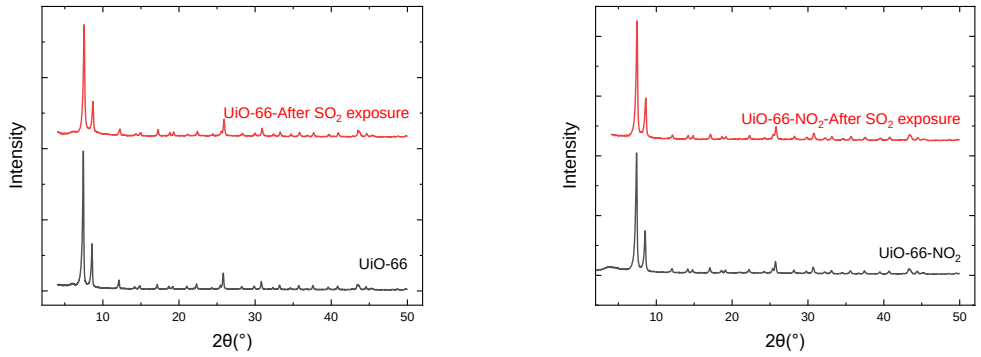

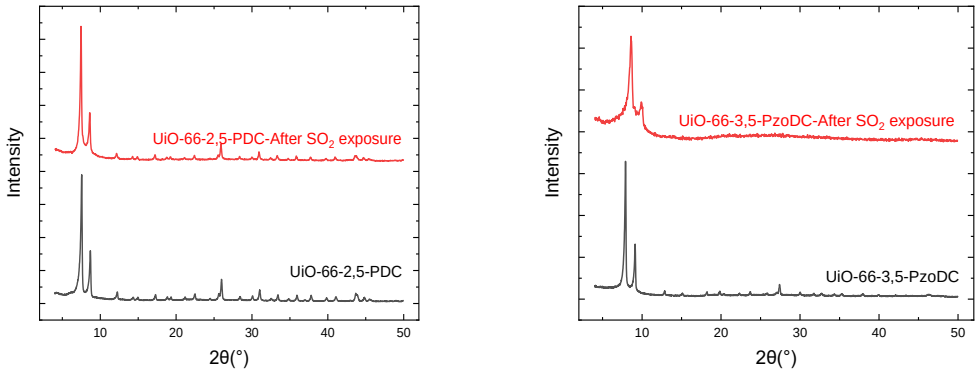

Figure 5-4: PXRD patterns of UiO-66 MOFs before and after SO_2 exposure.

Table 5-1: Surface areas of UiO-66 MOFs under SO_2 exposure.

MOFs	BET surface areas (m^2/g)		Surface area retained
	Before SO_2 exposure	After SO_2 exposure	
UiO-66	1290	1263	97.9 %
UiO-66-NH_2	1100	1030	93.6 %
UiO-66-NO_2	821	751	91.5 %
UiO-66-2,5-PDC	1300	1197	92.1 %
UiO-66-2,5-PziDC	1100	997	90.6 %
UiO-66-3,5-PzoDC	458	105	22.9 %

Considering the required high capacity of SO_2 and harsh processing conditions of practical applications, we removed UiO-66-NO_2 and UiO-66-3,5-PzoDC for further investigation in this work. However, the above analysis is also suggest that a high surface area and stable MOF with pyrazole ligand may be a good candidate for SO_2 capture, such as MOF-303[35].

5.3.4 SO_2 adsorption and IAST selectivity

SO_2 isotherms were recorded for activated samples of all four stable UiO-66 MOFs (parent UiO-66, UiO-66-NH_2, UiO-2,5-PDC, and UiO-66-2,5-PziDC) at 25 ℃ from 0 to 1000 mbar. All four isotherms increase rapidly from 0 to 50 mbar then proceed to a gradual increase in capacity to 1000 mbar and present typical type-I isotherm profiles (See Figure 5-5), suggesting favorable interactions between MOF materials with SO_2. The highest SO_2 loading approaches 10.5 mmol/g for UiO-66-2,5-PDC at 1000 mbar. However, all three N-modified UiO-66 MOFs show no significant increase in loading compared to parent UiO-66. This may be because the loadings of SO_2 for all MOF samples in this region (around 1000 mbar) highly depend on the surface areas. However, at low pressures, apparent enhancements of SO_2 capture are observed for all N modified UiO-66 MOFs. Impressively, UiO-66-2,5-PDC shows almost 5 times higher uptake (3 mmol/g) than that of parent UiO-66 (0.5 mmol/g) at 5 mbar. This further proves the positive effect of N sites for SO_2 adsorption.

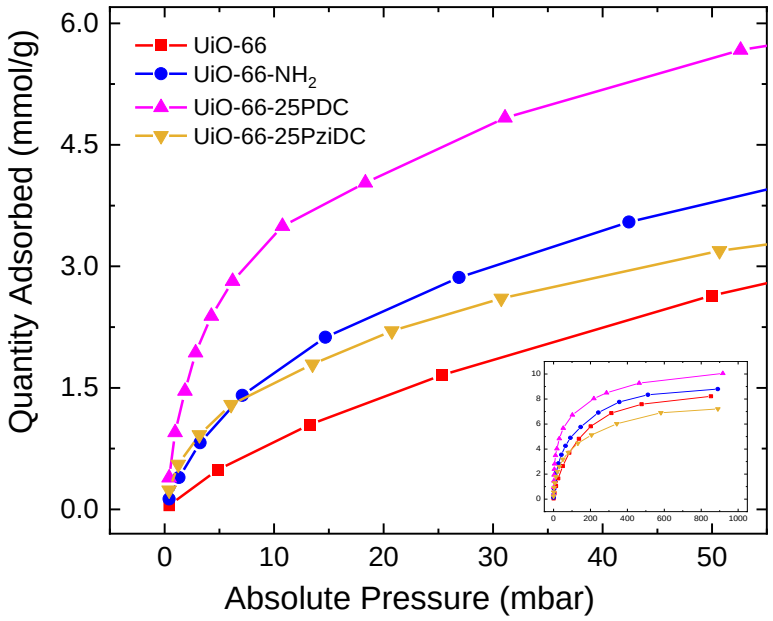

Figure 5-5: SO_2 isotherms for four "SO_2 stable" samples.

CO_2 is a common component in flue gas, and it is a big competitor for SO_2 adsorption since SO_2 and CO_2 have some similarities in structure and properties[36-37]. Therefore, evaluating the selective capabilities of adsorbents for SO_2 over CO_2 is vital. CO_2 isotherm experiments were carried out for UiO-66 MOFs, and the results are shown in Figure 5-6. We find that SO_2 capacities for all MOF samples are remarkably higher than their CO_2 uptakes. Ideal adsorbed solution theory (IAST) selectivity was calculated on a 1% SO_2/ 99% CO_2 mixture, an approximate ratio of SO_2 to CO_2 in real flue gas, and the results were summarized in Table 5-2. All selectivity values are much larger than one, suggesting the high affinity between MOF samples with SO_2. Notably, UiO-66-2,5-PDC showed a selectivity of 209, almost three times higher than that of parent UiO-66 (49), which could be attributed to the strong interaction between pyridine-Ns of high polarity with SO_2 of high dipole moment.

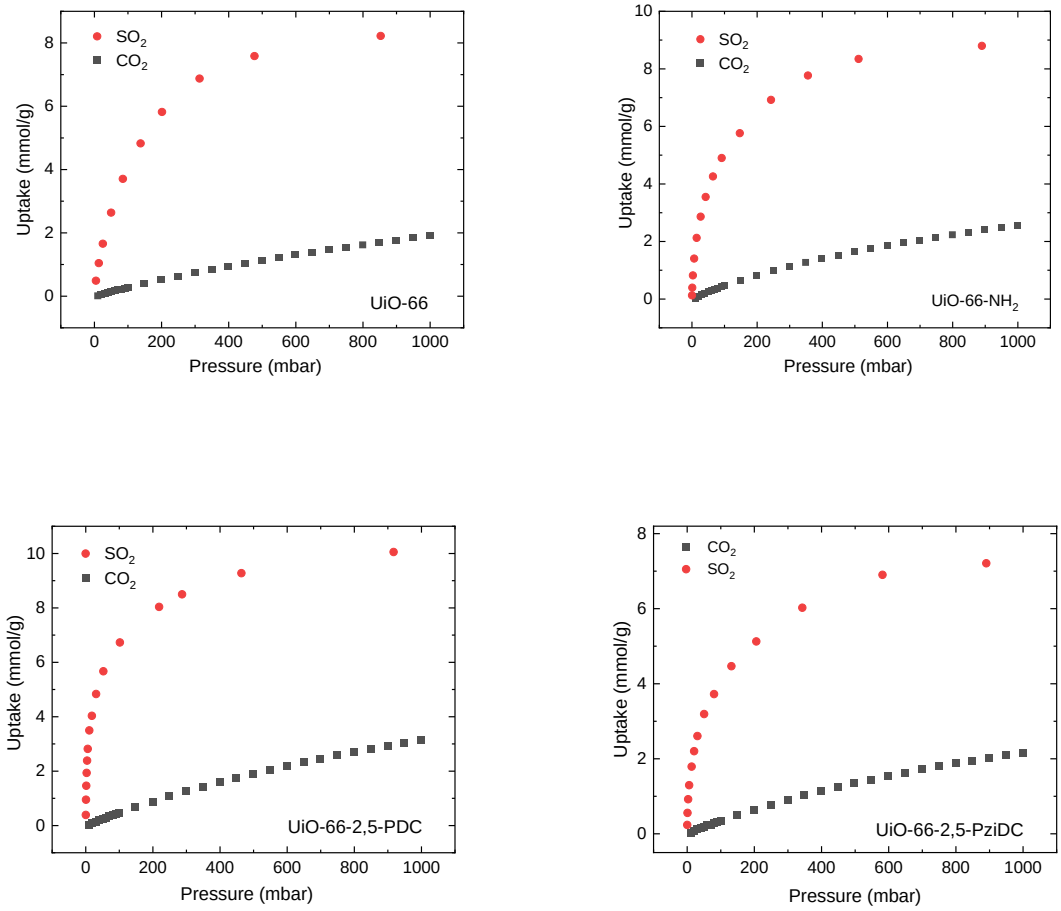

Figure 5-6: SO_2 and CO_2 isotherms for four "SO_2 stable" samples.

Table 5-2: Calculated IAST selectivity.

MOFs	IAST Selectivity
UiO-66	48
UiO-66-NH_2	59
UiO-66-2,5-PDC	209

5.3.5 ATR-IR spectroscopic characterization

ATR-IR spectra were collected to validate the interaction between introduced N sites and adsorbed SO_2 molecules. As shown in Figure 5-7, the frequency bands at the range of 650-680 cm^{-1} were attributed to μ_3-O stretching vibrations of the secondary building unit $Zr_6O_4(OH)_4(-CO_2)_{12}$ in the UiO-66 frameworks, and the characteristic asymmetric and symmetric stretching vibrations of ν(-OCO-) in UiO-66 type MOFs were observed for all MOF samples at 1595-1658 cm^{-1} and 1384-1404 cm^{-1}, respectively.[38-39] After SO_2 exposure, combination bands were observed at about 980 cm^{-1} for all MOF samples, which could be due to the S=O symmetric stretches of physiosorbed SO_2 species.[40-41] Besides, a strong peak appeared at about 1142 cm^{-1} for all N-modified UiO-66 MOFs, indicating the presence of more strongly bounded SO_2 species. That may result from the interaction between decorated nitrogen functional groups with adsorbed SO_2 molecules. Evidence (See Figures in Appendix C) could be that the bands at 3376 cm^{-1} and 3460 cm^{-1} signified as N-H_2 stretches for UiO-66-NH_2 were reduced, suggesting that the -NH_2 group was active for SO_2 adsorption[42]. Unfortunately, the N-S interaction was not caught by ATR-FTIR. However, the nitrogen sites with lone pairs of electrons on MOFs could work as Lewis base sites to interact with the electrophilic sulfur atom of SO_2 to form chalcogen bonds[43-44], which was evidenced by computational modeling.

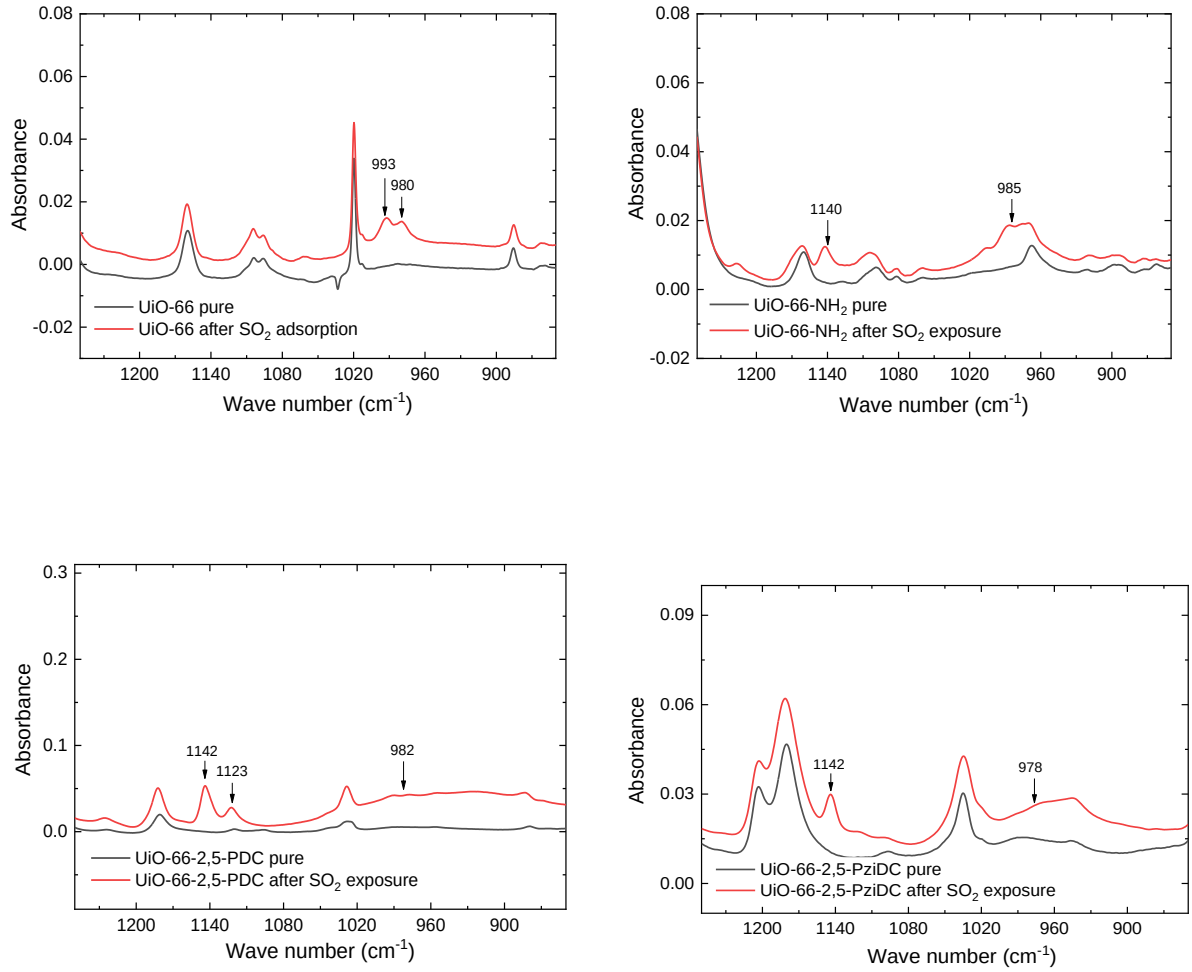

Figure 5-7: ATR-IR spectra of SO_2 adsorption into four "SO_2 stable" samples.

3.3.4 SO_2 binding energy in N-modified UiO-66

In addition to these experimental investigations, computational modeling is another powerful tool to gain an understanding of the molecular interaction between SO_2 and the MOFs. Here periodic DFT was used to calculate the binding energy of SO_2 in four of the synthesized MOFs: parent UiO-66, UiO-66-NH_2, UiO-66-2,5-PDC and UiO-66-2,5-PziDC. Based on the optimized structures, four potential binding sites were identified for binding SO_2, namely the μ_3-

OH site, μ_3-O site, benzene (or pyridine/pyrazine) ring and the N atom, as shown in Figure 5-8(a). The calculated binding energies on these sites were shown in Figure 5-8(b).

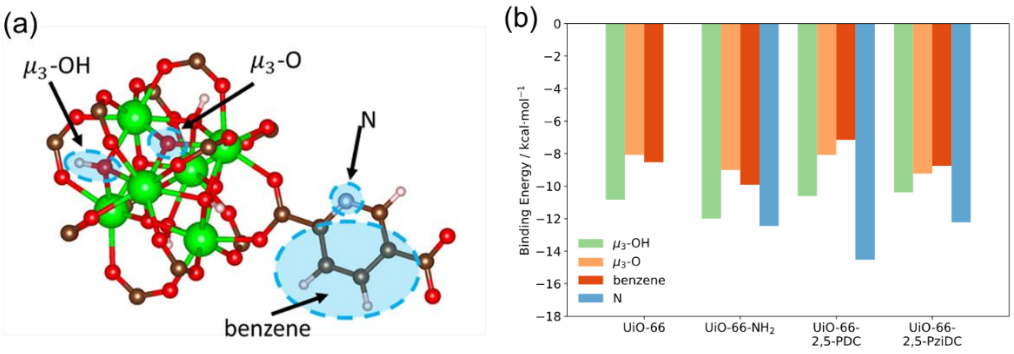

Figure 5-8: (a) Four possible binding sites: μ3-OH site, μ3-O site, benzene and N sites. Colors: oxygen (red), carbon (brown), nitrogen (grey), sulfur (yellow), zirconium (green), and hydrogen (light pink). (b) Binding energy of SO2 on the four binding sites on the parent and N-modified UiO-66 MOFs.

In the unmodified UiO-66, μ_3-OH was the most favorable site for SO_2 to bind to, with a binding energy of -10.8 kcal/mol. N-modification did not change the binding strength on the non-nitrogen sites. The increased binding strength on the OH site observed in UiO-66-NH_2 was likely from the long-range dispersion interaction due to the increased density of the framework with NH_2 functionalization. For all three N-modified MOFs, the N site had the strongest binding energy among all four binding sites, ranging from -12.2 to -14.5 kcal/mol. The relative order of the binding strength on the N sites in the three MOFs showed apparent accordance with their experimental SO_2 adsorption capacity order: SO_2 binds most strongly in UiO-66-2,5-PDC, which showed the largest capacity. The binding strengths in UiO-66-2,5-PziDC and UiO-66-2,5-NH_2 were similar, and their capacities were also similar.

The adsorption free energy was further estimated using these binding energy data. Here the multisite Langmuir model[26-28] was applied to calculate the adsorption free energy of SO_2 from first

principles, as shown in Table 5-3. It was found that the computational model provided excellent agreement with the experimental results (obtained by fitting the measured isotherm to a dual-site Langmuir equation) in the absolute adsorption free energy with errors less than 1 kcal/mol. When a higher level of theory (LMP2) was used, quantitative prediction of the $\Delta G_{ad}^{\ominus}$ could be achieved for some of the MOFs with errors about 0.2 kcal/mol (see SI). Our calculation showed that all three N-modified MOFs have more negative adsorption free energy than the parent. UiO-66-2,5-PDC had the most negative $\Delta G_{ad}^{\ominus}$ and thus the largest capacity. These binding energy and adsorption free energy data concluded that the modification of the linkers introduces strong-binding N sites but had negligible influence on the binding at other sites. The enhanced SO_2 adsorption capacity after modification was indeed due to addition of the N sites.

Table 5-3: Calculated adsorption free energy $\Delta G_{ad}^{\ominus}$ (in kcal/mol) via Langmuir model at PBE-D3 level for the parent and N-modified UiO-66 MOFs.

System	Experiment	PBE-D3
UiO-66	-2.5	-3.2
UiO-66-NH_2	-3.5	-3.9
UiO-66-2,5-PDC	-4.2	-3.9
UiO-66-2,5-PziDC	-3.7	-3.5

5.3.6 Pyridine-N vs. pyrazine-N

As we discussed in the previous sections, UiO-66-2,5-PziDC has twice as many N sites as compared to UiO-66-2,5-PDC, but a lower adsorption capacity. This observation is apparently explained by the binding energy calculation: though there are more N sites in UiO-66-2,5-PziDC, the binding strength on each site is much smaller ($\Delta\Delta E_{bind}$ = 2.3 kcal/mol) than in UiO-66-2,5-PDC. We performed energy decomposition analysis to seek the origins of this difference in the binding energies. By contrasting the results obtained using cluster models and periodic models, the short-range and long-range interactions could be decomposed; by performing calculations with and without the D3 correction, the electrostatic interaction and dispersion interaction could be separated as well. The results were summarized in Table 5-4. For the calculations in the entire unit cell, $\Delta\Delta E_{bind}$ was almost the same with and without the dispersion correction, which indicated that the $\Delta\Delta E_{bind}$ between UiO-66-2,5-PDC and UiO-66-2,5-PziDC does not primarily arise from long-range dispersion interactions. When a cluster model (either the ML_3 cluster or only a linker) was used, $\Delta\Delta E_{bind}$ decreased to 0.4 kcal/mol and the exclusion of dispersion interaction still mode no difference. Therefore, the majority of the $\Delta\Delta E_{bind}$ (1.9 kcal/mol) can be attributed to the long-range electrostatic interaction. Specifically, the 2,5-PDC linker had a permanent dipole moment, and the arrangement of the linkers in the framework can generate electrostatic fields to attract the polar SO_2 molecule from a long range. Such electrostatic field was absent in the UiO-66-2,5-PziDC case due to the zero-dipole moment of the linker.

Table 5-4: Binding energies (in eV) of SO_2 on the N sites in UiO-66-2,5-PDC and UiO-66-2,5-PziDC recalculated using periodic and cluster models. Numbers in parentheses are calculated using the same setup but exclude the D3 dispersion correction.

System	Unit cell	ML3 cluster	Linker only
UiO-66-2,5-PDC	-14.5 (-8.1)	-12.2 (-7.1)	-9.5
UiO-66-2,5-PziDC	-12.2 (-6.0)	-11.8 (-7.7)	-9.0
$\boldsymbol{\Delta\Delta E_{bind}}$	2.3 (2.1)	0.4 (0.4)	0.5

The remaining 0.02 eV in $\Delta\Delta E_{bind}$ was consequently from the short-range electrostatic interactions. We then performed NBO analysis to characterize these short-ranged interactions. All NBO analysis was done on gas phase SO_2-linker dimer complexes. The geometries of these gas phase complexes were found to be very similar to those in the MOF environment. For example, the N-S distance is 2.654 Å in the gas phase 2,5-PDC-SO_2 system and is 2.610 Å in UiO-66-2,5-PDC-SO_2 system.

In NBO analysis, the interaction strength due to the electron delocalization between a donor (N) and an acceptor (S) orbital pair was characterized by the stabilization energies $E^{(2)}$. Larger value of $E^{(2)}$ indicated stronger interaction[45]. Here we focused on the interaction between the lone pair electron orbital of the N atom in the linker and the Rydberg orbitals (unoccupied orbitals) of the S. Illustrations of these orbitals were shown in Figure 5-9. The calculated $E^{(2)}$ for three donor-acceptor pairs were listed in Table 5. Clearly, $E^{(2)}$ was systematically larger in 2,5-PDC-SO_2 system than in 2,5-PziDC-SO_2, indicating that the donor-acceptor interaction between the linker

N atom and the adsorbate S atom was slightly stronger in the 2,5-PDC case. This observation agrees with the calculated natural charge on the N atoms of the two linkers: N atom in 2,5-PDC has more negative charge (-0.4213) than that in 2,5-PziDC (-0.3815). The weaker short-range interaction in UiO-66-2,5-PziDC was likely also due to the symmetric distribution of the two N atoms, which leads to a less concentrated electron density on each N site.

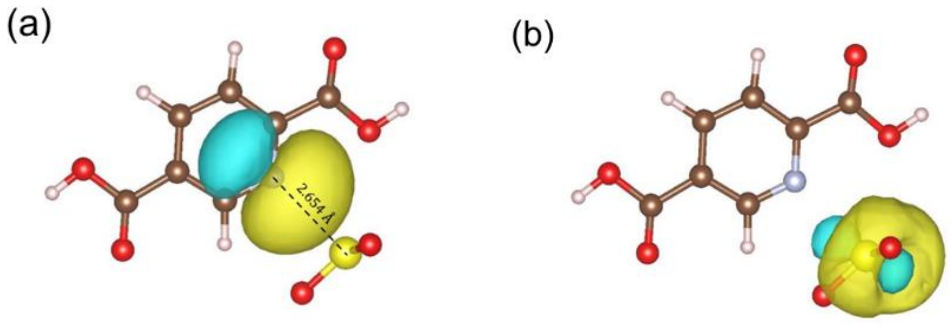

Figure 5-9: Illustration of the NBOs in in 2,5-PDC-SO_2 complex. (a) the lone pair orbital of N atom (LP-N) and (b) one of the unoccupied Rydberg orbitals of S atom (RY*-S), which corresponds to the first column in Table 5-5.

Table 5-5: Stabilization energies $E^{(2)}$ between the lone pair electrons of the N atom (LP-N) in the linker to three Rydberg orbitals of the S (RY*-S) atom in the SO_2.

System	$E^{(2)}$(LP-N→RY*-S) / kcal mol^{-1}		
2,5-PDC-SO_2	0.42	0.14	0.06
2,5-PziDC-SO_2	0.33	0.13	0.05

5.4 Conclusions

The kinetic adsorption of SO_2 for all the MOF samples indicated its affinity for these materials follows order: UiO-66-2,5-PDC > UiO-66-2,5-PziDC > UiO-66-NH_2 > UiO-66-3,5-PzoDC > UiO-66 > UiO-66-NO_2 (pyridine > pyrazine > amino > pyrazole > pure > nitro). The SO_2 capture on UiO-66-2,5-PDC (0.997 mmol/g) showed a 6.6-fold enhancement compared to parent UiO-66 (0.13 mmol/g). On the other hand, UiO-66-2,5-PDC displayed an unprecedented selectivity of SO_2/CO_2 (209: calculated by IAST++ with 1%SO_2/99%CO_2) under ambient conditions. ATR-FTIR results evidenced the interactions between nitrogen sites on MOFs with adsorbed SO_2 molecules.

The SO_2 adsorption behavior in the parent and three N-modified UiO-66 type MOFs have also been computationally investigated. The binding energies of SO_2 at four possible sites were calculated via periodic DFT. It was found that the newly added N sites through modification were the strongest binding sites. Meanwhile, the modification had negligible influence on the binding strength on other sites. Therefore, the enhanced SO_2 adsorption capacity was directly contributed by the presence of N sites. By closely comparing the binding of SO_2 to the N sites in UiO-66-2,5-PDC and UiO-66-2,5-PziDC, the symmetric distribution of the two N atoms in the 2,5-PziDC resulted in less concentrated electron density on each N site and thus weaker donor-acceptor interaction between the N site and the SO_2. This symmetry of 2,5-PziDC also leads to a zero-dipole moment, which eliminates any long-range electrostatic attraction to the polar SO_2 adsorbates. Consequently, the binding strength of SO_2 to the pyrazine was much weaker than that to the pyridine, and the adsorption capacity of SO_2 in UiO-66-2,5-PziDC was lower than UiO-66-2,5-PDC, despite its larger number of N sites. Our results highlight the influence of chemical environment of MOFs on their adsorption capacities.

5.5 References

1. Kazemi, S.; Safarifard, V., Carbon dioxide capture in MOFs: The effect of ligand functionalization. *Polyhedron* **2018,** *154*, 236-251.

2. Hao, J.; Xu, X.; Fei, H.; Li, L.; Yan, B., Functionalization of metal–organic frameworks for photoactive materials. *Advanced Materials* **2018,** *30* (17), 1705634.

3. Fliedel, C.; Ghisolfi, A.; Braunstein, P., Functional short-bite ligands: synthesis, coordination chemistry, and applications of N-functionalized bis (diaryl/dialkylphosphino) amine-type ligands. *Chemical Reviews* **2016,** *116* (16), 9237-9304.

4. Lyndon, R.; You, W.; Ma, Y.; Bacsa, J.; Gong, Y.; Stangland, E. E.; Walton, K. S.; Sholl, D. S.; Lively, R. P., Tuning the structures of metal–organic frameworks via a mixed-linker strategy for ethylene/ethane kinetic separation. *Chemistry of Materials* **2020,** *32* (9), 3715-3722.

5. Darunte, L. A.; Terada, Y.; Murdock, C. R.; Walton, K. S.; Sholl, D. S.; Jones, C. W., Monolith-supported amine-functionalized Mg2 (dobpdc) adsorbents for CO_2 capture. *ACS applied materials & interfaces* **2017,** *9* (20), 17042-17050.

6. Joshi, J. N.; Garcia-Gutierrez, E. Y.; Moran, C. M.; Deneff, J. I.; Walton, K. S., Engineering copper carboxylate functionalities on water stable metal–organic frameworks for enhancement of ammonia removal capacities. *The Journal of Physical Chemistry C* **2017,** *121* (6), 3310-3319.

7. Darunte, L. A.; Oetomo, A. D.; Walton, K. S.; Sholl, D. S.; Jones, C. W., Direct air capture of CO_2 using amine functionalized MIL-101 (Cr). *ACS Sustainable Chemistry & Engineering* **2016,** *4* (10), 5761-5768.

8. Jasuja, H.; Walton, K. S., Experimental study of CO_2, CH_4, and water vapor adsorption on a dimethyl-functionalized UiO-66 framework. *The Journal of Physical Chemistry C* **2013,** *117* (14), 7062-7068.

9. Cmarik, G. E.; Kim, M.; Cohen, S. M.; Walton, K. S., Tuning the adsorption properties of UiO-66 via ligand functionalization. *Langmuir* **2012,** *28* (44), 15606-15613.

10. Couck, S.; Denayer, J. F.; Baron, G. V.; Rémy, T.; Gascon, J.; Kapteijn, F., An amine-functionalized MIL-53 metal− organic framework with large separation power for CO_2 and CH_4. *Journal of the American Chemical Society* **2009,** *131* (18), 6326-6327.

11. Wu, L.; Xue, M.; Qiu, S.-L.; Chaplais, G.; Simon-Masseron, A.; Patarin, J., Amino-modified MIL-68 (In) with enhanced hydrogen and carbon dioxide sorption enthalpy. *Microporous and mesoporous materials* **2012,** *157*, 75-81.

12. Yang, Q.; Wiersum, A. D.; Llewellyn, P. L.; Guillerm, V.; Serre, C.; Maurin, G., Functionalizing porous zirconium terephthalate UiO-66 (Zr) for natural gas upgrading: a computational exploration. *Chemical Communications* **2011,** *47* (34), 9603-9605.

13. Li, B.; Lu, F. F.; Gu, X. W.; Shao, K.; Wu, E.; Qian, G., Immobilization of Lewis Basic Nitrogen Sites into a Chemically Stable Metal–Organic Framework for Benchmark Water‐Sorption‐Driven Heat Allocations. *Advanced Science* **2022,** *9* (11), 2105556.

14. Winarta, J.; Shan, B.; Mcintyre, S. M.; Ye, L.; Wang, C.; Liu, J.; Mu, B., A decade of UiO-66 research: a historic review of dynamic structure, synthesis mechanisms, and characterization techniques of an archetypal metal–organic framework. *Crystal Growth & Design* **2019,** *20* (2), 1347-1362.

15. Pearson, R. G., Hard and soft acids and bases. *Journal of the American Chemical society* **1963,** *85* (22), 3533-3539.

16. Walton, I.; Chen, C.; Rimsza, J. M.; Nenoff, T. M.; Walton, K. S., Enhanced sulfur dioxide adsorption in UiO-66 through crystal engineering and chalcogen bonding. *Crystal Growth & Design* **2020,** *20* (9), 6139-6146.

17. Waitschat, S.; Fröhlich, D.; Reinsch, H.; Terraschke, H.; Lomachenko, K.; Lamberti, C.; Kummer, H.; Helling, T.; Baumgartner, M.; Henninger, S., Synthesis of M-UiO-66 (M= Zr, Ce or Hf) employing 2, 5-pyridinedicarboxylic acid as a linker: defect chemistry, framework hydrophilisation and sorption properties. *Dalton Transactions* **2018,** *47* (4), 1062-1070.

18. Barkhordarian, A. A.; Kepert, C. J., Two new porous UiO-66-type zirconium frameworks; open aromatic N-donor sites and their post-synthetic methylation and metallation. *Journal of Materials Chemistry A* **2017,** *5* (11), 5612-5618.

19. Jacobsen, J.; Reinsch, H.; Stock, N., Systematic Investigations of the Transition between Framework Topologies in Ce/Zr-MOFs. *Inorganic chemistry* **2018,** *57* (20), 12820-12826.

20. Walton, K. S.; Snurr, R. Q., Applicability of the BET method for determining surface areas of microporous metal− organic frameworks. *Journal of the American Chemical Society* **2007,** *129* (27), 8552-8556.

21. Lee, S.; Lee, J. H.; Kim, J., User-friendly graphical user interface software for ideal adsorbed solution theory calculations. *Korean Journal of Chemical Engineering* **2018,** *35* (1), 214-221.

22. Perdew, J. P.; Burke, K.; Ernzerhof, M., D. of physics and NOL 70118 J. quantum theory group tulane university. *Phys. Rev. Lett* **1996,** *77*, 3865-3868.

23. Grimme, S.; Antony, J.; Ehrlich, S.; Krieg, H., A consistent and accurate ab initio parametrization of density functional dispersion correction (DFT-D) for the 94 elements H-Pu. *The Journal of chemical physics* **2010,** *132* (15), 154104.

24. Kresse, G.; Furthmüller, J., Efficiency of ab-initio total energy calculations for metals and semiconductors using a plane-wave basis set. *Computational materials science* **1996,** *6* (1), 15-50.

25. Kozlov, A. N.-E. S. M.; Viñes, F.; Illas, F., Electronic-structure-based chemical descriptors:(in) dependence on self-interaction and Hartree-Fock exchange. *Phys. Rev. B* **1996,** *54*, 11169-11186.

26. Cui, K.; Bhattacharyya, S.; Nair, S.; Schmidt, J., Origins of acid-gas stability behavior in zeolitic imidazolate frameworks: The unique high stability of ZIF-71. *Journal of the American Chemical Society* **2021,** *143* (43), 18061-18072.

27. Sillar, K.; Hofmann, A.; Sauer, J., Ab initio study of hydrogen adsorption in MOF-5. *Journal of the American Chemical Society* **2009,** *131* (11), 4143-4150.

28. Sillar, K.; Sauer, J., Ab initio prediction of adsorption isotherms for small molecules in metal–organic frameworks: the effect of lateral interactions for methane/CPO-27-Mg. *Journal of the American Chemical Society* **2012,** *134* (44), 18354-18365.

29. Schütz, M.; Hetzer, G.; Werner, H.-J., Low-order scaling local electron correlation methods. I. Linear scaling local MP2. *The Journal of chemical physics* **1999,** *111* (13), 5691-5705.

30. Cui, K.; Schmidt, J., Enabling Efficient and Accurate Computational Studies of MOF Reactivity via QM/MM and QM/QM Methods. *The Journal of Physical Chemistry C* **2020,** *124* (19), 10550-10560.

31. Perdew, J.; Burke, K.; Ernzerhof, M., Quantum Monte Carlo calculations for a large number of bosons in a harmonic trap. *Phys. Rev. Lett* **1996,** *77*, 3865-3868.

32. Francl, M. M.; Pietro, W. J.; Hehre, W. J.; Binkley, J. S.; Gordon, M. S.; DeFrees, D. J.; Pople, J. A., Self‐consistent molecular orbital methods. XXIII. A polarization‐type basis set for second‐row elements. *The Journal of Chemical Physics* **1982,** *77* (7), 3654-3665.

33. Frisch, M.; Trucks, G.; Schlegel, H.; Scuseria, G.; Robb, M.; Cheeseman, J.; Scalmani, G.; Barone, V.; Petersson, G.; Nakatsuji, H., Gaussian 16 Revision C. 01. 2016; Gaussian Inc. *Wallingford CT* **2016,** *421*.

34. Wang, Y.; Smith, J. S.; Liu, Y.; Lu, P.; Zhang, X.; Ng, D.; Xie, Z., Surface Hydrophilicity Modification of Thin-Film Composite Membranes with Metal− Organic Frameworks (MOFs) Ti-UiO-66 for Simultaneous Enhancement of Anti-fouling Property and Desalination Performance. *Separation and Purification Technology* **2022**, 122001.

35. Fathieh, F.; Kalmutzki, M. J.; Kapustin, E. A.; Waller, P. J.; Yang, J.; Yaghi, O. M., Practical water production from desert air. *Science advances* **2018,** *4* (6), eaat3198.

36. Brandt, P.; Nuhnen, A.; Lange, M.; Möllmer, J.; Weingart, O.; Janiak, C., Metal–organic frameworks with potential application for SO_2 separation and flue gas desulfurization. *ACS applied materials & interfaces* **2019,** *11* (19), 17350-17358.

37. Fan, Y. L.; Zhang, H. P.; Yin, M. J.; Krishna, R.; Feng, X. F.; Wang, L.; Luo, M. B.; Luo, F., High Adsorption Capacity and Selectivity of SO_2 over CO_2 in a Metal–Organic Framework. *Inorganic Chemistry* **2020,** *60* (1), 4-8.

38. Berestova, T. V.; Kuzina, L. G.; Amineva, N. A.; Faizrakhmanov, I. S.; Massalimov, I. A.; Mustafin, A. G., ATR-FTIR spectroscopic investigation of the cis-and trans-bis-(α-amino acids) copper (II) complexes. *Journal of Molecular Structure* **2017,** *1137*, 260-266.

39. Zou, C.; Vagin, S.; Kronast, A.; Rieger, B., Template mediated and solvent-free route to a variety of UiO-66 metal–organic frameworks. *RSC advances* **2016,** *6* (105), 102968-102971.

40. Weiler, F. H.; dos Santos Grasel, F.; Lourega, R. V.; da Silva Ramos, A.; Ferrao, M. F., Simultaneous determination of sulfur, nitrogen and ash for vegetable tannins using ATR-FTIR spectroscopy and multivariate regression. *Microchemical Journal* **2019,** *149*, 103994.

41. Vegunta, V. L.; Stevanic, J. S.; Lindström, M.; Salmén, L., Thermal and alkali stability of sodium dithionite studied using ATR-FTIR spectroscopy. *BioResources* **2017,** *12* (2), 2496-2506.

42. Peterson, G. W.; Mahle, J. J.; DeCoste, J. B.; Gordon, W. O.; Rossin, J. A., Extraordinary NO2 Removal by the Metal‐Organic Framework UiO‐66‐NH2. *Angewandte Chemie* **2016,** *128* (21), 6343-6346.

43. Legon, A. C., Tetrel, pnictogen and chalcogen bonds identified in the gas phase before they had names: A systematic look at non-covalent interactions. *Physical Chemistry Chemical Physics* **2017,** *19* (23), 14884-14896.

44. Brammer, L., Halogen bonding, chalcogen bonding, pnictogen bonding, tetrel bonding: origins, current status and discussion. *Faraday Discussions* **2017,** *203*, 485-507.

45. Agwupuye, J. A.; Louis, H.; Unimuke, T. O.; David, P.; Ubana, E. I.; Moshood, Y. L., Electronic structure investigation of the stability, reactivity, NBO analysis, thermodynamics, and the nature of the interactions in methyl-substituted imidazolium-based ionic liquids. *Journal of Molecular Liquids* **2021,** *337*, 116458.

CHAPTER 6. CONCLUSIONS AND RECOMMENDATIONS

6.1 Conclusions

This comprehensive dissertation delved into the exploration of knowledge and strategies aimed at designing, tuning, and engineering the structure and properties of Metal-Organic Frameworks (MOFs) for highly efficient gas adsorption and separation processes, with a specific focus on flue gas desulfurization. The extensive research yielded a multitude of valuable insights and significant findings, which are summarized as follows: (1) Trivalent metals on MIL-100-M with less electronegativity show stronger affinity to SO_2 molecules for the metal elements are in the same row of the periodic table. Additionally, the functionality exhibited by trivalent metal sites on MIL-100-M was successfully replicated through a metal insertion process employed for UiO-66-2COOH, presenting a promising avenue for mimicking these favorable properties. (2) DETA-based ILs in MIL-101 via post modification not only resulted in a substantial increase in the capacity and selectivity of the MOFs for SO_2 capture but also significantly improved their overall stability. The investigation further emphasized the crucial role played by the anions of the ILs in influencing the adsorption properties of MOFs. (3) An affinity trend of a variety of nitrogen sites on MOF ligands to SO_2 molecules is revealed and the influence of chemical environment (like symmetry) of linkers on the overall adsorption behaviors of MOFs is demonstrated that expands our understanding of the design principles and tuning strategies employed to optimize the performance of MOFs in the context of flue gas desulfurization.

6.1.1 Chapter 3 conclusions

Chapter 3 has detailed the synthesis and characterization of MIL-100-M compounds, highlighted their diverse trivalent metal sites and investigated their adsorption properties in relation to SO_2. The primary focus was to understand how OMSs in these compounds interact with SO_2 molecules. The MIL-100-M MOFs featuring diverse OMSs were successfully prepared with consistent crystallinity and comparable porosity, ensuring a valid basis for property comparison. By analysing the SO_2 isotherms, a distinct pattern emerged, revealing a correlation between the affinity of trivalent metals towards SO_2 and the electronegativity trend. Specifically, metals with lower electronegativity displayed a stronger affinity for SO_2 for metal elements in a same row of the periodic table. Among the MIL-100-M series, MIL-100-Sc emerged as particularly noteworthy, exhibiting exceptional SO_2 uptake at low partial pressures, a higher IAST selectivity for SO_2 over CO_2, and remarkable stability against exposure to water vapor and humid SO_2. Additionally, the post-metal insertion approach was employed to modify UiO-66-2COOH with trivalent metals, resulting in the creation of UiO-66-2COOM compounds. These compounds demonstrated robust stability when subjected to humid SO_2 conditions. Notably, UiO-66-2COOSc and UiO-66-2COOIn displayed superior SO2 uptake compared to other UiO-66-2COOM samples, indicating that the post-introduced metals within UiO-66-2COOM can replicate the functionality of OMSs (Open Metal Sites) in MIL-100-M. These findings present a promising solution for addressing stability challenges in MOFs featuring OMSs while simultaneously preserving their exceptional adsorption properties. Future research endeavours can further explore and optimize the post-metal insertion strategy to enhance the stability and performance of MOFs with OMSs, ultimately contributing to the advancement of sustainable materials with tailored properties.

6.1.2 Chapter 4 conclusions

In this chapter, we explored a different approach to modifying MIL-101 by introducing DETA and DETA-based ILs after its synthesis. These modifications were made possible by establishing a covalent interaction between the open Cr sites on MIL-101 and the nitrogen sites on DETA or ILs, ensuring their stabilization. The resulting composites of modified MIL-101 exhibited significantly higher capacities for SO_2 compared to the original MIL-101, especially in the low partial pressure range. This notable improvement could be attributed to the presence of functional sites on DETA or DETA-based ILs, which possessed a strong affinity for SO_2 molecules. To evaluate the selectivity of the samples, the IAST selectivity was calculated at a SO_2/CO_2 ratio of 1/99 and a pressure of 1000 mbar. It was found that MIL-101-DETA demonstrated slightly higher selectivity than MIL-101 due to the beneficial properties of DETA for both SO_2 and CO_2 capture. Remarkably, all MIL-101-ILs composites exhibited significantly higher selectivity than both MIL-101 and MIL-101-DETA, suggesting that the presence of anions in the ILs promotes the adsorption of SO_2 over CO_2. Particularly noteworthy is the unprecedented IAST selectivity of MIL-101-DETA-Lac, which exhibited a thousand-fold higher selectivity for SO_2 over CO_2, highlighting the remarkable influence of the anion, lactate. Further analysis using DRIFTS revealed that the capture of SO_2 on MIL-101-ILs is reversible, while in the case of MIL-101, it is not. Additionally, the investigation of the stability of the composites before and after exposure to SO_2 or water demonstrated that the grafted ILs effectively protect the framework of MIL-101, showcasing their potential as stable and efficient adsorbents for SO_2 capture.

6.1.3 Chapter 5 conclusions

In Chapter 5, the order of affinity of nitrogen functional sites for the different MOF samples in terms of the kinetic adsorption of SO_2 could be summarized as follows: UiO-66-2,5-PDC > UiO-66-2,5-PziDC > UiO-66-NH_2 > UiO-66-3,5-PzoDC > UiO-66-NO_2 (pyridine > pyrazine > amino > pyrazole > nitro). The SO_2 capture on UiO-66-2,5-PDC exhibited a remarkable increase of 6.6 times compared to the parent UiO-66. Additionally, UiO-66-2,5-PDC demonstrated an unprecedented selectivity for SO_2 over CO_2 (209:1, calculated by IAST++ with 1% SO_2 and 99% CO_2) under ambient conditions. ATR-FTIR results provided evidence of the interactions between nitrogen sites on the MOFs and the adsorbed SO_2 molecules. Moreover, the preference of pyridine over amino for SO_2 capture was also observed in CAU-10 type MOFs. To investigate the SO_2 adsorption behaviours in the parent UiO-66 and three nitrogen-modified UiO-66 type MOFs, computational analysis was conducted. The binding energies of SO_2 at various sites were calculated using periodic DFT. The results revealed that the newly added nitrogen sites through modification exhibited the strongest binding affinity for SO_2. However, the modification had minimal impact on the binding strength at other sites. Therefore, the increased adsorption capacity for SO_2 was directly attributed to the presence of nitrogen sites. A detailed comparison of the binding of SO_2 to the nitrogen sites in UiO-66-2,5-PDC and UiO-66-2,5-PziDC showed that the symmetric distribution of the two nitrogen atoms in 2,5-PziDC resulted in less concentrated electron density on each nitrogen site, leading to weaker donor-acceptor interaction between the nitrogen site and SO_2. Furthermore, the symmetry of 2,5-PziDC resulted in a zero-dipole moment, eliminating any long-range electrostatic attraction to polar SO_2 adsorbates. Consequently, the binding strength of SO_2 to pyrazine was considerably weaker than that to pyridine, resulting in a lower adsorption capacity for SO_2 in UiO-66-2,5-PziDC despite having a larger number of

nitrogen sites. These findings underscore the significant influence of the chemical environment of MOFs on their adsorption capacities.

6.2 Recommendations

Investigation of other trivalent metals or functional sites: While this dissertation focused on MIL-100-M compounds with different trivalent metals, MIL-101-ILs with diverse anions, and nitrogen-modified UiO-66 featuring various nitrogen sites, there remains a vast array of unexplored possibilities. One avenue for further exploration involves studying the adsorption properties of MOFs containing other metals beyond those investigated previously. Lanthanide elements such as lanthanum[1] and cerium[2] could be promising candidates for investigation, as their unique electronic configurations and coordination geometries may influence their interactions with SO_2. By synthesizing and characterizing MOFs with these metals, researchers can gain valuable insights into the role of metal species in SO_2 adsorption mechanisms. Moreover, expanding the exploration to other functional sites within MOFs, such as oxygen and sulfur, holds considerable potential.[3-4] Oxygen sites, for instance, could provide Lewis basic sites capable of forming strong interactions with SO_2 molecules. Similarly, exploring MOFs with incorporated sulfur functionalities can also open up new possibilities. Investigating the impact of different oxygen or sulfur environments within MOFs on the adsorption capacity and selectivity towards SO_2 would offer crucial knowledge about the role of these functional sites in capturing pollutants. Overall, by testing a wide range of metals and exploring various functional sites, including oxygen and sulfur, within MOFs, researchers can gain valuable insights into the relationship between MOF properties and their interaction with SO_2. This expanded investigation will not only advance our fundamental understanding but also pave the way for designing more efficient and selective MOFs for SO_2 capture and mitigation in the future.

Characterization of functional sites - gas interactions: While this dissertation has employed various techniques to investigate the interactions between functional sites in MOFs and SO2 molecules, the scope of our understanding remains relatively limited. Advanced characterization techniques play a crucial role in unravelling the intricate interactions between functional sites and gases like SO_2. By employing techniques such as in situ spectroscopy, neutron scattering, and computational modelling, we can delve deeper into the adsorption process, unravelling the specific mechanisms and binding sites that govern the functional sites - gas interactions. In situ spectroscopy techniques[5-6], such as in-situ Raman spectroscopy, provide valuable information about the vibrational modes and chemical bonding within the MOFs during gas adsorption. By monitoring changes in the spectra of the MOFs as they come into contact with SO_2, we can identify the presence of specific functional groups or chemical species involved in the adsorption process. Time-resolved spectroscopic techniques can also provide insights into the kinetics of gas adsorption and desorption, shedding light on the dynamic behavior of functional sites - gas interactions. Neutron scattering techniques, including neutron diffraction and small-angle neutron scattering (SANS)[7], can provide detailed structural information about the adsorbed gas molecules within the MOF framework. Neutron diffraction allows to determine the precise positions and orientations of the gas molecules, providing insights into the adsorption sites and the nature of the host-guest interactions. SANS, on the other hand, enables the investigation of the structural changes occurring at the mesoscopic level, such as changes in porosity or pore connectivity induced by the adsorbed gas. Computational modeling, particularly density functional theory (DFT) calculations and molecular dynamics simulations, offers a powerful tool to complement experimental techniques. By simulating the interaction between MOFs and SO_2 at the

atomic scale, we can obtain a detailed understanding of the adsorption process, including the energetics, binding sites, and the dynamics of the adsorbed gas molecules.

Long-term stability, cycling performance, and scale-up and synthesis optimization: While this dissertation has provided valuable insights into the stability of MOFs through exposure to specific conditions for a duration of 24 hours, it is imperative to assess their long-term stability and cycling performance under realistic operating conditions. The practical viability of MOF materials heavily relies on their ability to maintain their adsorption performance over extended periods of time.[8-9] Therefore, subjecting the materials to prolonged exposure to humid SO_2 and evaluating their adsorption capacity and stability over multiple cycles is crucial to determine their suitability for practical applications. Furthermore, evaluating the feasibility of large-scale production is crucial to ensure the practicality and cost-effectiveness of MOF materials.[10-11] This involves assessing the scalability of the synthesis methods, evaluating the economic viability of the raw materials and manufacturing processes, and considering the environmental impact of large-scale MOF production. By addressing these aspects, we can guide the development of industrial-scale manufacturing processes that meet the demands of practical applications while considering economic and sustainability factors.

Exploration of other applications: In addition to the investigation of adsorption properties with SO_2, conducting comparative studies to explore the adsorption behaviour of MOF materials in this dissertation with other gases would be highly beneficial. By examining their interactions with gases like hydrogen sulfidic (H_2S), nitrogen dioxide (NO_2), or other harmful pollutants, a more comprehensive understanding of their potential for gas separation and capture applications can be achieved. Moreover, beyond gas adsorption applications, further research could expand the scope of MOFs' potential by exploring their utility in other areas such as gas

sensing[12], catalysis[13-14], or energy storage[15]. Investigating the performance and behaviour of these MOFs in these alternative applications can unlock additional opportunities for practical utilization.

6.3 References

1. Zhang, X.; Sun, F.; He, J.; Xu, H.; Cui, F.; Wang, W., Robust phosphate capture over inorganic adsorbents derived from lanthanum metal organic frameworks. *Chemical Engineering Journal* **2017,** *326*, 1086-1094.

2. Hu, Z.; Wang, Y.; Zhao, D., The chemistry and applications of hafnium and cerium (IV) metal–organic frameworks. *Chemical Society Reviews* **2021,** *50* (7), 4629-4683.

3. Damasceno Borges, D.; Normand, P.; Permiakova, A.; Babarao, R.; Heymans, N.; Galvao, D. S.; Serre, C.; De Weireld, G.; Maurin, G., Gas adsorption and separation by the Al-based metal–organic framework MIL-160. *The Journal of Physical Chemistry C* **2017,** *121* (48), 26822-26832.

4. Zárate, J. A.; Sánchez-González, E.; Jurado-Vázquez, T.; Gutiérrez-Alejandre, A.; González-Zamora, E.; Castillo, I.; Maurin, G.; Ibarra, I. A., Outstanding reversible H 2 S capture by an Al (iii)-based MOF. *Chemical Communications* **2019,** *55* (21), 3049-3052.

5. Liu, J.-J.; Jiang, Z.-W.; Hsu, S.-W., Investigation of the Performance of Heterogeneous MOF-Silver Nanocube Nanocomposites as CO_2 Reduction Photocatalysts by In Situ Raman Spectroscopy. *ACS Applied Materials & Interfaces* **2023,** *15* (5), 6716-6725.

6. Jin, Z.; Wang, X., In situ XPS proved efficient charge transfer and ion adsorption of $ZnCo_2O_4$/CoS S-Scheme heterojunctions for photocatalytic hydrogen evolution. *Materials Today Energy* **2022,** *30*, 101164.

7. Nayuk, R.; Zacher, D.; Schweins, R.; Wiktor, C.; Fischer, R.; Van Tendeloo, G.; Huber, K., Modulated Formation of MOF-5 Nanoparticles · A SANS Analysis. *The Journal of Physical Chemistry C* **2012,** *116* (10), 6127-6135.

8. Ding, M.; Cai, X.; Jiang, H.-L., Improving MOF stability: approaches and applications. *Chemical Science* **2019,** *10* (44), 10209-10230.

9. Carter, J. H.; Morris, C. G.; Godfrey, H. G.; Day, S. J.; Potter, J.; Thompson, S. P.; Tang, C. C.; Yang, S.; Schröder, M., Long-term stability of MFM-300 (Al) toward toxic air pollutants. *ACS applied materials & interfaces* **2020,** *12* (38), 42949-42954.

10. Wang, C.; Kim, J.; Tang, J.; Na, J.; Kang, Y. M.; Kim, M.; Lim, H.; Bando, Y.; Li, J.; Yamauchi, Y., Large‐scale synthesis of MOF‐derived superporous carbon aerogels with extraordinary adsorption capacity for organic solvents. *Angewandte Chemie* **2020,** *132* (5), 2082-2086.

11. Rubio-Martinez, M.; Avci-Camur, C.; Thornton, A. W.; Imaz, I.; Maspoch, D.; Hill, M. R., New synthetic routes towards MOF production at scale. *Chemical Society Reviews* **2017,** *46* (11), 3453-3480.

12. Lin, R. B.; Liu, S. Y.; Ye, J. W.; Li, X. Y.; Zhang, J. P., Photoluminescent metal–organic frameworks for gas sensing. *Advanced Science* **2016,** *3* (7), 1500434.

13. Huang, Y.-B.; Liang, J.; Wang, X.-S.; Cao, R., Multifunctional metal–organic framework catalysts: synergistic catalysis and tandem reactions. *Chemical Society Reviews* **2017,** *46* (1), 126-157.

14. Li, D.; Xu, H.-Q.; Jiao, L.; Jiang, H.-L., Metal-organic frameworks for catalysis: State of the art, challenges, and opportunities. *EnergyChem* **2019,** *1* (1), 100005.

15. Zhang, X.; Chen, A.; Zhong, M.; Zhang, Z.; Zhang, X.; Zhou, Z.; Bu, X.-H., Metal–organic frameworks (MOFs) and MOF-derived materials for energy storage and conversion. *Electrochemical Energy Reviews* **2019,** *2*, 29-104.

APPENDIX A. CHPATER 3 SUPPORTING INFORMATION

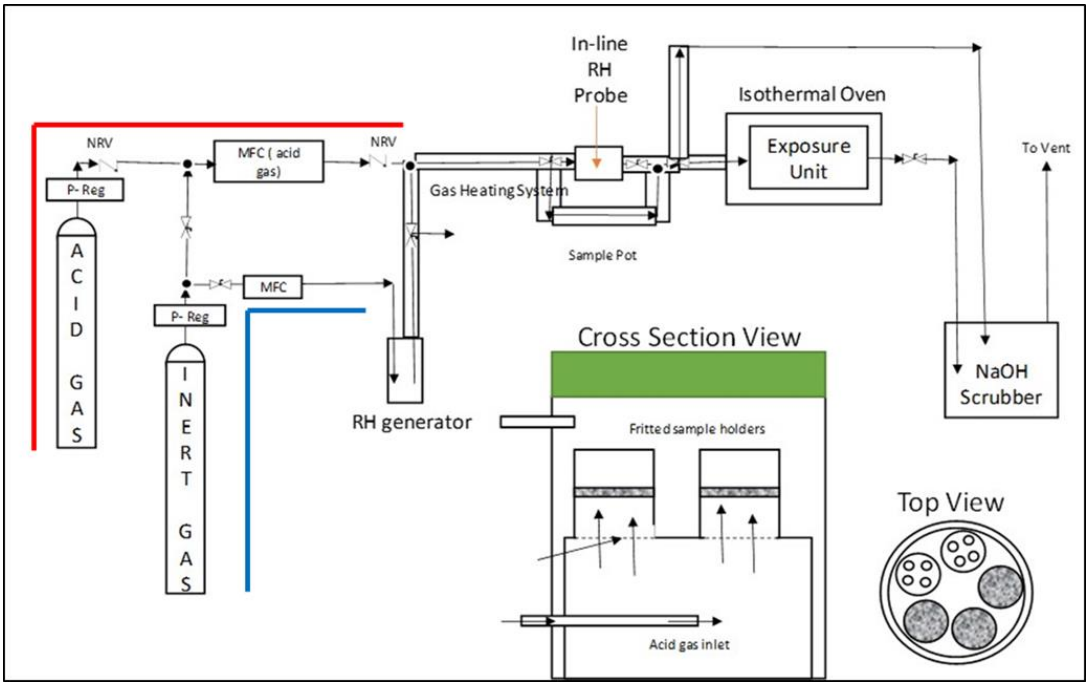

Figure A-1: Diagram of humid SO_2 exposure device.

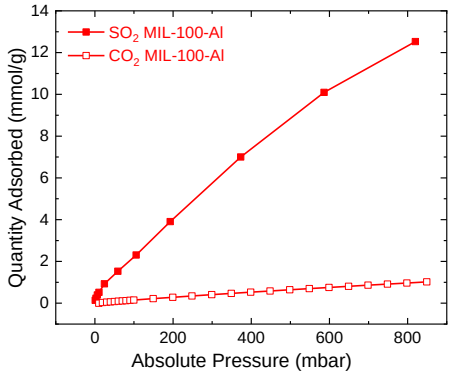

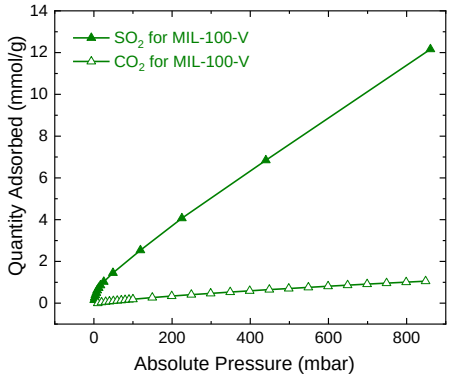

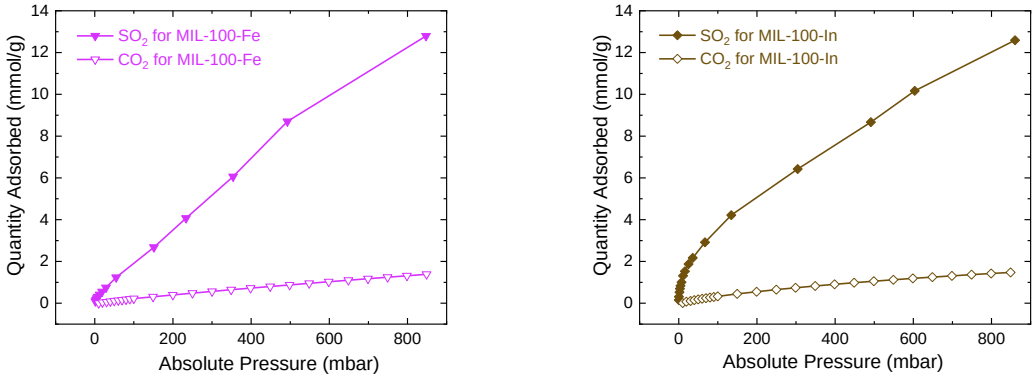

Figure A-2: Comparisons of SO_2 and CO_2 isotherms for MIL-100-M MOFs.

A.1 Preliminary results of DFT simulations for MIL-101-M (Dr. Thyagarajan Raghuram)

Density functional theory (DFT) simulations: MIL-100 was modeled using a trimetallic oxo-centered building unit with the M_3^{III} $(\mu_3\text{-O})(X)(COO)_6$ moiety reported in the literature.[1] M represents the trivalent metal ions ($M=Al^{3+}$, Sc^{3+}, V^{3+}, Fe^{3+}, In^{3+}) and X (F^-) is the counteranion to make the cluster charge neutral. The trimetallic clusters were placed in a large cubic box (a = 20 Å) and optimized using first-principle density functional theory (DFT) calculations implemented in VASP software.[2-3] The calculations used the projected augmented-wave pseudopotentials[4-5] with the generalized gradient approximation using the Perdew-Burke-Ernzerhof (PBE) functional.[6] We used a plane-wave cutoff energy of 520 eV with an energy tolerance of 10^{-4} eV for electronic minimization and 0.03 eV for ionic minimization self-consistent cycles. With a relatively large unit cell, we used a single gamma-point for our calculations.

The molecular binding energies of CO_2, SO_2 and H_2O with all variations of the trimetallic unit were estimated using DFT computations. We used the initial configurations for the metallic cluster and the adsorbate molecules from the work of Mavrandonakis and co-workers.[1] In their work, the configurations consisted of the trimetallic cluster and a pair of adsorbed guest molecules

of the same type. We relaxed the coordinates of the MIL-100 cluster and adsorbate molecules during the optimization. The binding energy for a single adsorbate molecule is defined as

$$\Delta E = 0.5(E_{MOF+ads} - E_{MOF} - E_{ads})$$

where $E_{MOF+ads}$, E_{MOF}, and E_{ads} denote the energies of the metallic cluster with a pair of adsorbed molecules, metallic cluster, and a pair of the adsorbate molecules in the gas phase, respectively. Based on this definition, a favorable binding implies a negative value for ΔE. The factor of 0.5 is to account for the two adsorbate molecules present in the cluster calculations.

Table A-1 shows the computed molecular binding energies for the three adsorbate molecules CO_2, SO_2 and H_2O with MIL-100 clusters for five different metal ions M (M = Al, Sc, V, Fe, and In.). It is observed that all metal ions have a stronger affinity for SO_2 than CO_2. This is also consistent with the adsorption isotherms measured in MIL-100 for SO_2 and CO_2, which are reported in Figures 3-3 and 3-4, respectively. The maximum observed adsorption loading for SO_2 is greater than 10 $mmolg^{-1}$ for all MIL-100 materials at 900 mbar. However, for CO_2 we observe a maximum uptake ~ 1.6 $mmolg^{-1}$ at 1 bar. Additionally, IAST predictions shown in Table 3-1 also suggest that the MIL-100 MOFs are all strongly SO_2 selective. Another observation from Table A-1 is that all MIL-100 clusters show the strongest affinity for the water molecule. This is very likely due to the hydrogen bonding interactions of the water molecule with the carboxylate ion groups in the trimetallic moiety.

Table A-1: Binding energies E (kJ/mol^{-1}) for three adsorbate molecules CO_2, SO_2, and H_2O with MIL-100 trimetallic cluster models with Al, Sc, V, Fe and In metal ions.

ΔE (kJ mol^{-1})	MIL-100-Al	MIL-100-Sc	MIL-100-V	MIL-100-Fe	MIL-100-In
CO_2	-21	-33	-19	-18	-35
SO_2	-32	-47	-51	-25	-54
H_2O	-72	-74	-57	-57	-89

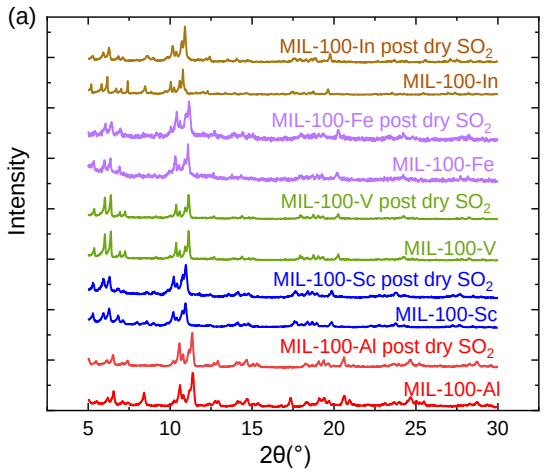

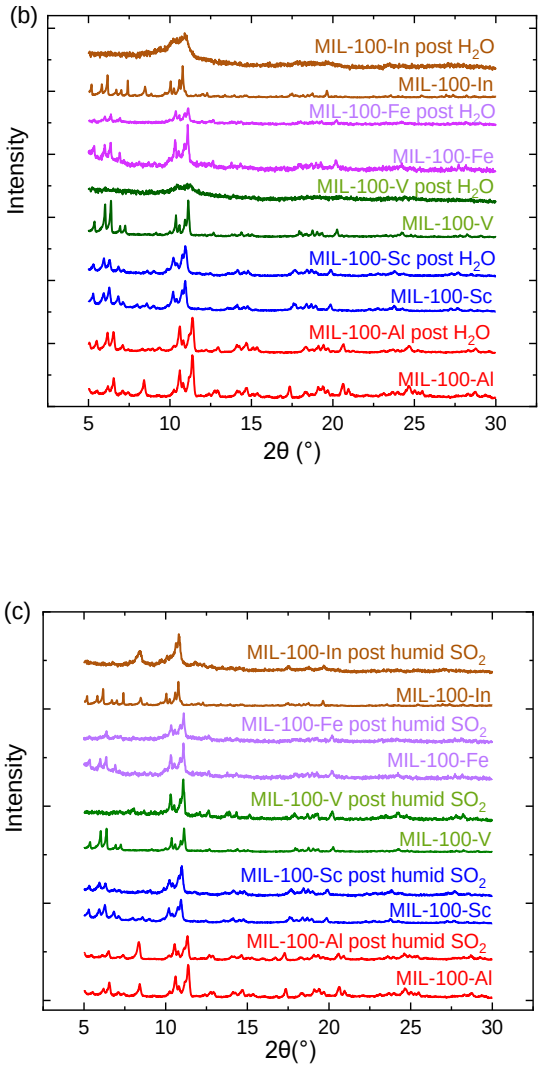

Figure A-3: PXRD of MIL-100-M after different treatments: (a), post dry SO_2, (b), post H_2O, and (c), post humid SO_2.

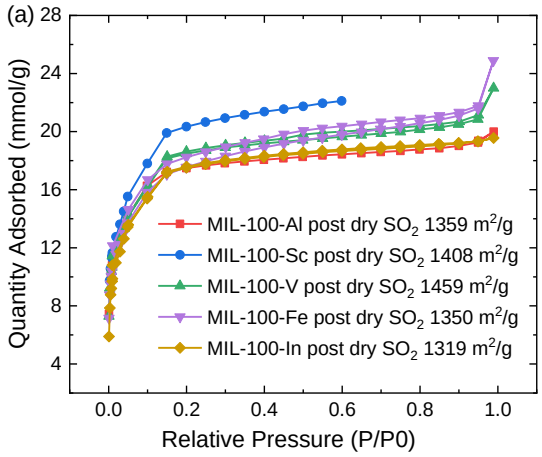
(a)
Quantity Adsorbed (mmol/g)
Relative Pressure (P/P0)
MIL-100-Al post dry SO2 1359 m2/g
MIL-100-Sc post dry SO2 1408 m2/g
MIL-100-V post dry SO2 1459 m2/g
MIL-100-Fe post dry SO2 1350 m2/g
MIL-100-In post dry SO2 1319 m2/g

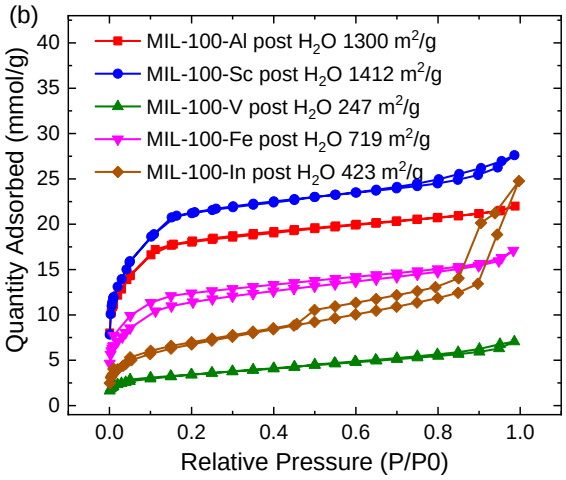
(b)
Quantity Adsorbed (mmol/g)
Relative Pressure (P/P0)
MIL-100-Al post H2O 1300 m2/g
MIL-100-Sc post H2O 1412 m2/g
MIL-100-V post H2O 247 m2/g
MIL-100-Fe post H2O 719 m2/g
MIL-100-In post H2O 423 m2/g

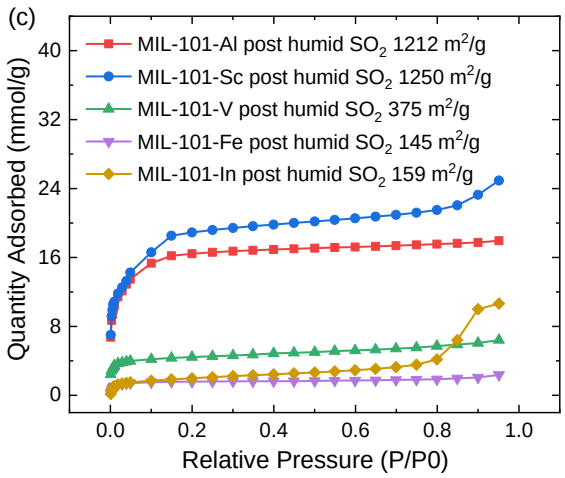

Figure A-4: N_2 adsorption isotherms of MIL-100-M after different treatments: (a), post dry SO_2, (b), post H_2O, and (c), post humid SO_2.

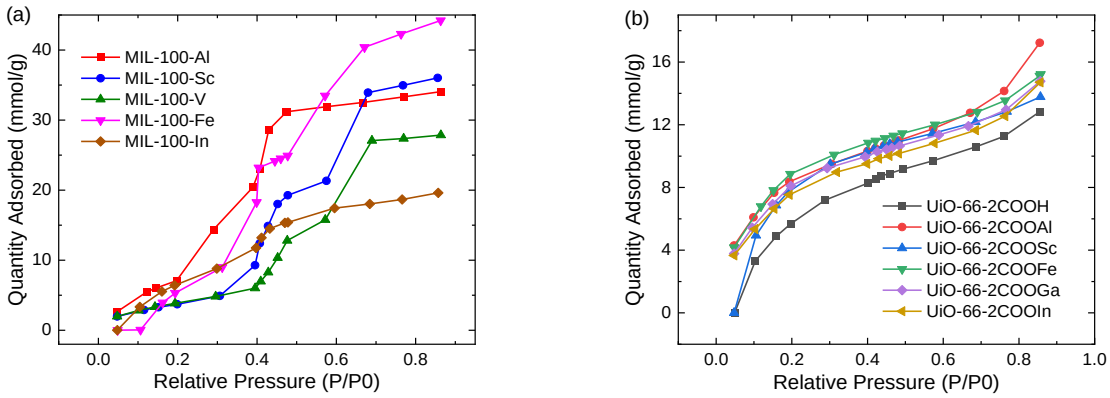

Figure A-5: Water vapor isotherms: (a), MIL-100-M; (b), UiO-66-2COOM.

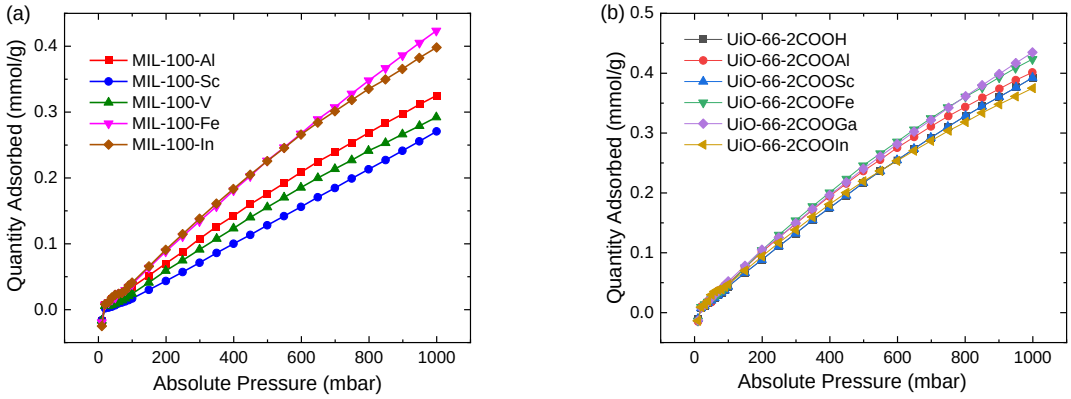

Figure A-6: CH_4 isotherms: (a), MIL-100-M; (b), UiO-66-2COOM.

A.2 References

1. Mavrandonakis, A.; Vogiatzis, K. D.; Boese, A. D.; Fink, K.; Heine, T.; Klopper, W., Ab Initio Study of the Adsorption of Small Molecules on Metal-Organic Frameworks with Oxo-centered Trimetallic Building Units: The Role of the Undercoordinated Metal Ion. *Inorg. Chem.* **2015,** *54* (17), 8251-63.

2. Kresse, G.; Furthmüller, J., Efficiency of ab-initio total energy calculations for metals and semiconductors using a plane-wave basis set. *Comput. Mater. Sci.* **1996,** *6* (1), 15-50.

3. Kresse, G.; Furthmüller, J., Efficient iterative schemes for ab initio total-energy calculations using a plane-wave basis set. *Phys. Rev. B* **1996,** *54* (16), 11169-11186.

4. Kresse, G.; Joubert, D., From ultrasoft pseudopotentials to the projector augmented-wave method. *Phys. Rev. B* **1999,** *59* (3), 1758-1775.

5. Blöchl, P. E., Projector augmented-wave method. *Phys. Rev. B* **1994,** *50* (24), 17953-17979.

6. Perdew, J. P.; Burke, K.; Ernzerhof, M., Generalized Gradient Approximation Made Simple. *Phys. Rev. Lett.* **1996,** *77* (18), 3865-3868.

APPENDIX B. CHPATER 4 SUPPORTING INFORMATION

Table B-1: Materials information.

Material	Formular	Molecular weight (g/mol)
DMF (Dimethylformamide)	$(CH_3)_2NC(O)H$	73.1
MIL-101	$C_{27}H_{23}NCr_3O_{16}$	773
DETA (diethylenetriamine)	$(NH_2CH_2CH_2)_2NH$	103.2
DETA-Cl	$(NH_2CH_2CH_2)_2NH\text{-}HCl$	139.6
DETA-Ace	$(NH_2CH_2CH_2)_2NH\text{-}HO_2H_2C_2$	162.2
DETA-Lac	$(NH_2CH_2CH_2)_2NH\text{-}HO_3H_5C_3$	193.3

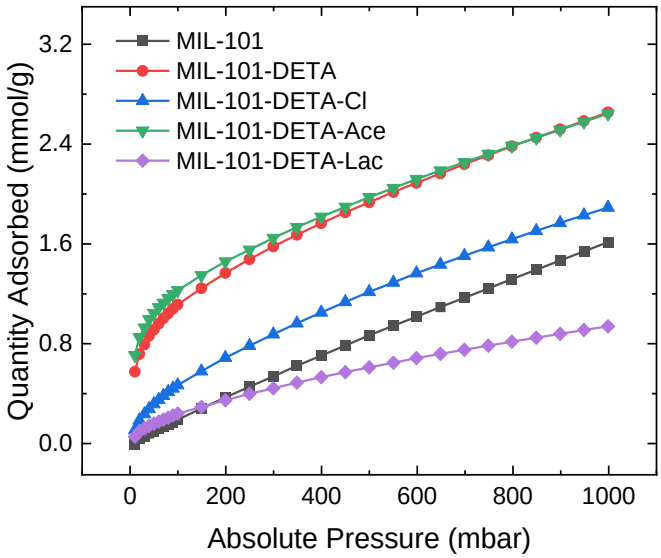

Figure B-1: CO_2 isotherms for MIL-101 and MIL-101 composites.

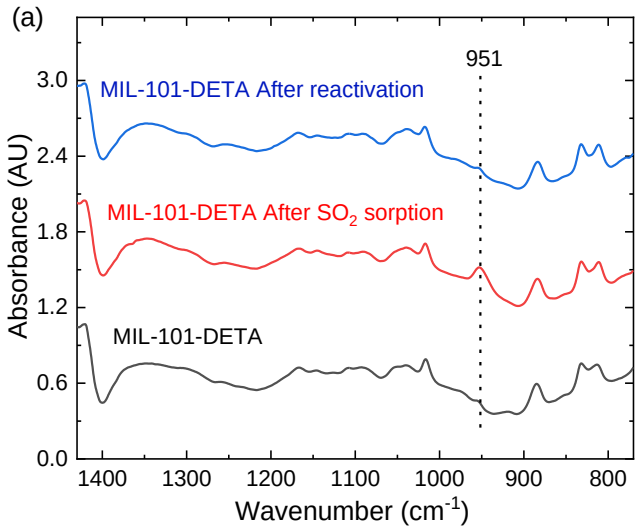

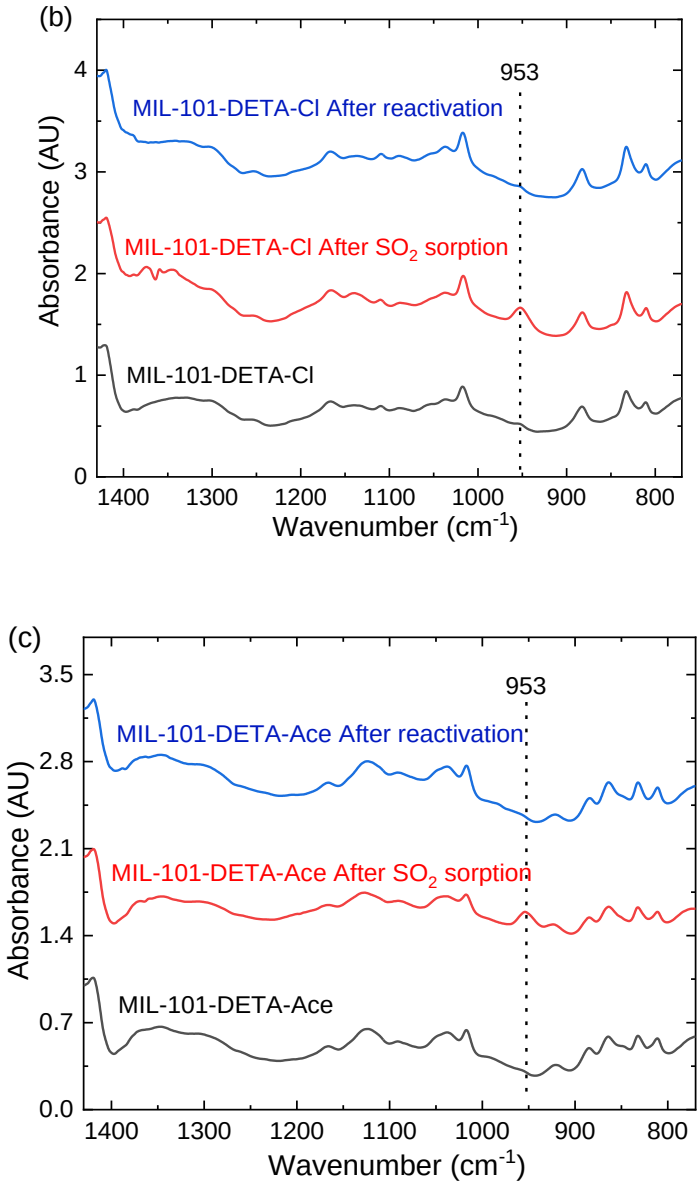

Figure B-2: In-situ DRIFTS spectra for (a) MIL-101-DETA, (b) MIL-101-DETA-Cl, and (c) MIL-101-DETA-Ace.

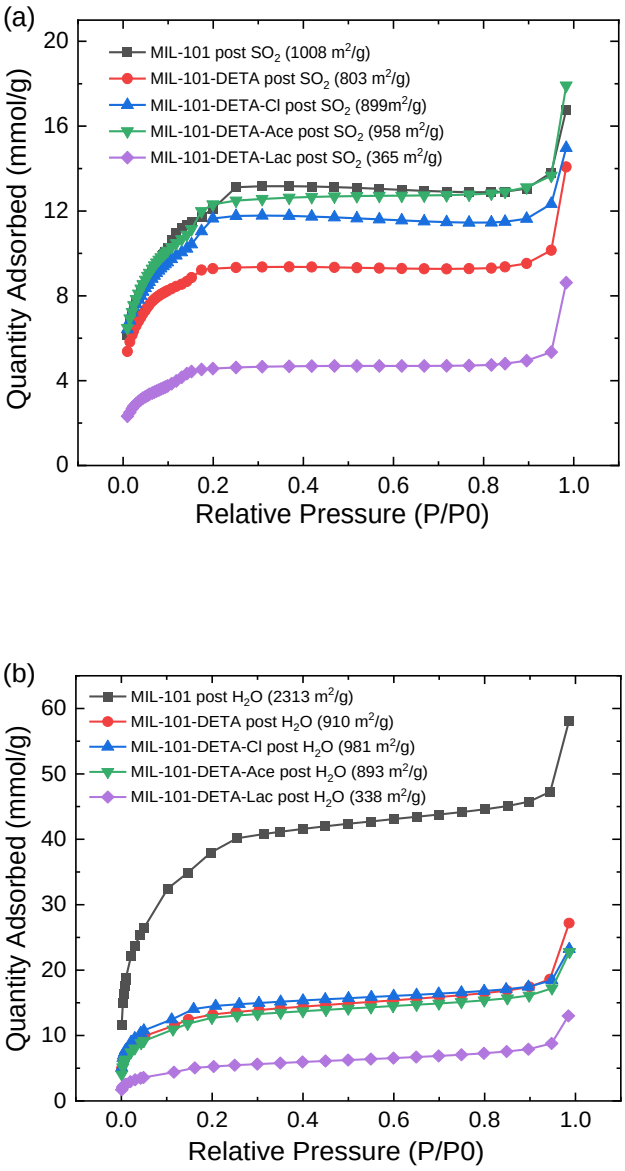

Figure B-3: BET surface areas for all samples (a) after SO_2 isotherm experiments and (b) after H_2O isotherm experiments.

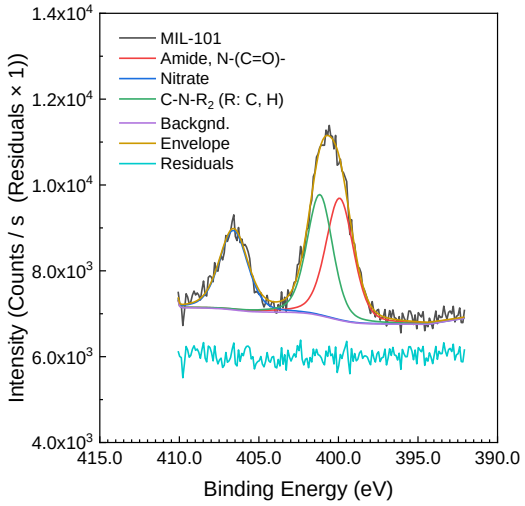
MIL-101
Amide, N-(C=O)-
Nitrate
C-N-R2 (R: C, H)
Backgnd.
Envelope
Residuals
Intensity (Counts / s (Residuals × 1))
Binding Energy (eV)

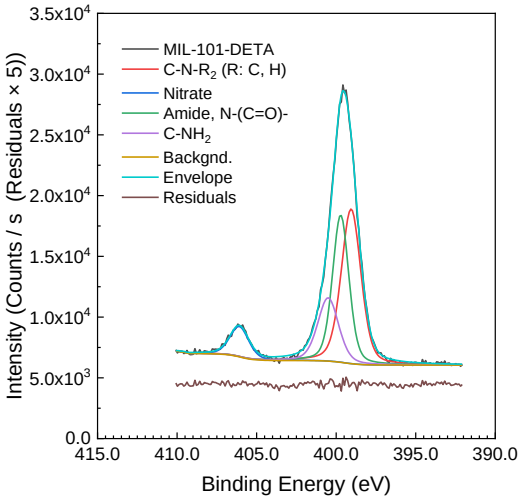
MIL-101-DETA
C-N-R2 (R: C, H)
Nitrate
Amide, N-(C=O)-
C-NH2
Backgnd.
Envelope
Residuals
Intensity (Counts / s (Residuals × 5))
Binding Energy (eV)

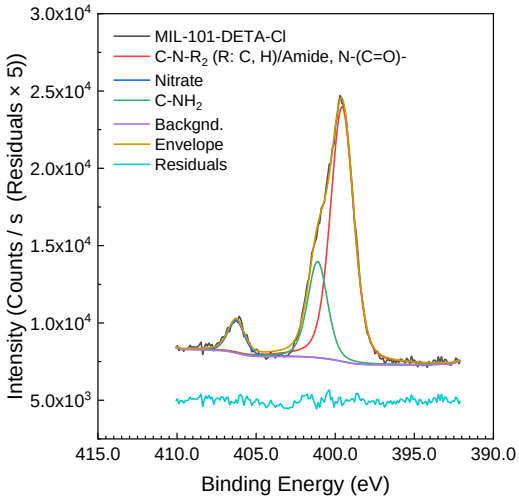
MIL-101-DETA-Cl
C-N-R2 (R: C, H)/Amide, N-(C=O)-
Nitrate
C-NH2
Backgnd.
Envelope
Residuals
Intensity (Counts / s (Residuals × 5))
Binding Energy (eV)

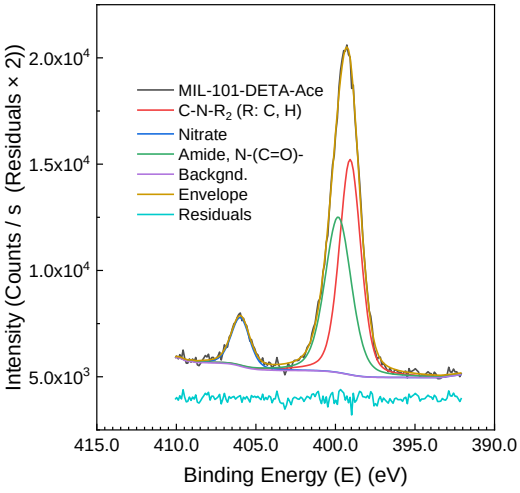
MIL-101-DETA-Ace
C-N-R2 (R: C, H)
Nitrate
Amide, N-(C=O)-
Backgnd.
Envelope
Residuals
Intensity (Counts / s (Residuals × 2))
Binding Energy (E) (eV)

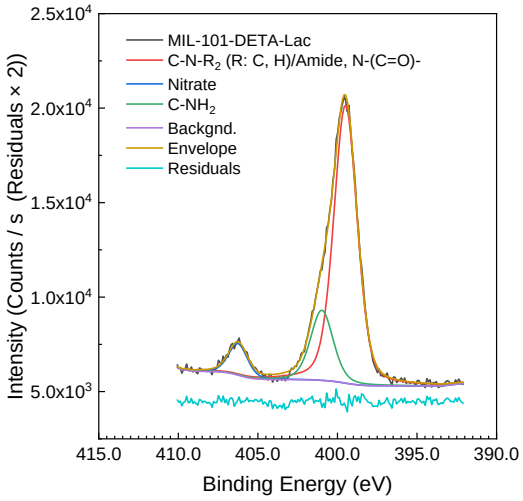

Figure B-4: N1s XPS spectra of MIL-101 and MIL-101 composites.

B.1 MIL-101-TETA-ILs

Tris(2-aminoethyl)amine (TETA) and TETA-based ionic liquids (ILs) were effectively synthesized and employed in the post-modification of MIL-101. Nevertheless, the comprehensive examination of these samples in terms of sulfur dioxide (SO_2) adsorption was not conducted, unlike the studies performed on DETA-based ILs. Here are a few measurements that have been carried out on these samples.

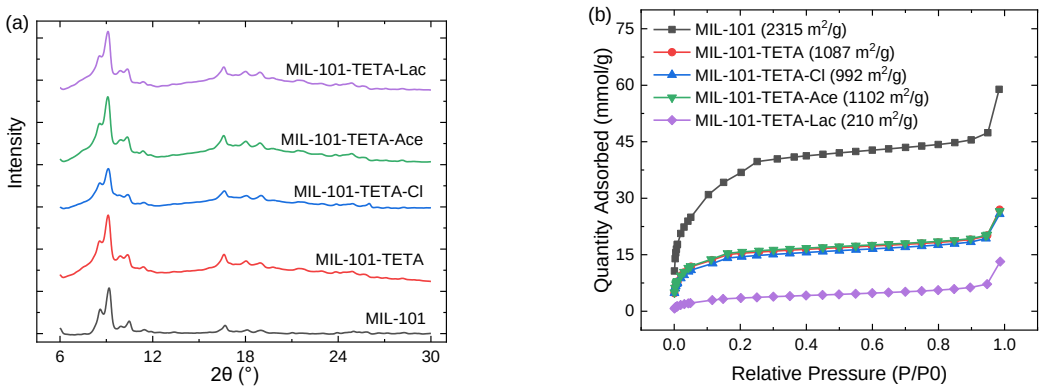

Figure B-5: (a) PXRD patterns and (b) BET surface areas of MIL-101-TETA-ILs.

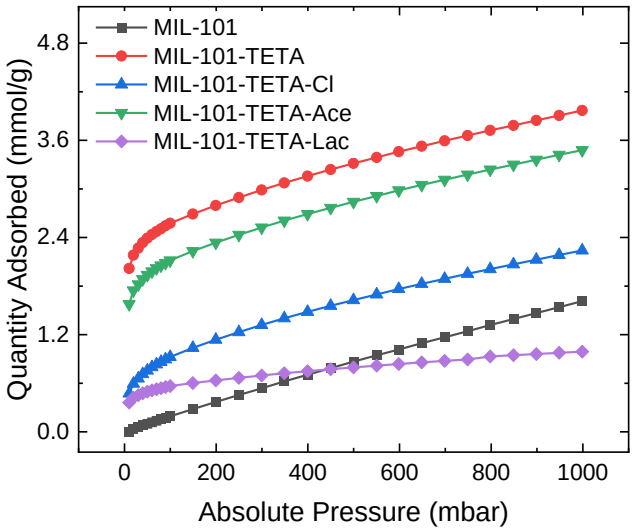

Figure B-6: CO_2 isotherms of MIL-101-TETA-ILs.

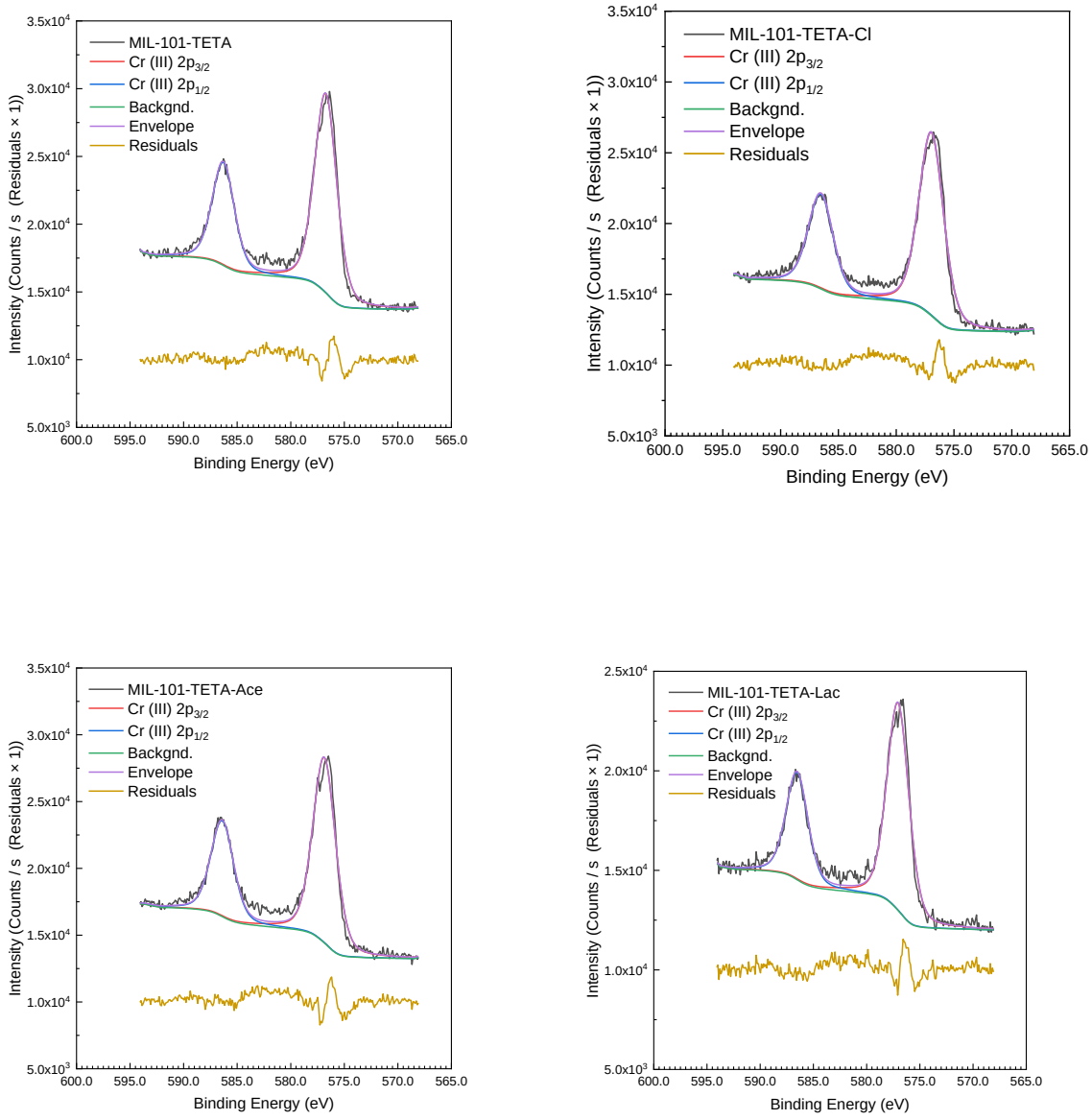

Figure B-7: Cr2p XPS spectra of MIL-101-TETA-ILs.

APPENDIX C. CHPATER 5 SUPPORTING INFORMATION

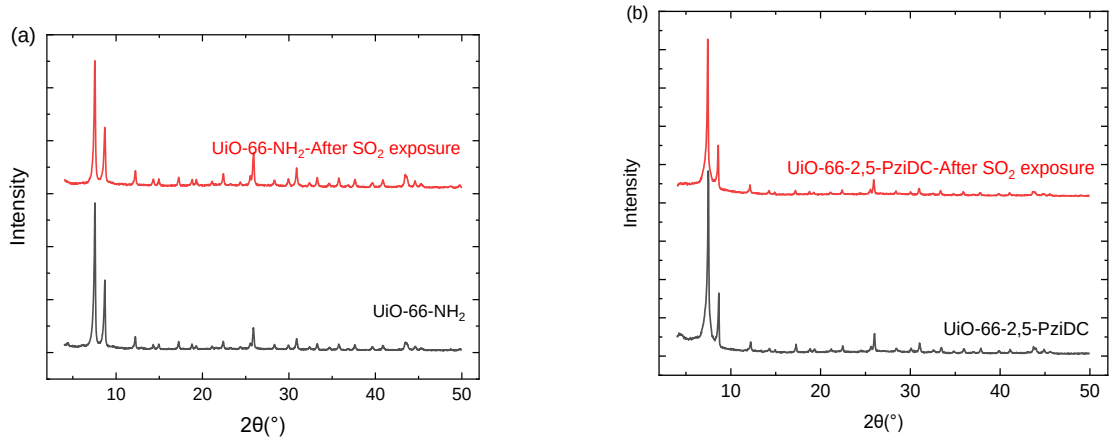

Figure C-1: PXRD patterns of (a) UiO-66-NH_2 and (b) UiO-66-2,5-PziDC MOFs before and after SO_2 exposure.

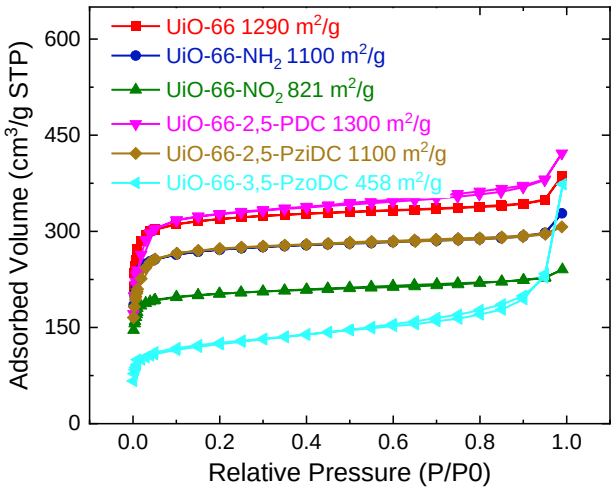

Figure C-2: BET surface areas of N-modified UiO-66 MOFs.

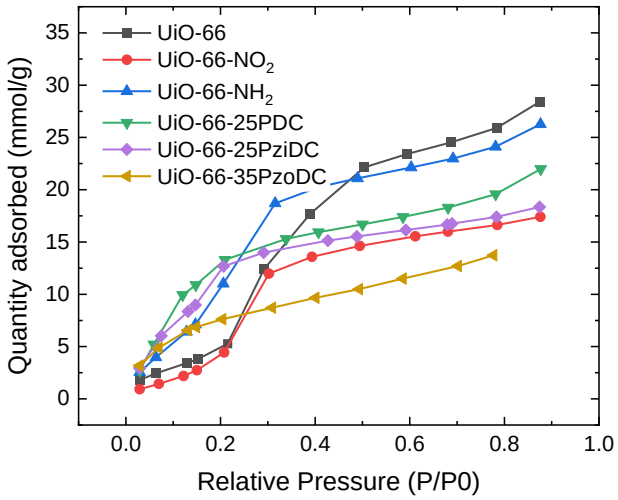

Figure C-3: Water vapor isotherms of N-modified UiO-66 MOFs.

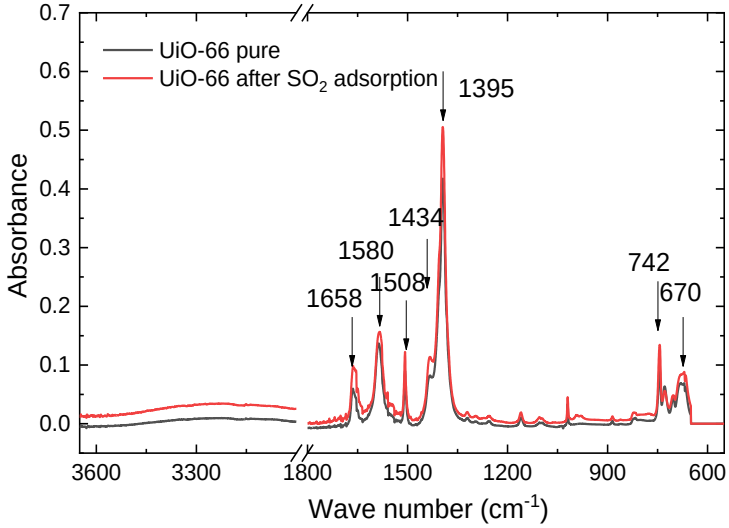

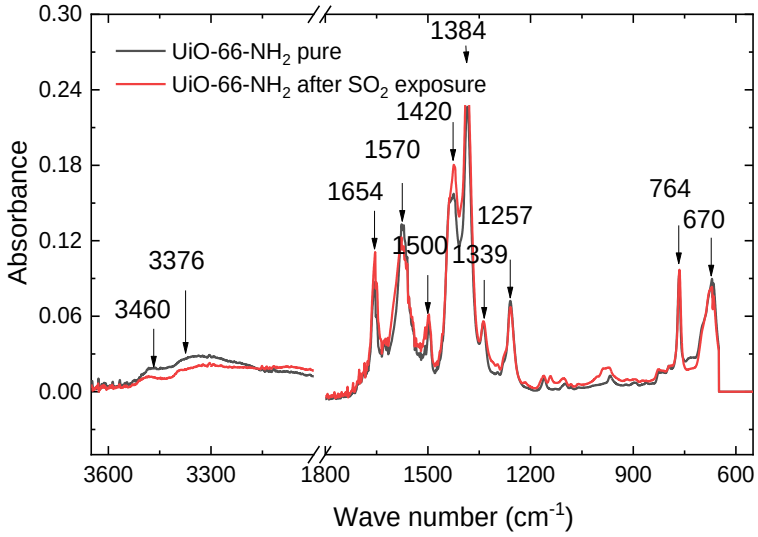
UiO-66-NH2 pure
UiO-66-NH2 after SO2 exposure
Absorbance
Wave number (cm-1)
0.30
0.24
0.18
0.12
0.06
0.00
3600
3300
1800
1500
1200
900
600
1384
1420
1570
1654
1257
1500
1339
764
670
3376
3460

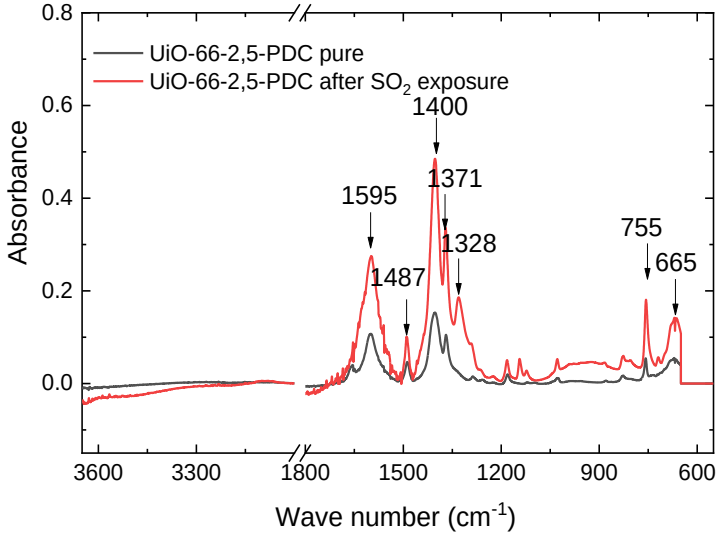
UiO-66-2,5-PDC pure
UiO-66-2,5-PDC after SO2 exposure
Absorbance
Wave number (cm-1)
0.8
0.6
0.4
0.2
0.0
3600
3300
1800
1500
1200
900
600
1400
1371
1595
1328
1487
755
665

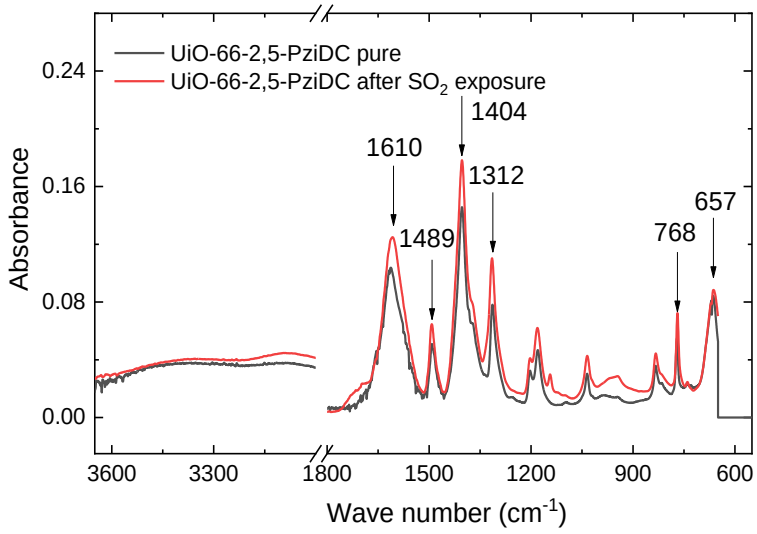

Figure C-4: ATR-IR spectra of N-modified UiO-66 MOFs before and after SO_2 exposure.

C.1 Geometry of the ML3 cluster model

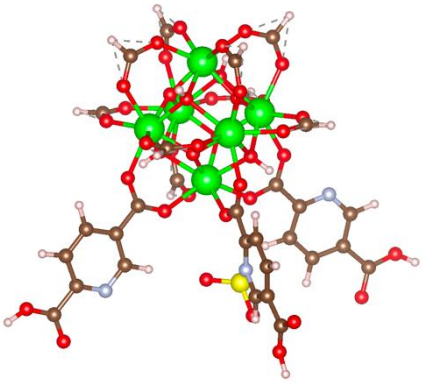

Figure C-5: Structure of the ML_3 cluster model.

Adsorption free energy calculation: Beyond the binding energies, a multisite Langmuir model[1-3] was used to calculate the isotherm and the Henry's constant. The binding free energy ΔG_s of SO_2 on each site s in the MOF were first calculated:

$$\Delta G_{\mathrm{s}} = \Delta E_s + \Delta E_{\mathrm{ZPE}} - T\Delta S_{\mathrm{trans-rot}} - RT$$

where ΔE_s is the binding energy, ΔE_{ZPE} is the zero-point energy change and $\Delta S_{\mathrm{trans-rot}}$ is the loss of translational and rotational entropy of SO_2 upon binding. The anharmonicity was included in the entropy calculation using the method described in[1]. The uptake at a given pressure p was calculated using the Langmuir isotherm equation:

$$n(p) = \sum_s c_s \frac{K_s p}{1 + K_s p}$$

where c_s is the concentration of site kind s in the MOF, $K_s = \exp(-\beta \Delta G_s)$ is the equilibrium constant of binding. The Henry's constant and the adsorption free energy can be calculated accordingly:

$$K_{\mathrm{H}} = \sum_s c_s K_s$$

$$\Delta G_{ad}^{\ominus} = -k_B T \ln \frac{K_H p^{\ominus}}{c^{\ominus}}$$

We first calculated the adsorption free energy in the parent and N-modified UiO-66 at PBE-D3 level, and then added a local MP2 (LMP2)[4] correction using the QM/QM approach[5] to achieve the high-accuracy results. The ML_3 cluster was used as the high-level region and will be treated at the LMP2 level, while the rest of the system was still treated at PBE-D3 level. The total energy of the system was:

$$\Delta E_{\mathrm{tot}}^{\mathrm{LMP2/PBE-D3}} = \Delta E_{\mathrm{clu}}^{\mathrm{LMP2}} - \Delta E_{\mathrm{clu}}^{\mathrm{PBE-D3}} + \Delta E_{\mathrm{tot}}^{\mathrm{PBE-D3}}$$

All cluster calculations were performed in Molpro 2019 package[6]. An effective core potential (ECP28MWB)[7] was used for Zirconium. Triple zeta ECP-based correlation consistent

basis sets of Peterson and co-workers (VTZ-PP)[8] was used for Zr and Dunning style correlation consistent basis sets[9] was used for other atoms (VTZ for H, C, AVTZ for N, S, O). When performing LMP2 calculations, the Boys localization scheme[10] was used.

Towards quantitative prediction of the adsorption free energy

We further seek more quantitative predictions of the adsorption free energy. For such calculations, more accurate correlated wave function methods are needed. We adapt the QM/QM method[5] to perform the high-level calculations. For most cases, PBE-D3 tends to overestimate the binding energy of SO_2 in MOFs. The largest deviation is observed at N sites, where $\Delta\Delta E = \Delta E_{\mathrm{LMP2}} - \Delta E_{\mathrm{PBE-D3}}$ can be as large as 2.3-3.2 kcal/mol. This large difference is probably from the well-known delocalization error of GGA functionals. With this large energy difference, to calculate the correct binding free energy at LMP2 level, the entropy change must also be corrected. We found a linear relationship between the ΔS and ΔE of binding in these MOF systems. Based on the calculated data at the PBE level, an empirical relation $T\Delta\Delta S \simeq 0.6066\,\Delta\Delta E$ is used to estimate the LMP2 correction to the entropy loss. With the LMP2 corrections, the calculated $\Delta G_{ad}^{\ominus}$ are listed in the last column in Table S1. For UiO-66, UiO-66-2,5-PziDC and UiO-66-NH_2, we can achieve quantitative prediction of the $\Delta G_{ad}^{\ominus}$ with errors about 0.2 kcal/mol. However, the prediction for UiO-66-2,5-PDC become worse. Possible reasons could be: (1) the empirical correction of entropy loss fails and (2) we missed some sites or configurations that are important at LMP2 level. Note that the calculation of the Henry's constant and $\Delta G_{ad}^{\ominus}$ is equivalent to calculate the absolute value of the partition function. Missing any sites or configurations leads to an underestimation of the total partition function, and thus a more positive prediction of the adsorption free energy.

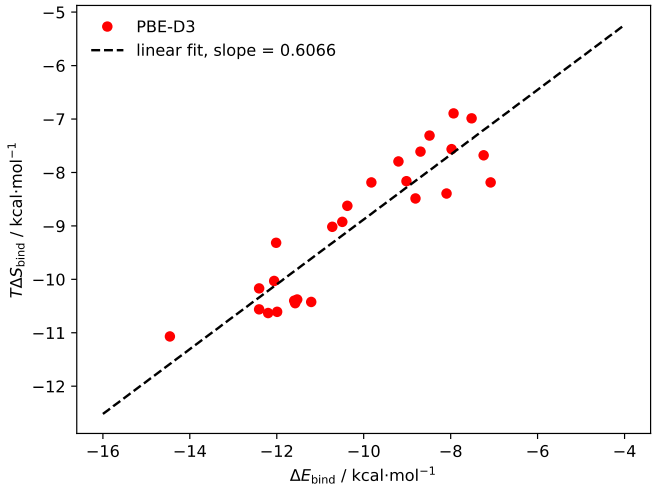

Figure C-6: Linear relationship between $T\Delta S_{bind}$ (T=298K) and ΔE_{bind} for SO_2 adsorption in UiO-66 type MOFs.

Table C-1: Calculated adsorption free energy $\Delta G_{ad}^{\ominus}$ (in kcal/mol) via Langmuir model at LMP2/PBE-D3 level for the parent and N-modified UiO-66 MOFs.

System	Experiment	LMP2/PBE-D3
UiO-66	-2.5	-2.8
UiO-66-NH_2	-3.5	-3.7
UiO-66-2,5-PDC	-4.2	-3.0
UiO-66-2,5-PziDC	-3.7	-3.5

C.2 Extension

CAU-10: CAU-10 was synthesized following an adapted literature procedure of Reinsch et al.[11] A homogeneous mixture of 5 mmol (1.875 g) of Aluminum nitrate nonahydrate, 5 mmol (0.830 g) of isophthalic acid (1,3-BDC), 10 mL of DMF, and 40 mL of H_2O, was placed in a 100 mL PTFE-lined autoclave. The reactor was heated in an isotherm oven at 135 ℃ for 12 h. The product was obtained by centrifuge at 8,000 rpm and washed three times each with DMF and then acetone.

CAU-10-NH_2 and **CAU-10-3,5-PDC:** CAU-10-NH_2 and CAU-10-3,5-PDC were synthesized analogously by replacing 1,3-BDC with 5-Aminoisophthalic acid (1,3-BDC-NH_2: 5 mmol, 0.906 g) and 3,5-Pyridinedicarboxylic acid (3,5-PDC: 5 mmol, 0.836 g).

Both experimental SO_2 adsorption results and computational calculations indicated that pyridine was more favorable for SO_2 capture than amino on UiO66 type MOFs. To check if this rule applicable for other MOFs, three CAU-10 MOFs (CAU-10, CAU-10-NH_2, and CAU-10-3,5-PDC) with same structures but different nitrogen functional sites were synthesized and their kinetic and dynamic SO_2 capture have been measured. As shown in Figure C-7, the results confirmed that pyridine possesses higher affinity to SO_2 than amino on CAU-10 type MOFs since CAU-10-3,5-PDC performed higher uptake of SO_2 than that of CAU-10-NH_2 for both measurements.

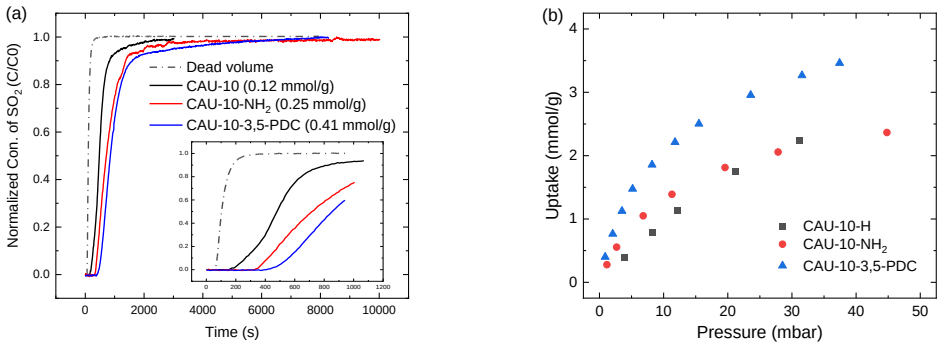

Figure C-7: (a), SO_2 Breakthrough measurements. (b), SO_2 isotherms for three CAU-10 type MOFs.

C.3 References

1. Cui, K.; Bhattacharyya, S.; Nair, S.; Schmidt, J., Origins of acid-gas stability behavior in zeolitic imidazolate frameworks: The unique high stability of ZIF-71. *Journal of the American Chemical Society* **2021,** *143* (43), 18061-18072.

2. Sillar, K.; Hofmann, A.; Sauer, J., Ab initio study of hydrogen adsorption in MOF-5. *Journal of the American Chemical Society* **2009,** *131* (11), 4143-4150.

3. Sillar, K.; Sauer, J., Ab initio prediction of adsorption isotherms for small molecules in metal–organic frameworks: the effect of lateral interactions for methane/CPO-27-Mg. *Journal of the American Chemical Society* **2012,** *134* (44), 18354-18365.

4. Schütz, M.; Hetzer, G.; Werner, H.-J., Low-order scaling local electron correlation methods. I. Linear scaling local MP2. *The Journal of chemical physics* **1999,** *111* (13), 5691-5705.

5. Cui, K.; Schmidt, J., Enabling Efficient and Accurate Computational Studies of MOF Reactivity via QM/MM and QM/QM Methods. *The Journal of Physical Chemistry C* **2020,** *124* (19), 10550-10560.

6. Werner, H.; Knowles, P.; Knizia, G.; Manby, F.; Schütz, M.; Celani, P.; Korona, T.; Lindh, R.; Mitrushenkov, A.; Rauhut, G., MOLPRO, version 2012.1, a package of ab initio programs, 2012. *Google Scholar There is no corresponding record for this reference* **2017**.

7. Nicklass, A.; Dolg, M.; Stoll, H.; Preuss, H., Ab initio energy‐adjusted pseudopotentials for the noble gases Ne through Xe: Calculation of atomic dipole and quadrupole polarizabilities. *The Journal of chemical physics* **1995,** *102* (22), 8942-8952.

8. Peterson, K. A.; Figgen, D.; Dolg, M.; Stoll, H., Energy-consistent relativistic pseudopotentials and correlation consistent basis sets for the 4 d elements Y–Pd. *The Journal of chemical physics* **2007,** *126* (12), 124101.

9. Peterson, K. A.; Yousaf, K. E., Molecular core-valence correlation effects involving the post-d elements Ga–Rn: Benchmarks and new pseudopotential-based correlation consistent basis sets. *The Journal of chemical physics* **2010,** *133* (17), 174116.

10. Foster, J.; Boys, S., Canonical configurational interaction procedure. *Reviews of Modern Physics* **1960,** *32* (2), 300.

11. Reinsch, H.; van der Veen, M. A.; Gil, B.; Marszalek, B.; Verbiest, T.; De Vos, D.; Stock, N., Structures, sorption characteristics, and nonlinear optical properties of a new series of highly stable aluminum MOFs. *Chemistry of Materials* **2013,** *25* (1), 17-26.